Theoretical and Experimental Tools for Clinical Translation of Quantitative Tissue Optical Sensing

by

Seung Yup Lee

A dissertation submitted in partial fulfillment
of the requirements for the degree of
Doctor of Philosophy
(Biomedical Engineering)
in The University of Michigan
2015

Doctoral Committee:

Professor Mary-Ann Mycek, Chair
Professor James M. Scheiman
Professor Zhen Xu
Professor Euisik Yoon

2015

Acknowledgements

This dissertation would have not been possible without the help and support of many people. First, I am very grateful to my advisor, Prof. Mary-Ann Mycek for all her guidance, support and patience. In particular, I thank for the opportunity and encouragement on an independent and initiative approach towards research. Now I feel I am one-step closer to an independent researcher. She has also set a role model of a great mentor for me.

I thank my three committee members: Dr. Jim Scheiman, who always provided support, guidance and fruitful discussion for clinical pancreas study; Dr. Euisik Yoon, who shared his expertise to initiate a new project using microfabrication technique; Dr. Zhen Xu, who provided valuable comments and insight on my research from my BME qualifying exam.

I also thank Dr. Stephen Feinberg for his advice and insight on my BME qualifying exam and Dr. Shiuhyang Kuo for the tissue constructs samples to help me exploring new applications in regenerative medicine.

Multi-disciplinary research works in this dissertation were possible with many great collaborators to thank: Dr. Diane Simeone, Dr. Barbara McKenna, Sheryl Korsnes, Dr. Jeremy Talyor and Dr. Oliver Lee for their helps on clinical optical data acquisition, analysis and discussion; Kyoungwhan Na, Komal Kampasi and Dr. Fan Wu from Prof. Yoon's lab in the EECS department for their training and advice on microfabrication and assembly process. I am thankful for all of my past and present lab mates: Dr. Malavika

Chandra, Dr. Robert Wilson, Dr. William Lloyd, Dr. Leng-Chun Chen, Dr. Sakib Elahi, Val Coldren and Urmi Parikh. I also thank my friend, Jungwon Ahn for his helps on heat simulation.

I also thank Dr. Rachael Schmedlen, whom I assisted in teaching BME Senior Design class, in which I learned a lot about teaching and design process.

Most importantly, I would like to thank my family: farther, mother and sister in Korea, who always prayed for me and showed me unconditional love and support.

My wife, Eunjin - You are my love and my best friend since we were 8 years old. Thank you for your endless support and trust in me.

My lovely 20-month-old daughter, Ruah - You contributed to this works more than you think by showing me your angelic smile every day.

Thank God for your faithfulness throughout my life.

Let light shine out of darkness… (2 Corinthian 4:6)

Chapter 2-3

This work was supported in part by the National Institutes of Health (NIH CA-114542 to M.-A.M.), the National Pancreas Foundation, the Wallace H. Coulter Foundation, the U.M. Comprehensive Cancer Center, and grants from the U.M. Medical School Translational Research Program and the American Society for Gastrointestinal Endoscopy.

Chapter 4

The project was supported in part by the National Institutes of Health (R01-DE-019431, to M.-A.M. and S.E.F.) U. M. Rackham Graduate School (Centennial Fellowship to S. Y. L)

Chapter 5

This work was supported in part by the National Institutes of Health (NIH R01-EB-018537), the U.M. Comprehensive Cancer Center and U. M. Rackham Graduate School

Table of Contents

List of Figures

List of Tables

Abstract

Quantitative tissue optical spectroscopy has been considered as a promising method for clinical diagnosis, owing to its ability to non-invasively give an objective assessment of biological tissues at cellular and sub-cellular levels. In spite of recent advances in optics and the computational power, not many quantitative tissue optical sensing technologies have been translated into clinical practice. In order to translate this technology in the clinics, we need to further improve the technology. To name a few, we need accurate and rapid quantification method for a real-time diagnostic feedback. Next, we need computational methods for complex tissue-optics problems. Also, we need a novel approach in probe design for the inaccessible organs. This dissertation focuses on the development, verification and validation of theoretical (mathematical and computational) and experimental (instrumental) tool set to promote the translation of quantitative tissue optical spectroscopy into clinical diagnostic applications.

For the mathematical tool, a direct-fit photon tissue interaction (DF-PTI) model that could rapidly and accurately extract the parameters associated biophysical features was developed and validated to characterize the precursor lesions of pancreatic cancer. A rapid scattering model on pancreatic tissue reflectance based on principal components analysis (PCA) results was also developed. The diagnostic capability of scattering properties obtained was demonstrated on an 18-patient data set using a rigorous statistical method, which implied the potential of reflectance spectroscopy for real-time detection of

pancreatic cancer. For the computational tool, a ray-traced Monte Carlo (RTMC) simulation for the design of fluorescence spectroscopy or imaging system utilizing complex optics to probe turbid biological tissues was devised. This new method was verified computationally with epithelial tissue models and experimentally using tissue-simulating optical phantoms. For the instrumental tool, the design and development of minimally-invasive diagnostic technologies employing optoelectronic components were discussed.

In this dissertation, we focused on detection of pancreatic cancer, which has the worst prognosis among other major cancers. Pancreatic tissues were employed as our model system to validate our developed tools. The developed technology and tools can be applied to a variety of other human tissue sites to help in the translation of quantitative tissue optical sensing in a clinical setting.

Chapter 1.
Introduction

1.1 Quantitative Tissue Optical Spectroscopy

Tissue optical spectroscopy has been considered a promising technique for non-invasive assessment of biological tissues in a variety of biomedical applications, including disease diagnostics [1] and cellular viability assessment [2]. Essentially, it is analyzing the spectral distribution of light that interacts with biological tissues and varies depending on tissue morphological (*e.g.* cellular density/structure), biochemical (*e.g.* metabolic rate) and physiological status (*e.g.* vascularization/intravascular oxygenation). The main sources in the spectral difference are attributed to light scattering or absorption, laser-induced fluorescence or Raman scattering pattern. Particular instrumental configurations for each technique or devices with multi-modal capability [3] have been successfully developed and employed to obtain those optical signatures from biological tissues. Not only the instrumentation, but also various quantitative methods [4] have been proposed to provide a quantitative and objective interpretation of the acquired spectral signal or a computational tool for optical probe design. Compared to the conventional imaging techniques currently employed in standard procedure, optical spectroscopy has the potential to become a more sensitive tool due to its capability of assessing alteration at a cellular and sub-cellular level [5].

However, even though spectroscopic technologies have been established during the last two decades based on recent advances in excitation sources (laser, lamp and LED), fiber

optic probes, sensitive detectors (Intensified Charged Couple Device (ICCD) and Electron Multiplying CCD(EMCCD)) and rapid electronics coupled with huge data processing capability, they have not been fully translated into clinical practice yet. In this dissertation, we focus on developing theoretical and experimental tools to address some technical challenges that are a barrier for clinical translation of quantitative optical tissue sensing. The developed tool set is intended to provide a comprehensive solution for mathematical, computational and instrumental needs in optical tissue sensing techniques on *in vivo* human tissue measurements. Although applications of each developed tool can be expanded to a variety of biomedical areas, the developed tools have been verified using tissue-simulating optical phantoms and computational epithelial tissue models or validated on pancreatic cancer detection from *ex vivo* human tissue measurements.

1.2 Basic Principles of Quantitative Tissue Optical Spectroscopy

1.2.1 Reflectance Spectroscopy

Reflectance spectroscopy measures the wavelength-dependent intensity of diffusively reflected light that undergoes scattering and absorption within biological tissues. An incident light on biological tissues is scattered whenever it encounters a mismatch of refractive index induced by inhomogeneous cellular structure or extracellular matrix. The scattering process is elastic, preserving the energy of the incident light with the same frequency; therefore it can occur in a broad wavelength range of incident light. These scattering events are also wavelength-dependent; *i.e.* different cellular or extracellular features contribute to the alteration of scattering intensity and angle at a particular wavelength range. Thus, the spectral distribution of elastically scattered light indicates characteristic features of biological tissues.

Absorption events occur when the light is absorbed by endogenous chromophores such as oxy- and deoxygenated hemoglobin [6], β-carotine [7] and bilirubin [8] or pigment (e.g. melanin) [9]. Each absorber has a unique spectral absorption feature; thus analyzing the absorption spectrum enables monitoring of physiological activity and diagnosing of some relevant diseases such as jaundice and skin cancer.

The instrumental setup of reflectance spectroscopy is relatively simple because a broad wavelength range can be measured and the intensity of reflectance is much higher than other spectroscopic techniques. A halogen lamp is the most commonly used broadband light source. An intensified charged-couple device (ICCD) coupled with spectrograph [10] or a compact spectrometer device [11] can be used for spectrum recording. As a result of recent advances in optoelectronics, white LED has emerged as an alternative, small but powerful broadband source [11] and a silicon-photodiode coupled with the selected excitation wavelength by monochromator from a broad band lamp source [12] has shown the capability of acquiring a wavelength-resolved diffuse reflectance.

1.2.2 Fluorescence Spectroscopy

Fluorescence spectroscopy measures fluorescence emitted by specific molecules that absorb excitation light. The molecule that absorbs excitation light is activated from the ground state to an excited state with a higher electronic energy level. Among a number of ways in which the molecules relax to the ground state, fluorescence is the re-emission of low energy photons with a longer wavelength than the excitation light. This wavelength shift is called the Stokes Shift.

Fluorescence spectroscopy has been employed to provide biochemical information in targeted biological tissues due to its molecular specificity. Molecular specific

fluorescence characteristics are the major difference between these and non-fluorescensing materials. The intrinsic fluorescence is dependent on the concentrations of the fluorophores and unique emission spectral characteristics of each fluorophore. The measured fluorescence spectrum contains not only this intrinsic fluorescence, but also scattering and absorption properties of tissue samples, which can affect fluorescence photon propagations. Thus, in order to obtain accurate biochemical information, quantitative methods are necessary to uncouple the desired intrinsic fluorescence from the measured fluorescence that is a result of mixed events.

Both endogenous and exogenous fluorophores can be employed in fluorescence spectroscopy. Endogenous fluorophores that are naturally fluorescent, include biological structures (such as mitochondria and lysosomes), molecules related to a metabolic process (such as NAD(P)H and Flavin), extracellular matrix, and proteins (containing amino acid, tryptophan and tyrosine) [13]. Targeting these endogenous fluorophores enables label-free optical sensing. Exogenous fluorophores are engineered to emit a strong fluorescence light with a high quantum yield. They are commonly used in cell imaging to observe spatial localization of specific event. Clinical application of these exogenous fluorophores requires a regulatory approval after ensuring clinical safety.

In a common instrumental setup of fluorescence spectroscopy, a laser source emitting the corresponding wavelength to the absorption spectrum of targeted fluorophores is employed for excitation. For detection, an optical long- or band- pass filter or a monochromater is needed to cut off the excitation laser. Sensitive detectors including, ICCDs, EMCCDs, photomultiplier tubes (PMTs) and avalanche photodiodes (APDs) are commonly used to capture a relatively weak fluorescence signal with high signal-to-noise

ratio. Optical components are carefully selected such that excitation light does not cause the autofluorescence in the optical components that could produce a noise in the target fluorescence.

1.2.3 Quantitative Analysis

Quantitative analysis of tissue optical spectroscopy aims to uncouple the desired optical signal to provide quantitative values of biologically-relevant parameters from the undesired background in the measured reflectance and fluorescence. A variety of quantitative techniques have been developed to model human tissue reflectance and fluorescence, including diffusion approximation (DA) [14], semi-empirical models [15] and Monte Carlo simulations [16]. With a goal to develop theoretical tools for clinical translation of tissue optical spectroscopy, this dissertation focuses on advances in the semi-empirical model and Monte Carlo simulation.

Diffusion approximation is an analytical solution to a simplified form of the radiative transfer equation (RTE) in a particular situation, in which diffusion can approximate overall photon propagations [17]. Although DAs have been commonly used in many applications [14, 18, 19], they are inaccurate for tissue interrogation with small source-detection separation, in which the photon path does not follow a diffusion regime [20]. As an alternative approach, forward semi-empirical models have been developed to analyze optical spectra obtained by small source-detector separation [15]. Inverse semi-empirical models have been employed to extract scattering and absorption coefficients in media or biophysical parameters [21, 22].

Monte Carlo simulations are viewed as the “gold standard” method for accurately simulating light transport in turbid media such as biological tissues [16, 23]. In MC

modeling, light transport is simulated by tracing each photon's random walk step. Every step size, angle and attenuation of individual photons between photon-tissue interactions are determined by random sampling based on tissue optical properties. Due to recent advances in computing power and speed, MC simulations have been extensively employed in various biomedical optics applications to solve both forward and inverse problems. In forward problems, optical spectra are estimated [24, 25] and depth-resolved optical probes are designed [26, 27]. Inverse models have been used to extract optical properties for distinguishing malignant tissue from benign [28, 29] .

1.3 Clinical Translation of Quantitative Tissue Optical Sensing Technologies

Not many tissue optical sensing technologies have been successfully commercialized for clinical diagnostic applications. The representative example of the device that became a standard-of-care in the clinic is the pulse oximeter. The pulse oximeter which is a common biophysical monitoring device in the hospital utilizes red and infrared light source to non-invasively measure oxygen saturation. Another example is the bilirubinometer, which measures total serum bilirubin level from bilirubin absorption and autofluorescence for neonatal jaundice diagnosis [30].

Most other technologies have been developed to detect or screen for different types of cancers. MelaFind® (Mela Sciences Inc.) [31] is a FDA- and CE- approved multispectral imaging device to aid in detection of early pigmented cutaneous melanoma by providing an objective analysis of an irregular mole pattern. VELscope® (LED Dental Inc.) is also a FDA-approved autofluorescence visualization system for oral cancer screening [32]. The WavSTAT Optical Biopsy system, developed by Spectra Science Inc., aims to become an adjunctive tool to diagnose colon and esophageal cancer during the current

endoscopic procedures. The system is based on fluorescence and scattering spectroscopy and now has FDA Premarket Approval (PMA). LuViva®, developed by Guided Therapeutics, is a multimodal spectroscopic imaging device for cervical cancer screening [33] and is currently under FDA PMA review, but is commercially available in other countries.

Some other optical techniques for oral cancer detection are currently undergoing clinical trials. The Multispectral Digital Microscopy [34] is a multispectral wide-field fluorescence and narrow-band imaging device. The FastEEM4 [35] obtains fluorescence spectra excited at different wavelengths, producing fluorescence excitation-emission matrices (EEM).

1.4 Current Technical Challenges

Accurate and Rapid Quantification Quantitative analysis of the obtained optical signals from the designed instrumentation is becoming more essential for clinical diagnostic applications. The quantification process can provide an objective assessment compared to traditional histology; which can potentially increase diagnostic efficiency and save necessary resources required for personnel training. In addition to providing diagnostically-relevant information accurately, some applications require a real-time or immediate feedback. This ability can maximize the utility of computational quantification compared to the traditional histology analysis performed off-site with delayed results

Computational Tool for More Complex Tissue-Optics Problem Tissue-optics problems in quantitative tissue optical sensing can be defined by how the technology obtains a targeted diagnostically-relevant parameter in the given tissue optical properties/structure and designed optical configuration. Computational modeling based on Monte Carlo

simulation plays a critical role in overcoming physical limitations on the actual realization of the hardware system and tissue preparation necessary during the tissue-optics problem solving process. Commercialized devices are handling a relatively simple tissue-optics problem that extracts oxy- and deoxy- hemoglobin or bilirubin concentrations based on bulk tissue-sensing. In tissue sensing applications for oral, cervical, colon and esophageal cancer detection, the model typically builds up two-layered tissue models consisting of epithelial tissue on top of stroma. However, for some clinical applications, tissue-optics problems may be more complex. Thus, there is a technical need in the computational tool to address advanced tissue-optics problems.

Instrumental Innovation for Increasing Accessibility to Confined Areas Most of the currently commercially-available techniques introduced in the chapter 1.3 target readily-accessible sites such as finger, forehead or skin, thus imposing no critical limitation in probe design, or sites that can be approached with patients' cooperation and appropriate probe design, such as oral and cervical sites. In case of the WavSTAT Optical Biopsy System, the optical probe needs to be delivered via one of the endoscopy working channels. Thus, design flexibility is strictly limited to approaches using a fiber-optic probe only. Even for some sites allowing only a hollow needle access, such as lung and pancreas, single fiber-based spectroscopy and imaging systems [36] compatible with the use of a needle have been demonstrated. However, optical fiber technologies have some technical drawbacks, including point measurements (lack of spatial information) and limited source-detector configurations.

1.5 Model System: Pancreatic Cancer

1.5.1 Background

The clinical problem for pancreatic cancer is that current diagnostic methods are inaccurate and unable to diagnose disease in patients with potentially curable pancreatic cancer. Pancreatic adenocarcinoma is the 4th leading cause of cancer deaths in the United States. By 2020, pancreatic cancer is projected to become the 2nd leading cause of cancer death [37], and over the next 20 years annual deaths from pancreatic cancer are expected to increase (the only one of the top five causes of cancer death to do so) until they double [38].

Among the estimated 42,000 patients diagnosed in this country last year, only 7% were diagnosed at an early stage [39]. This gives pancreatic cancer the dubious distinction of having the highest mortality rate for any solid tumor, with a 5-year survival rate of only 7%. Among those patients with advanced disease, there are two populations with considerable differences in survival. For those with metastatic disease, the 5-year survival is 1.8%, compared to 8% for those with localized regional disease (a tumor that is not amenable to surgical removal, typically due to involvement of critical blood vessels). Since the 5-year survival of patients with surgically resectable (or potentially resectable, after neo-adjuvant therapy) disease is 20%, accurate identification of such patients is essential to making progress in this disease.

Current diagnostic methods, including computed tomography (CT), magnetic resonance imaging, and endoscopic ultrasound (EUS) have not been able to provide accurate diagnosis in early-stage disease, either because of failure identify small lesions or inability to accurately differentiate masses as either adenocarcinoma or pancreatitis

(inflammation of the pancreas). Intensive efforts to identify and utilize molecular markers have not been able to address this diagnostic challenge.

1.5.2 Key Challenges

The critical challenge is to provide an accurate tissue diagnosis, which allows rapid institution of therapy: either surgery for resectable tumors, neoadjuvant therapy for borderline resectable disease, or definitive chemoradiotherapy for patients with localized unresectable disease. A recent consensus statement [40] concluded that pretreatment tissue diagnosis is mandatory for patients considered for therapy and that the current preferred modality for obtaining a tissue diagnosis is endoscopic ultrasound-guided fine-needle aspiration (EUS-FNA). However, this approach suffers from several limitations as discussed below.

The challenges to accurate characterization of suspect pancreatic neoplasia result from the relative inaccessibility of the pancreas given its anatomical location, the non-specific nature of symptoms, and the characteristic stromal reaction with intense fibrosis associated with both adenocarcinoma and chronic pancreatitis. This similarity significantly complicates attempts to differentiate the two similar appearing lesions by imaging, even with cytological evaluation of fine-needle aspirates (FNAs). Finding small nests of tumor cells in a sea of fibrosis is one major challenge; the differentiation of well-differentiated cancers from normal tissues, another key challenge is difficult to be achieved through cytology.

Figure 1.1 Early and accurate diagnosis of potentially curable pancreatic cancer patients is impossible in some cases with current diagnostic methods. The key challenge is distinguishing cancer from benign tissues, particularly in case of inflammation (chronic pancreatitis). Shown here is a clinical image from pancreatic EUS-FNA (endoscopic ultrasound-guided fine-needle aspiration), the diagnostic procedure-of-choice for tissue acquisition in suspect pancreatic cancer. It illustrates the lack of specific contrast afforded by ultrasound sensing alone [41]. The pancreatic mass is difficult to distinguish, and classification relies on cytology, which is often non-diagnostic.

EUS has emerged as an innovative imaging modality to provide access to the pancreas for tissue evaluation and is the current diagnostic procedure-of-choice for tissue acquisition in suspected pancreatic cancer (Fig. 1.1). While EUS imaging remains the most sensitive test to identify a pancreatic mass, determining whether the mass is benign or malignant remains problematic due to reliance on EUS-guided fine needle aspiration (FNA) sampling. Unfortunately, these FNA cytology samples are often non-diagnostic, leading to a negative predictive value of only 50-70%, given the high pre-test likelihood for cancer among the patients referred for the procedure [42]. For those patients with a strong clinical suspicion of pancreatic cancer, laparotomy to obtain tissue for those with

unresectable disease or an unnecessary resection for those with a resectable tumor may be performed.

This failure of accurate tissue characterization causes patients to undergo major surgery to reveal only benign or inflammatory disease on pathologic examination. The mortality of pancreatic surgery is in the range of 2-5% in experienced centers, with major morbidity of 20-25% [43]. In one study, as many as 9% of patients were reported to have undergone surgery for suspicion of cancer, only to reveal benign disease [44]. Recently, a prospective clinical study found that when chronic pancreatitis was present, EUS-FNA detected pancreatic adenocarcinoma with a sensitivity of only 54% [45] and a meta-analysis of 28 clinical studies concluded that EUS-FNA is an inadequate technique to rule out malignancy [42].

1.6 Optical Techniques for Pancreatic Disease

A variety of optical spectroscopic and imaging techniques have been attempted on cancerous and precancerous pancreatic tissues in animal models and human patients. (Fig. 1.2) Optical Coherence Tomography (OCT) has been employed to investigate the lesions of the main pancreatic duct in *in vivo* dog model [46], *ex vivo* human [47] and *in vivo* human [48] studies. Because it has a long penetration depth, OCT visualizes a layered epithelial structure and identifies characteristic patterns in malignant tissues. However, its sensitivity for identifying normal tissues is very low; thus OCT is non-diagnostic in distinguishing normal tissues from other benign lesions. Since OCT images cannot display cellular nuclei and organelles clearly due to insufficient resolution and providing only a back-scattered pattern of the layers, additional image interpretation by an expert is required for an accurate diagnosis. Needle-based confocal fluorescence

microscopy coupled with a cathepsin-activatable near-infrared probe (NIRF) has demonstrated that molecular imaging could be a sensitive tool for detecting an early stage of pancreatic cancer in an *in vivo* mice model study [49]. There is a regulatory issue of using the exogenous NIRF probe for human patients. Multi-center clinical trials results [50] on the needle based confocal laser endomicroscopy has reported a very low sensitivity (~ 58%) to detect pancreatic cystic neoplasms, probably because of the necessity of subjective interpretation of low resolution images. Non-linear optical microscopy has been proposed as a label-free and real-time method to characterize pancreatic histology at a cellular level [51]. However, the bulky and expensive instrumentation set up make it difficult to be translated into clinical practice. Although diffuse optical tomography (DOT) has been developed and showed feasibility in porcine tissue [52], it is still at the development stage and requires further technical and biological validations.

Optical scattering markers in duodenal mucosa have been investigated to predict the malignant changes in the pancreas based on the field effect theory [53]. A recent *in vivo* human study employing polarization gating spectroscopy [54] has revealed the diagnostic potential of detecting the increase in blood supply surrounding malignant tissues for identifying pancreatic cancer according to the field effect. However, the technology has critical limitations in distinguishing normal tissues from inflammatory tissues, which is currently the unmet clinical need. Previous *ex vivo* studies [22, 55-57] performed in our lab have shown that reflectance and fluorescence optical spectroscopy has potential as a label-free, rapid, quantitative, compact, cost-effective optical biopsy tool to address current clinical needs. None of the optical techniques introduced here except optical

spectroscopy are yet ready for clinical translation because of technical immaturity, insufficient clinical efficacy, inability to address critical unmet needs in a clinic or instrumental/cost limitations. However, many technical issues still remain to be addressed in translating optical spectroscopy into *in vivo* human study.

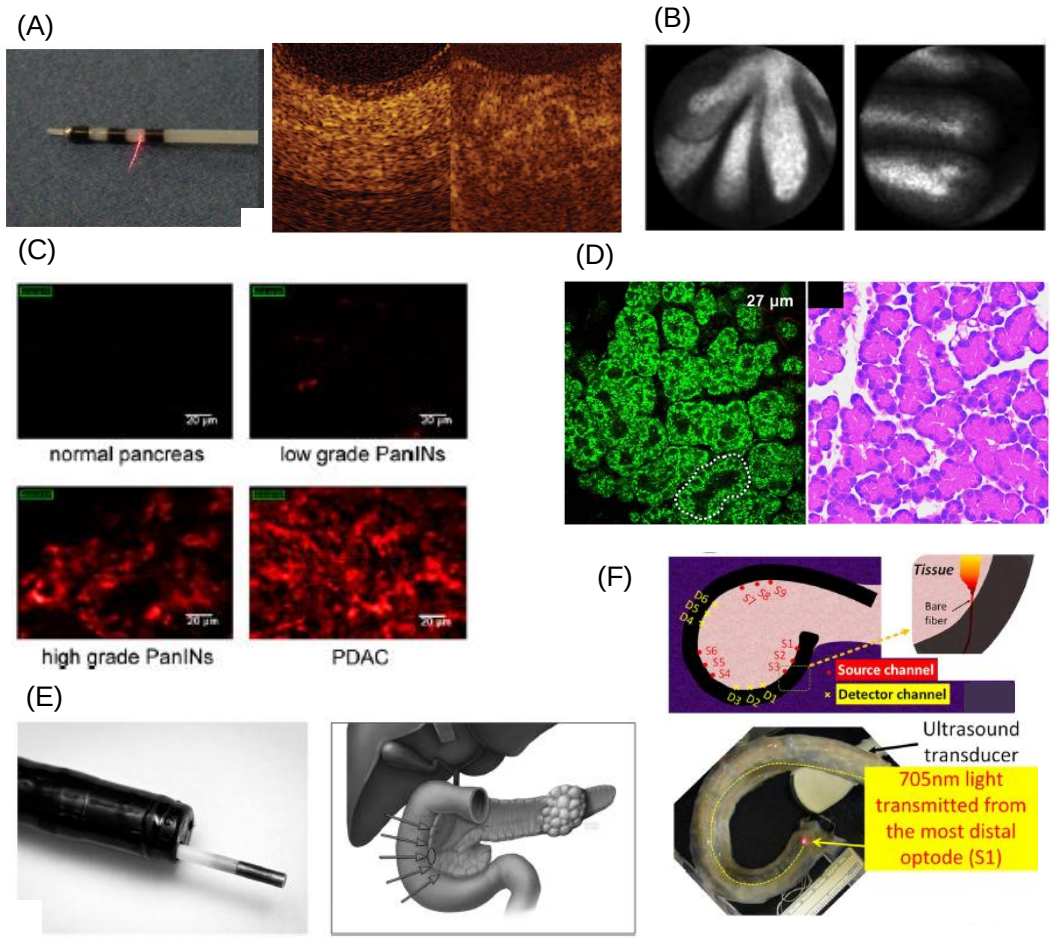

Figure 1.2 Types of optical techniques developed for pancreatic cancer diagnostics (A) left: OCT probe inserted inside Endoscopic retrograde cholangiopancreatography (ERCP) [47] right : obtained OCT images for normal (left) and tumor-involved main pancreatic duct sections [48] (B) needle based confocal laser endomicroscopy images on intraductal papillary mucinous neoplasm [50] (C) Near infrared probed confocal imaging in mouse model [49] (D) Nonlinear optical microscopy images (left) on normal rat pancreas compared to hematoxylin and eosin image (right)(E) Polarization gating spectroscopy probing duodenal mucosa in endoscopy channel [54] (F) Diffuse optical tomography technique in duodenoscope [52]

1.7 Dissertation Objectives

The main objective of this dissertation is to develop theoretical (mathematical and computational) and experimental (*i.e.* instrumental) tools to fill the gap between the current technology and the desired technology for human tissue optical sensing. Specific Aim 1 is focused on two different mathematical models for rapid and accurate quantification of human pancreatic tissue reflectance and fluorescence. Aim 2 involves the development of a new computational simulation method to evaluate fluorescence spectroscopy or imaging system in turbid media. Aim 3 concerns the instrumental design of optoelectronic microprobe that can be inserted into a hollow needle (~ 1 mm diameter) for optical sensing in a very limited space which even an endoscopic channel is unable to gain access.

Specific Aim 1: To develop and validate a mathematical model for rapid and accurate quantitative analysis of *ex vivo* human pancreatic tissues. Two different mathematical models will be developed to extract parameters associated with biophysical features or scattering properties in order to rapidly and accurately assess human pancreatic tissues freshly excised during the surgery.

Specific Aim 2: To devise and verify a computational method for the assessment or design of fluorescence spectroscopy or imaging system utilizing complex optics to probe turbid biological tissues. A new computational method will be developed by combining the conventional optical design software and the gold-standard Monte Carlo method, and will be verified computationally and experimentally.

Specific Aim 3: To design and fabricate a prototype of an optoelectronic microprobe for an accurate diagnosis of pancreatic cancer during the EUS-FNA procedure. Microfabrication technology will be employed to fabricate a prototype board assembled

with miniaturized die-level optoelectronic component, and their overall performance and optical sensing feasibility will be tested using the calibrated tissue optical phantoms.

1.8 Dissertation Overview

Chapter 2 describes the development and validation of a rapid semi-empirical model, called the Direct Fit Photon Tissue Interaction Model (DF-PTI), for quantitative characterization of precursor lesions of pancreatic cancer. The DF-PTI model extracts parameters associated with morphological and biochemical features from the first-ever optical spectroscopic measurement on human pancreatic pre-cancerous tissues.

Chapter 3 describes the development and validation of a simple scattering model of steady-state reflectance to evaluate the potential for real-time cancer detection using reflectance spectroscopy. The principal component analysis reveals that reflectance-only data has a e diagnostic performance comparable to that of the multi-modal approach. The simple and rapid scattering model is employed to analyze steady-state reflectance obtained from freshly excised human pancreatic tissues. The diagnostic power of scattering properties of pancreatic tissue in distinguishing malignant from non-malignant tissues will be evaluated utilizing a rigorous tissue classification algorithm.

Chapter 4 describes the basic principle of ray-traced Monte Carlo simulation method and its verification on computational tissue models and two-layered optical tissue-simulating phantoms.

Chapter 5 describes the design, fabrication, assembly, characterization and feasibility tests on the first prototype of an optoelectronic microprobe that is compatible with a hollow needle for accurate *in vivo* pancreatic cancer detection.

Chapter 6 summarizes and concludes the dissertation with a statement of its scientific contributions and a discussion of future works.

Chapter 2.
Mathematical Model on Diffuse Reflectance of Pancreatic Pre-Cancerous Tissues

2.1 Introduction

Pancreatic adenocarcinoma, the 4th leading cause of cancer death in the United States with a five-year survival rate of less than 7%, is often detected at late-stages of development when treatment is ineffective [58]. Intraductal papillary mucinous neoplasm (IPMN, Fig. 2.1) is a precursor lesion of pancreatic cancer, characterized by an intraductal proliferation of neoplastic cells with mucin production [59].

IPMN diagnosis, which could offer an opportunity to treat patients before they develop a potentially incurable pancreatic malignancy, may be challenging; identifying those IPMN with progression to malignancy remains an unmet medical need. Of the main imaging modalities employed to detect IPMN (computed tomography, endoscopic retrograde cholangiopancreatography, magnetic resonance cholangiopancreatography, and endoscopic ultrasonography (EUS)), EUS offers the highest resolution [60] and enables a cytologic diagnosis of IPMN via fine-needle aspiration (EUS-FNA). However, the sensitivity of EUS-FNA cytology diagnosis is low (44-75%) [61, 62] and the technique suffers from a steep learning curve and high inter-operator variability [63]. Thus, the effectiveness of identifying cancer precursor lesions such as IPMN could be improved by developing a more sensitive and quantitative detection method.

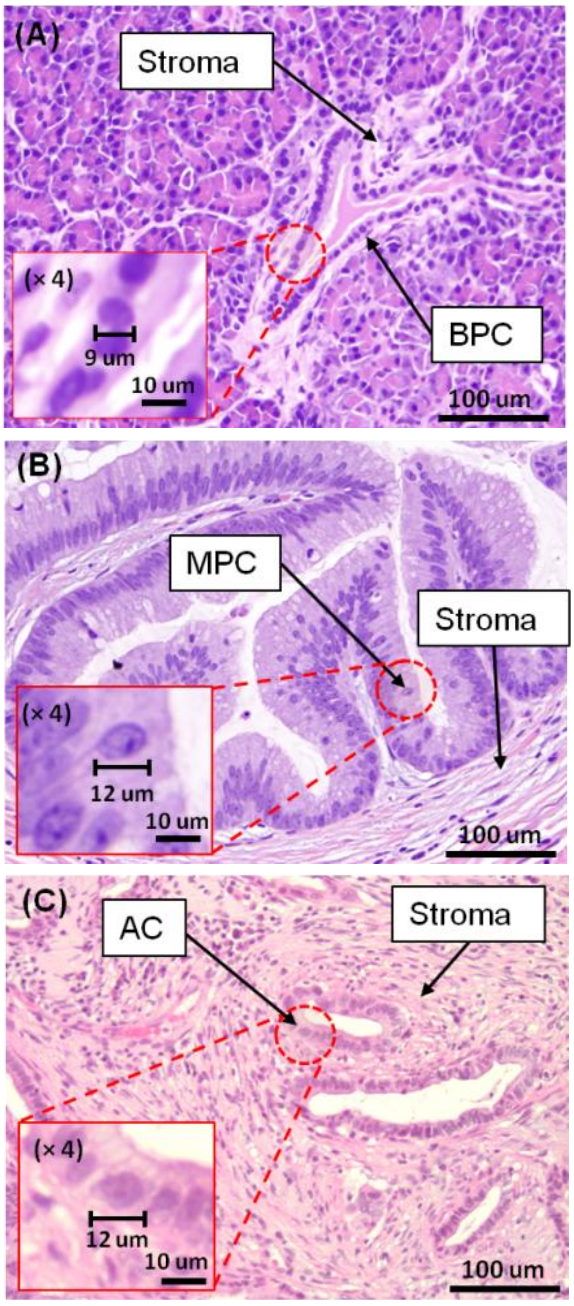

Figure 2.1 Representative histological images of (A) normal pancreatic ductal tissue (BPC: benign pancreatic cell), (B) IPMN (MPC: malignant pancreatic cell with enlarged nuclei), and (C) pancreatic adenocarcinoma (AC with enlarged nuclei). The nuclei and stroma have been stained purple (hematoxylin stain) and pink (eosin stain), respectively. Note that IPMN and AC tissues have similar biophysical features, including nuclear enlargement and abundant collagen surrounding cells, relative to normal tissues. These features can be analyzed by quantitative multimodal optical spectroscopy.

Optical spectroscopy has shown promise as a potential diagnostic tool for pre-cancer detection in various human tissues, including the cervix [64], the colon [65] and the breast [7]. Advantages of optical spectroscopy compared to current imaging modalities (listed above) include quantifying tissue morphological and biochemical alterations occurring at the molecular and cellular levels during neoplastic progression [66] and clinical compatibility with EUS-FNA procedures [67]. Previously, our group successfully distinguished human pancreatic diseases, including pancreatic adenocarcinoma (AC) and chronic pancreatitis, from normal tissues with multimodal optical spectroscopy and a mathematical photon-tissue interaction (PTI) model [22, 55, 56, 68].

Here, we report the first, to our knowledge, optical spectroscopic (reflectance and fluorescence) measurements from human pancreatic malignant precursor, IPMN. Because the study employed tissues obtained surgically, typically from patients with advanced disease, the opportunity to study IPMN (a cancer precursor) in patients was limited. For freshly excised pancreatic tissues (Fig. 2.1), we developed quantitative tissue-optics models to assess the biophysical similarities and differences between normal tissues, IPMN, and AC tissues.

2.2 Experimental methods

2.2.1 Instrumentation

A Reflectance and Fluorescence Lifetime Spectrometer (RFLS) [10], was employed to obtain reflectance and fluorescence spectra of human pancreatic tissues. A tungsten halogen lamp (HL 2000FHSA, Ocean Optics) provided white light (400-750 nm) for reflectance measurements; a pulsed laser at 355 nm (PNV001525-140, JDS Uniphase) provided fluorescence excitation light. Lamp and laser light was delivered to tissue via

two separate optical fibers with core diameters of 600 μm. Tissue reflectance and fluorescence light were collected by a third identical fiber and delivered to the detectors. Collected light was passed to a spectrograph (MS 125, Oriel Instruments) coupled to an intensified charge-coupled device camera (ICCD 2063, Andor Technology) to detect tissue reflectance (400-750 nm) and fluorescence (360-700 nm). The RFLS also measured time-resolved fluorescence decays, which are not discussed here. Data aquisition time for each modality was less than 1 s. All measured spectra were background subtracted, corrected, and normalized as in [10].

2.2.2 Human studies and data set

The study was approved by the Institutional Review Board of the Univ. of Michigan (U of M) Medical Center. Informed written consent was obtained from each patient. Optical data were acquired from freshly-excised human pancreas within 30 minutes of resection during pancreatic surgery. Measurements were taken at up to 10 sites on each tissue specimen, depending on specimen size. At each site, two reflectance and two fluorescence spectra were collected. For each tissue site, immediately after optical measurements were acquired, the site was biopsied by a clinical pathologist for histopathological tissue analysis to confirm diagnosis.

Table 2.1 Numbers of patients and analyzed tissue sites for each tissue type

Tissue Type	Number of Patients	Number of Analyzed Tissue Sites	
		Reflectance	Fluorescence
Normal	3	11	11
IPMN	2	8	5
AC	4	17	17

Table 2.1 summarizes the study. Two measurements on each site were averaged for analysis. The IPMN diagnoses were "IPMN with moderate dysplasia," as shown in Fig. 1. The 22 normal and 33 AC reflectance and fluorescence spectra from 11 and 17 sites, respectively, used for comparison with the IPMN data, were reported previously [68]. For one IPMN patient, fluorescence spectra were not recorded due to misalignment. Among 18 measured IPMN reflectance spectra from 9 sites, two spectra from one site were excluded by the exclusion criteria $R_{550\ nm}/R_{650\ nm} < 0.1$ [12, 14] due to excessive blood absorption.

2.2.3 Direct Fit PTI model for steady-state reflectance and fluorescence

A PTI model for reflectance and fluorescence spectra was reported [22, 68]. The model employed a semi-empirical reflectance equation to extract absorption- and scattering-related tissue parameters from measured reflectance spectra. The empirical model was described as a function of the tissue scattering coefficient (related to the cellular nuclear diameter *L*, nuclear refractive index n_s, and cellular density [*Cell*]) and the tissue absorption coefficient (related to a linear combination of oxygenated [*oxy-Hb*] and deoxygenated [*deoxy-Hb*] hemoglobin concentration). In this model, nuclear diameter, total hemoglobin concentration and oxygen saturation were freely varied for fitting with remaining variables fixed.

Here, a Direct Fit PTI (DF-PTI) model was developed and employed with seven main modifications to the previous model [12] : 1) to improve fit quality at all wavelengths, the semi-empirical model was fit directly to the measured data without a "canonical normal" spectrum, 2) the wavelength range for fitting was expanded from 700 nm to 750 nm to more accurately account for the effect of cellular nuclear size and refractive index on

spectrum shape [69], 3) the cost function was minimized with a nonlinear least-squares iterative algorithm, 4) bilirubin *[Bilirubin]* was added as an absorber [67], 5) collagen concentration *[Collagen]* and cellular density *[Cell]* were freely varied, 6) nuclear refractive index was freely varied, as the refractive index is related to tissue malignancy [70], and 7) the mean vessel radius R_v was freely varied [71]. In the original PTI model, mean vessel radius was fixed at 7 μm and the absorption coefficient of whole blood was employed for the vessel packaging correction factor. In the DF-PTI model, the blood absorption in the capillary network was modeled with a varying vessel radius size and blood volume fraction (ρ) [72]. The ranges of varied tissue parameters employed in the DF-PTI model are shown in Table 2.2

Table 2.2 Ranges of all the varied tissue parameters in the DF-PTI reflectance model

Parameters	L	n_s	[*Cell*]	[*Collagen*]	[*oxy-Hb*] [*deoxy-Hb*]	R_v	ρ	[*Bilirubin*]
Min. Value	8 μm	1.37	5.6×10^7 (/cm^3)	1.0×10^6 (/cm^3)	0 μM	7μm	0	0 μM
Max. Value	14 μm	1.40	8.4×10^7 (/cm^3)	1.0×10^7 (/cm^3)	50 μM	20μm	0.15	40 μM

For each tissue measurement, the scattering coefficient calculated via the best DF-PTI reflectance fit was employed to correct the corresponding fluorescence spectrum for attenuation [22]. As measurements were *ex vivo* and local blood content could vary over time, only the extracted scattering, and not absorption, coefficient was employed to calculate intrinsic fluorescence, while hemoglobin and bilirubin concentrations were varied when calculating intrinsic fluorescence. The resulting intrinsic fluorescence spectra were fit to a linear combination of basis spectra of three endogenous tissue

fluorophores: nicotinamide adenine dinucleotide (NADH, 450-500 nm emission peak), flavin adenine dinucleotide (FAD, 500-600 emission peak) and collagen (400-450 emission peak) [22]. The best fit provided the fractional contribution of each fluorophore to the intrinsic fluorescence.

2.3 Results and Discussion

2.3.1 Comparison between PTI model and DF-PTI model

Figure 2.2 compares the fitting results of the (A) PTI model and the (B) DF-PTI model. Analyzed reflectance spectra were collected from a tissue site confirmed to be IPMN with moderate-grade dysplasia. In the wavelength range 450–530 nm, which is related to nuclei scattering [55], the DF-PTI showed improved fit accuracy compared to the PTI model. In the Soret (400 – 420 nm) and alpha/beta bands (500 – 540 nm) of hemoglobin absorption, the DF-PTI showed improved fit accuracy compared to the PTI model. In the slope after 620 nm (attributed to tissue scattering) [67], the DF-PTI showed improved fit accuracy compared to the PTI model. The mean percent error of the DF-PTI model was less than 2 %, which showed a better accuracy than the PTI (~8%). The execution time for DF-PTI model fitting procedure on each site was less than 2 seconds, reduced from > 30 seconds for the PTI model.

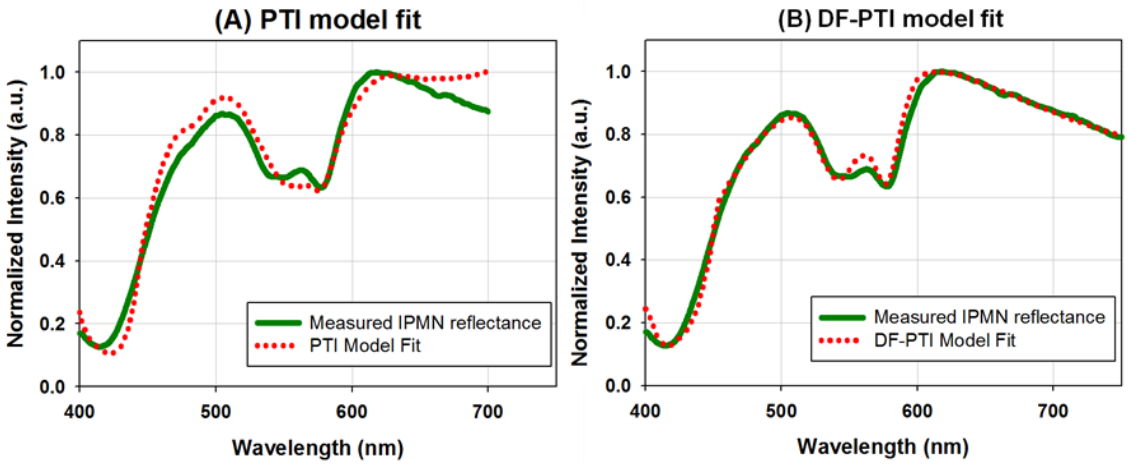

Figure 2.2 Representative model fitting results on measured IPMN reflectance spectra using (A) the original PTI model, and (B) the developed DF-PTI model. Solid green lines indicate measurement IPMN reflectance and dotted red lines indicate each model fit.

2.3.2 Reflectance analysis

Figure 2.3 (A) shows the average of all normalized reflectance spectra from human pancreatic tissues: normal, IPMN with moderate dysplasia, and AC tissues. The features in the 400-440 nm and 540-580 nm ranges were attributed mainly to hemoglobin absorption. The higher reflectance in the 450-530 nm range in IPMN and AC sites was attributed to the cellular density and nuclear size [22, 68]. Figure 2.3 (B) shows wavelength-dependent standard errors of the mean spectra for each tissue type. It is noted that standard errors are greatest in the wavelength range related hemoglobin absorption. Figure 2.3 (C) shows a representative PTI model fit to IPMN reflectance. Mean percent error between measured data and fit for all the measurements was less than 5% in the range 450-750 nm. The mean values of extracted nuclear diameters and refractive indices from IPMN measurements were larger than those from normal tissues (Table 2.3)

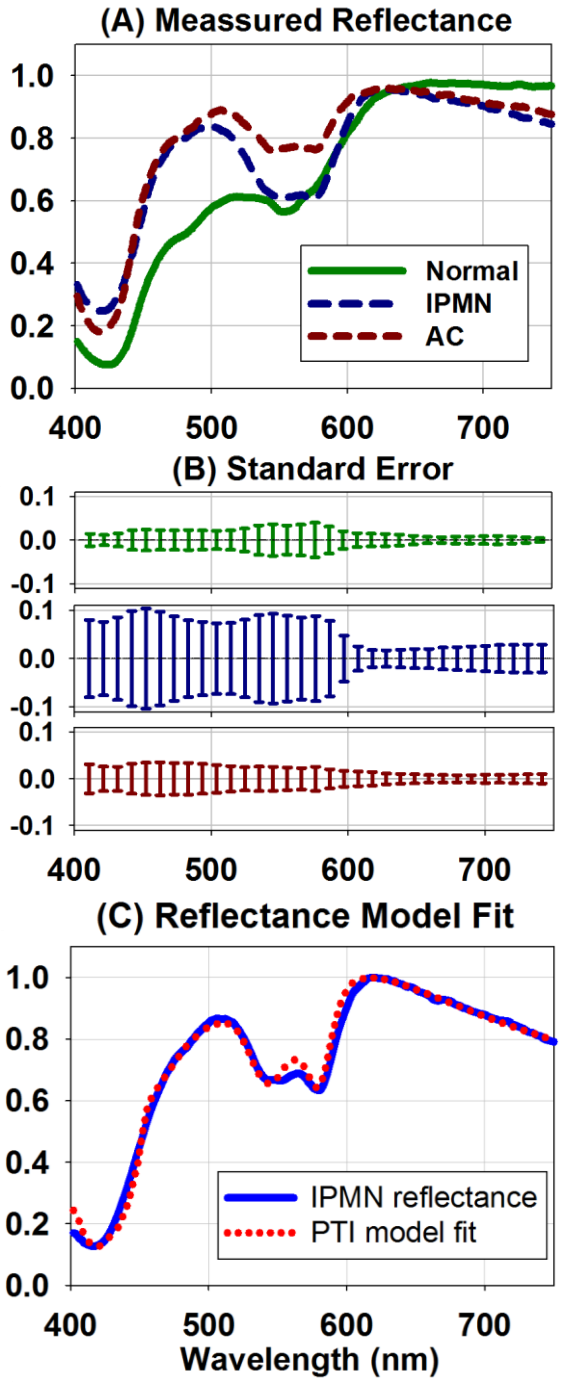

Figure 2.3 Quantitative analysis of measured reflectance spectra can distinguish IPMN and AC from normal pancreas. (A) Mean of normalized reflectance spectra obtained from human pancreatic normal tissues, IPMN with moderate dysplasia, and AC. (B) Wavelength-dependent standard error bars of mean measured spectra for each tissue type. (C) Representative PTI model fit for IPMN reflectance.

The mean extracted nuclear sizes are consistent with histology (Fig. 2.1), indicating nuclear enlargement both in IPMN and AC relative to normal pancreas. Additionally, the ratio of the extracted nuclear size of AC to normal tissue (11.64/8.89 = 1.30) is consistent with the previously reported nuclear dilation factor L/L_0 (1.27 ± 0.01) [68]. The result for mean extracted refractive index of normal pancreas (1.372) was consistent with previous reports [22, 68]. The extracted nuclear refractive indices of IPMN and AC were larger than that of normal pancreas. This finding is consistent with studies reporting that dysplastic cell nuclei have larger refractive indices than normal nuclei due to the higher DNA content and concentrations of nucleic acids in dysplastic cells relative to normal cells [70, 73].

Here, variations in local tissue blood content arising from the experimental protocol (tissue dissection prior to optical measurement) preclude the reporting of tissue absorption-related parameters. We note that mean estimated vessel radii were 11 to 13 μm for all tissue types. Larger estimated vessel radius (compared to previously employed 7 μm), with the inclusion of fractional blood volume, produced more accurate fits within the Soret absorption band.

Table 2.3 Extracted parameters related to tissue scattering for each tissue type

Tissue Type	Nuclear diameter	Refractive index	Cell Density	Collagen Density
Normal	8.89 ± 0.13 μm	1.372 ± 0.002	$8.07 \pm 0.12 \times 10^7/cm^3$	$1.28 \pm 0.16 \times 10^6/cm^3$
IPMN	11.50 ± 0.88 μm	1.394 ± 0.004	$7.15 \pm 0.09 \times 10^7/cm^3$	$6.15 \pm 1.56 \times 10^6/cm^3$
AC	11.64 ± 0.37 μm	1.396 ± 0.002	$7.21 \pm 0.09 \times 10^7/cm^3$	$8.58 \pm 0.62 \times 10^6/cm^3$

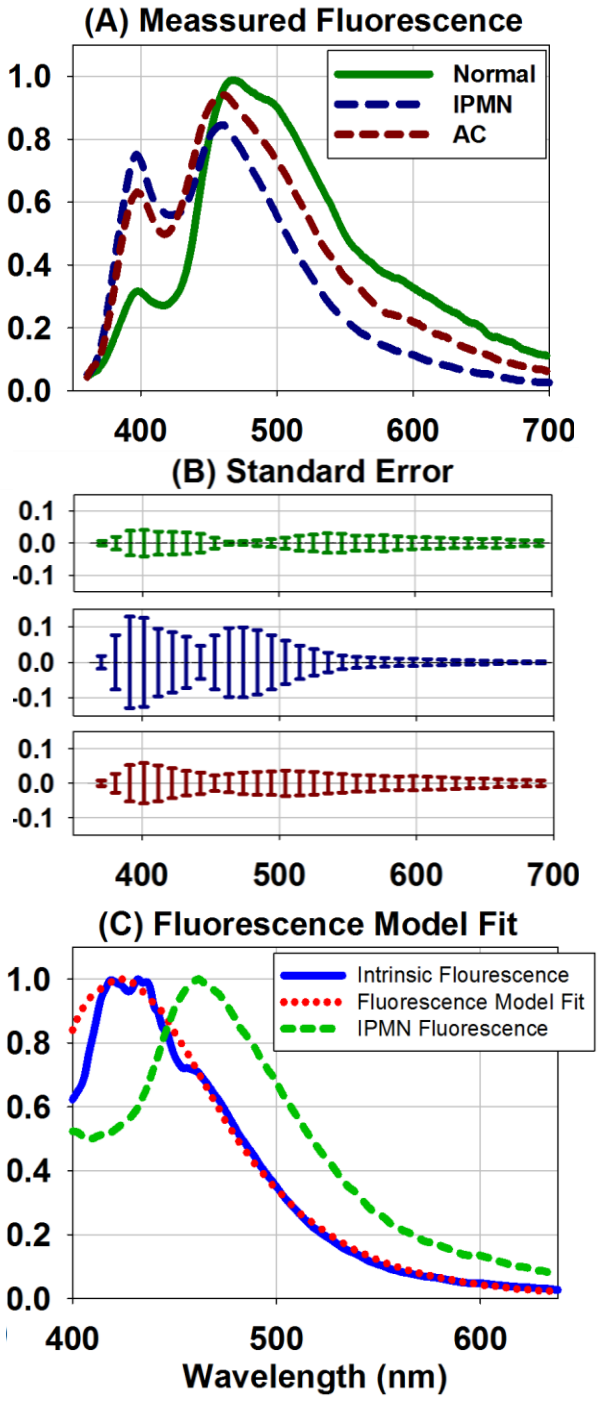

Figure 2.4 Quantitative analysis of measured fluorescence spectra can distinguish IPMN and AC from normal pancreas. (A) Mean of normalized fluorescence spectra obtained from human pancreatic normal tissues, IPMN with moderate dysplasia, and AC. (B) Wavelength-dependent standard error of mean spectra for each tissue type. (C) Representative PTI model fit for IPMN intrinsic fluorescence

2.3.3 Fluorescence analysis

Figure 2.4 (A) shows the average of all normalized fluorescence spectra from human pancreatic normal, IPMN, and AC tissues. Fluorescence spectra included contributions from intracellular NADH and FAD, and from stromal collagen, with emission peaks around 470 nm, 540 nm, and 430 nm, respectively. Although measured fluorescence spectra were attenuated by hemoglobin absorption, notable spectral differences between normal and diseased pancreas were apparent. Figure 2.4 (B) shows the wavelength-dependant standard error of the mean spectra for each tissue type, with higher variation in the wavelength band attributed to hemoglobin absorption. Intrinsic fluorescence was calculated from measured fluorescence (Fig. 2.4 (C)). Mean percent error of fitting intrinsic fluorescence in the range 400-550 nm was under 7%.

The extracted percentage contribution from collagen emission to the intrinsic fluorescence for normal, IPMN, and AC tissues were 45.4 ± 7.3 %, 92.2 ± 3.4 % and 76.1 ± 5.4 %, respectively. The collagen contribution to the intrinsic tissue fluorescence was greater for IPMN and AC tissues than for normal pancreas. This result is consistent with histological findings (Fig. 2.1), which indicate a collagen-rich stroma in IPMN and AC relative to normal pancreas. The increase of extracellular collagen content in IPMN and AC relative to normal pancreas arises from a fibrotic response during disease development, with collagen surrounding IPMN being more mature and with denser organization, since it is formed more slowly than collagen surrounding pancreatic AC, which is immature and newly formed in the process of tumor-induced desmoplasia (abundant fibrotic stroma) [74].

2.4 Conclusion

The DF-PTI model was developed and employed to quantitatively analyze reflectance spectra from pre-cancerous human pancreatic tissues. The DF-PTI model is faster and fits measured data more accurately (over a wider wavelength range) than previously-reported models.

The analysis results suggest that multimodal tissue optical spectroscopy coupled with quantitative tissue-optics models can characterize intraductal papillary mucinous neoplasm (IPMN), a cancer precursor in human pancreatic tissues. The analysis developed here assessed parameters associated with cellular nuclear size, nuclear refractive index, and tissue collagen content, and the results were consistent with known histopathology for these tissues.

Parameters extracted from model fits to reflectance and fluorescence data distinguished IPMN tissues from normal pancreas and closely associated IPMN tissues with pancreatic cancers. Thus, optical characterization of IPMN tissues, which have similar optical scattering properties to adenocarcinoma, could enable early clinical intervention, including follow-up examinations to monitor progression to malignancy with the goal to intervene prior to development of an incurable pancreatic cancer.

Chapter 3.
Quantitative Analysis for Real-time Pancreatic Cancer Detection

3.1 Introduction

For a minimally-invasive and accurate diagnostic tool for pancreatic cancer detection, a multimodal optical spectroscopy was previously developed to demonstrate the first optical spectroscopic assessment on a mouse xenograft model and freshly excised human pancreatic tissues [55]. Also, a mathematical model called photon tissue interaction (PTI) model based on a semi-empirical model was previously developed to provide the first quantitative link between pancreatic tissues histology and the obtained reflectance and fluorescence spectra [22]. For accurate diagnostics, tissue classification algorithm based on a linear discriminant analysis employing the spectral area and ratio, was created on the dataset of nine patients consisting of 96 fluorescence and reflectance measurements: 33 measurements from 17 adenocarcinoma sites, 41 from 22 pancreatitis sites and 22 from 11 normal sites [56]. The PTI model has been validated on the same dataset to reveal that the extracted biophysically-relevant parameters such as nuclear enlargement factor and collagen fluorescence contribution can distinguish adenocarcinoma from pancreatitis and normal tissue with statistical significance [57].

However, the previous studies suffer from a limited patient population, which made it difficult to draw a convincing conclusion about the diagnostic accuracy of optical spectroscopy. Furthermore, multiple sites were measured per patient, leading to intra-patient correlation. Thus, a more statistically-rigorous classification algorithm is required

on a larger patient number to more accurately assess the diagnostic accuracy. Using that tissue classification algorithm, a different analysis model could be tested for accurate and rapid quantification method for real-time pancreatic detection. In this chapter, we present tissue classification results employing a principal component analysis on both reflectance and fluorescence data obtained from 18 patients. The results show that reflectance data only has the classification performance comparable to the combination of the reflectance and fluorescence spectroscopy. Based on this finding, we further introduce the scattering model to analyze pancreatic tissue reflectance and describe the diagnostic capabilities of scattering properties of human pancreatic tissues.

3.2 Materials and Methods

3.2.1 Instrumentation

A clinically-compatible reflectance spectroscopy and fluorescence system [10] was employed in the study. In this work, we have focused on characterizing pancreatic tissue via reflectance spectroscopy. Also, the detailed descriptions about a setup for fluorescence spectroscopy and data processing can be found in the literature [75].

With our focus on reflectance, the instrumental set up for reflectance measurements consisted of a tungsten-halogen lamp (HL 2000FHSA, Ocean Optics, Dunedin, FL) as a broadband light source, a spectrograph (MS 125, Oriel Instruments, Stratford, CT) coupled with an ICCD (2063 Andor Technology, Belfast, Northern Ireland) for recording spectrum, and a hand-held optical probe to deliver and collect light to and from pancreatic tissues (Fig 3.1 (a))[55]. The probe had two multi-mode optical fibers for source and detector (600 μm core diameter and 660 μm center-to-center spacing). Spectra

were collected in the range from 460 nm to 760 nm with 0.7 nm spectral resolution. Acquisition time for one spectrum was less than 0.5 seconds.

To correct measured tissue reflectance for instrument artifacts, measured spectrum $R_{TISSUE\_meas}(\lambda)$ was background-subtracted and calibrated for spectral response of the system. The dark background $R_{BG\_meas}(\lambda)$, was measured prior to every reflectance acquisition. The spectral response, $R_{REF\_meas}(\lambda)$ was acquired by placing a probe at fixed distance (6 mm) from a 50% diffuse reflectance Spectralon standard (SRS-50-010, Labsphere, North Sutton, NH) before the surgery began. Known reflectance of the diffuse standard, $R_{REF\_known}(\lambda)$, was multiplied to the corrected spectrum, generating a relative tissue reflectance to the standard, $R_{TISSUE}(\lambda)$ (Eg.3.1) .

$$R_{TISSUE}(\lambda) = R_{REF\_known}(\lambda)\left(\frac{R_{TISSUE\_meas}(\lambda) - R_{BG\_meas}(\lambda)}{R_{REF\_meas}(\lambda) - R_{BG\_meas}(\lambda)}\right) \qquad \text{Equation 3.1}$$

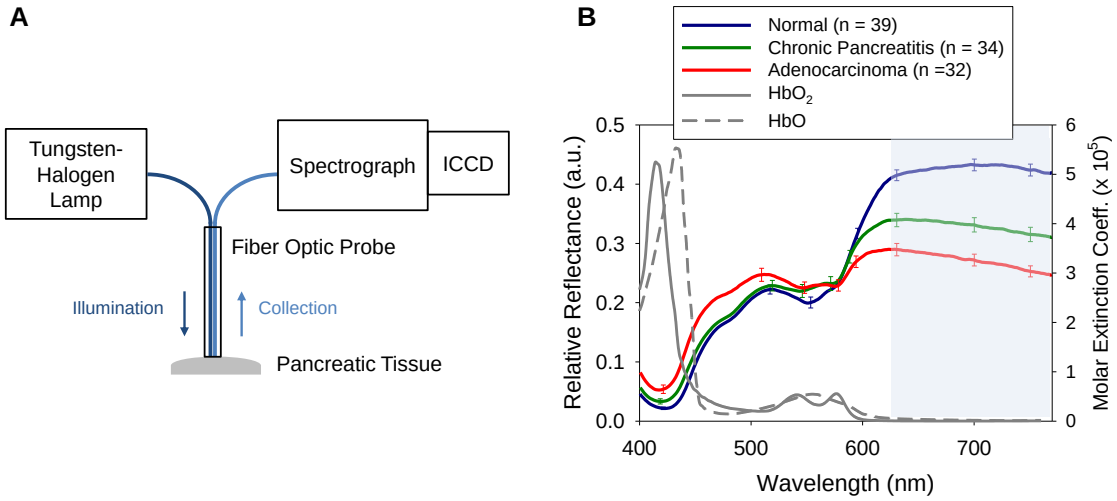

Figure 3.1 (A) Schematic of the fiber-optic-based instrument and its advantages for clinical usage. The instrument has a compact configuration inside a clinically-compatible mobile cart. Acquisition time is less than 0.5 s, enabling real-time analysis without patients' motion artifact. Unlike aspiration cytology, non-invasive optical measurement enables to examine intact tissues with the interrogation volume of 1 mm^3, which is a typical FNA volume. Smaller fiber optic probe can be employed to be compatible with the EUS-FNA needle. All technical feature makes reflectance spectroscopy suitable for a

real-time optical biopsy tool (B) Mean measured reflectance spectra (solid- colored lines, left y-axis) for three pancreatic tissue types using the instrument and molar extinction coefficients of oxygenated and deoxygenated hemoglobin (solid-gray and dashed-gray, right y axis). Error bars for the mean spectra represent the standard error. Blue-shaded region indicates a wavelength window (> 630 nm) that is relatively independent from tissue absorption (mainly due to hemoglobin) and show a distinctive difference between pancreatic tissue types. Thus, this wavelength range is of our interest for tissue scattering analysis.

3.2.2 Human Study

Reflectance data was collected from 18 patients who underwent pancreatic surgery (age 36 to 79, mean ± SD = 62.9 ± 11.3; 5 males and 13 females). Study was approved by the Institutional Review Board of University of Michigan and consent was acquired from the patients prior to all measurements. Within 30 minutes after pancreas was excision, a pathologist accessed pancreatic tissue sites for optical measurement. The end of the fiber optic probe was placed in contact with the tissues sites and two measurements were performed sequentially. Depending on the sample, up to 10 sites were measured. Immediately after data acquisition, the pathologist collected a biopsy from the same site. Biopsied tissue was approximately 3-5 mm in diameter which corresponds to optical interrogation volume of ~ 1 mm^3 in this study. Obtained biopsies were fixed in formalin, paraffin-embedded, sectioned and stained with hematoxylin and eosin for histologic examination. Histology confirmed 39 normal sites from 9 patients, 34 pancreatitis sites from 9 patient and 32 adenocarcinoma sites from 8 patients were analyzed. Some different tissue types were measured from the same patient. Of the total of 117 sites, 12 sites were excluded due to excessive blood content or low SNR.

3.2.3 Principal Component Analysis

To investigate the diagnostic capability of reflectance and florescence data for classifying malignant tissue from non-malignant tissues, a Principle Component Analysis (PCA)

model was employed to extract the principal components from each reflectance and fluorescence spectrum. The inputs to the PCA code were the corrected and normalized reflectance and fluorescence spectra. The PCA code was written in MATLAB using a native MATLAB function.

3.2.4 Rapid and Simple Scattering Model for Reflectance Analysis

Although the reflectance spectra were acquired in the wavelength range from 460 to 760 nm, only the range from 630 to 760 nm was analyzed to extract tissue scattering parameters. It's because that the absorption by major chromophores in human tissues is negligible and the acquired spectra of each pancreatic tissue type showed a distinctive difference (Fig. 3.1(b)) in this range. Without absorption, it was observed there was a linear relationship between the reflectance and the reduced scattering coefficient [15]. Thus, tissue reflectance was simply modeled using (Eq. 3.2).

$$R_{TISSUE} = a\mu'_s + a_0 \qquad \text{Equation 3.2}$$

Here, the coefficients of a and a_0 values were obtained by a linear fitting of measured reflectance values on manufactured tissue-simulating phantoms described in detail in Fig. 3.2. The reduced scattering coefficients of manufactured phantoms ranged from 5 to 20 cm^{-1} within a typical range for human tissues [76]. The wavelength-resolved reduced scattering coefficient was modeled using power law dependence on the wavelength (Eq 3.3), which is widely accepted in biomedical optics [76, 77].

$$\mu'_s(\lambda) = \mu'_s(\lambda_0)(\lambda / \lambda_0)^{-\gamma} \qquad \text{Equation 3.3}$$

$\mu'_s(\lambda_0)$ was the reduced scattering coefficient value at the reference wavelength, 630nm and the exponent γ was defined as scattering power, which was known to be related to

average scatterer size [78, 79]. This simple scattering model based on power law dependence fitted the corrected tissue reflectance to extract two scattering parameters $\mu'_s(630)$ and γ. The fitting range of $\mu'_s(630\ nm)$ was limited to a typical value of human tissues and the scattering power γ was $0.2 < \gamma < 4.0$ from theoretical [80] and experimental [81] results. A nonlinear least squares algorithm was employed for rapid fitting procedures and the process time per one spectrum was less than a hundred milliseconds.

3.2.5 Phantom Calibration

Solid phantoms were made using an agarose (161-3101, Bio-Rad Laboratories, Hercules, CA) according to the literature published recipe [76]. Briefly, 0.2 g of agarose powder was added to boiling DI water (20mL) and dissolved. The, the mixture was cooled at room temperature until ~ 80 ˚C. Before reaching 60 ˚C, either 0.4, 0.8, 1.2 and 1.6 mLs of 20% Intralipid (I141, Sigma-Aldrich, St. Louis, MO) were added to different agarose solutions as a scattering agent and thoroughly stirred until the solution was homogeneous. At 40 ˚C, the mixed solution was transferred into a glass beaker to solidify, which took about two hours. Resulting phantom is a solid cylinder with a diameter of 40 cm and a depth of 3 cm.

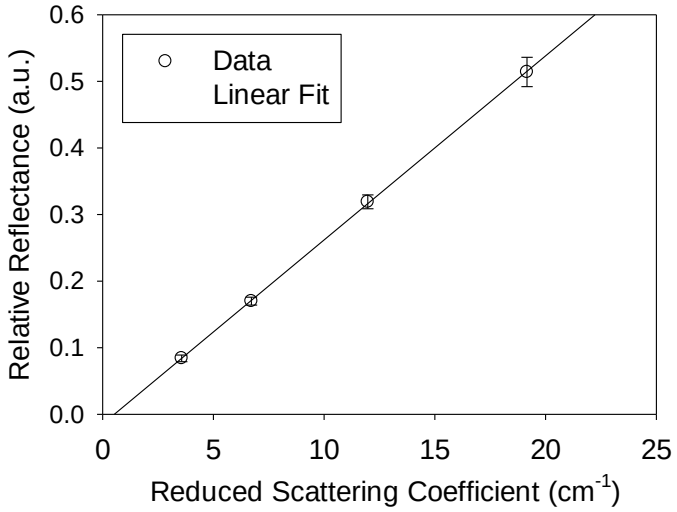

Figure 3.2 Linear relationship ($R^2 = 0.99$) between the measured relative reflectance and reduced scattering coefficients of the scattering phantoms with no absorbers. Error bars present standard deviation. The range of reduced scattering coefficients, from 10 to 20 cm^{-1} is relevant to human pancreatic tissues.

Reduced scattering coefficient of each phantom was determined by an integrating sphere (RT-60-SF, Labsphere, North Sutton, NH) setup and an inverse adding-doubling algorithm [82]. Reduced scattering coefficients at 630nm of four phantoms were calculated to be 3.6, 6.7, 12.0 and 19.2 cm^{-1}, respectively. Manufactured phantoms were also measured by reflectance spectroscopy. Four sites were measured on each phantom. Measured phantom spectra were background-subtracted and calibrated. Linear regression was performed on reflectance data with the corresponding reduced scattering coefficients to determine the coefficients of a and a_0

3.2.6 Statistical Analysis and Performance Metrics

For the initial comparison, a two-sided Wilcoxon rank sum test was performed to assess the ability of each scattering parameter to discriminate three tissue types. To evaluate their classification ability in a more statistically-rigorous way, a multinomial logistic

regression using Generalized Estimating Equations (GEE) model [83, 84] was employed in a "leave-two-patients-out" cross-validation method. The GEE accounted for the correlation among sites measured from the same patients [85, 86]. In the cross validation, dataset was split into 9 training sets and testing sets including 16 patients and 2 patients, respectively. The classification algorithm was run for each of the 9 training and testing sets. In each run, multinomial logistic regression was carried out on the training set to obtain fit coefficients using tissue type information determined by histopathology. Those fit coefficients were used as inputs for GEE. Optical diagnosis probabilities were calculated by using fit coefficients and scattering parameters from the testing set.

A threshold was then applied to these probabilities to determine sensitivity and specificity for all different classifications including malignant vs. benign (normal and pancreatitis), which is considered a current clinical need, disease (adenocarcinoma and pancreatitis) vs. normal, adenocarcinoma vs. normal, adenocarcinoma vs. pancreatitis and pancreatitis vs. normal. Confidence intervals for sensitivity and specificity were calculated using Wilson score interval with continuity correction [87]. Receiver operator characteristics (ROC) analysis curves also evaluated the classification ability of scattering parameters along with the area under curve (AUC) values.

3.3 Results

3.3.1 PCA Analysis and Classification Results

The first three reflectance and fluorescence principal components, their scores, and their statistical significance for distinguishing between the tissue types are displayed in Fig. 3.3. The first reflectance principal component score (*RPC1*) and the first fluorescence principal component score (*FPC1*) were the most statistically significant ($p < 0.01$) for

distinguishing adenocarcinoma from normal pancreatic tissue, distinguishing adenocarcinoma from chronic pancreatitis, and distinguishing chronic pancreatitis from normal pancreas.

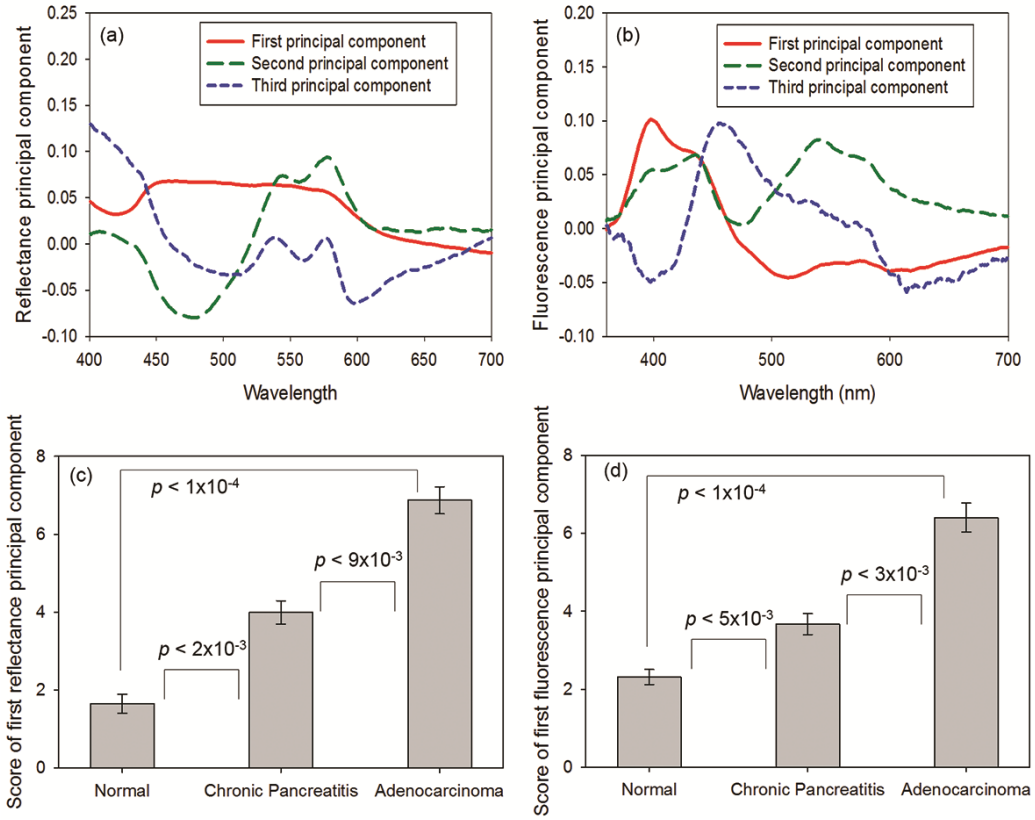

Figure 3.3 (A, B) First three principal components (accounting for 95% of the spectral variation) of the reflectance (A) and fluorescence (B) data sets. (C, D) Parameters extracted from principal component analysis (PCA) of tissue optical spectra, shown with their statistical significance for tissue classification. (C) The first reflectance principal component score was statistically significant for distinguishing adenocarcinoma from normal pancreatic tissue ($p < 1x10^{-4}$), distinguishing adenocarcinoma from chronic pancreatitis ($p < 9x10^{-3}$), and distinguishing chronic pancreatitis from normal pancreatic tissue ($p < 2x10^{-3}$). (D) The first fluorescence principal component score was also statistically significant for distinguishing adenocarcinoma from normal pancreatic tissue ($p < 1x10^{-4}$), distinguishing adenocarcinoma from chronic pancreatitis ($p < 3x10^{-3}$), and distinguishing chronic pancreatitis from normal pancreatic tissue ($p < 5x10^{-3}$). To remove negative values for ease of display, an offset of 4 was added to all principal component scores before they were plotted on the bar graph.

Variables from the PCA model were input into the tissue classification algorithm to distinguish between adenocarcinoma, chronic pancreatitis, and normal pancreas. The outputs of the classification algorithm were the optical diagnosis probabilities *P(N)*, *P(CP)*, and *P(A)* of each tissue site being normal, chronic pancreatitis, or adenocarcinoma, respectively. Ternary plots of the optical diagnosis probabilities *P(N)*, *P(CP)*, and *P(A)* were created for classification procedures that used both reflectance and fluorescence (Fig. 3.4), as well as reflectance only and fluorescence only (Fig. 3.5).

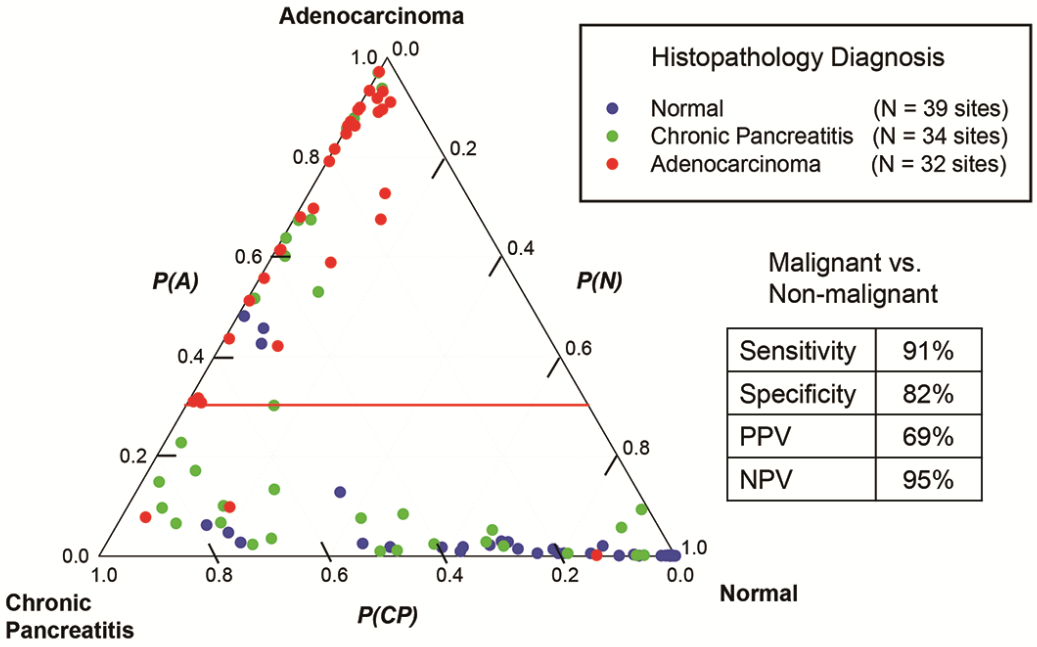

Figure 3.4 Ternary plot of optical diagnosis probabilities (probability *P(N)* that a tissue site is normal; probability *P(CP)* that the site is chronic pancreatitis; probability *P(A)* that the site is adenocarcinoma), as determined by principal component analysis. The tissue sites are color-coded according to histopathological diagnosis. Shown alongside the ternary plot are the sensitivity, specificity, positive predictive value (PPV), and negative predictive value (NPV) for distinguishing malignant (adenocarcinoma) tissue sites from non-malignant (normal and chronic pancreatitis) tissue sites. Parameters from reflectance (first three principal component scores) and fluorescence (first principal component score) were both used in this method, and one threshold (*P(A)* > 0.3; red line) was employed to achieve the shown classification accuracy.

The resulting sensitivity, specificity, PPV, and NPV for distinguishing adenocarcinoma from non-cancerous tissues (Table 3.1) were calculated using cross-validation to be 91%, 82%, 69%, and 95%, respectively. The corresponding area under the ROC curve was 0.89 for the algorithm including both reflectance and fluorescence PCA parameters. These results show the high diagnostic accuracy of the optical method employing both reflectance and fluorescence, as described in this report. Additional variations of the classification algorithm were run to compare the results obtained by using only reflectance variables (*RPC1*, *RPC2*, *RPC3*) and only fluorescence variables (*FPC1*, *FPC2*) with those obtained by using a combination of reflectance and fluorescence variables (*RPC1*, *RPC2*, *RPC3*, *FPC1*). For these comparisons, thresholds were manually selected such that the resulting sensitivity was the same (91%) for all three algorithms, and then the corresponding specificity, PPV, and NPV of the three algorithms were compared.

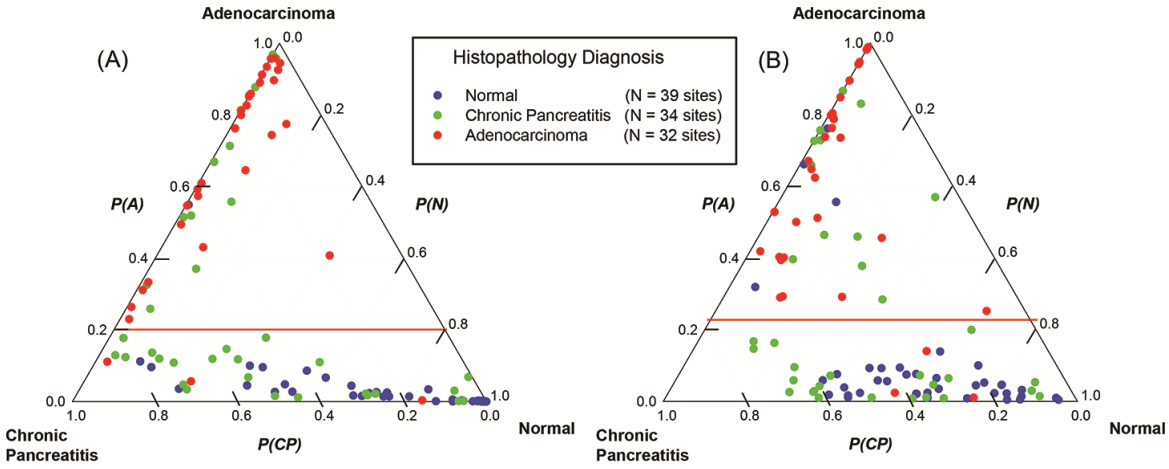

Figure 3.5 Ternary plots of optical diagnosis probabilities (probability *P(N)* that a site is normal; probability *P(CP)* that the site is chronic pancreatitis; probability *P(A)* that the site is adenocarcinoma), as determined by optical spectroscopy with principal component analysis, using reflectance data only (A) and fluorescence data only (B). The tissue sites are color-coded according to histopathological diagnosis

Using only reflectance variables, and choosing the threshold of *P(A)* > 0.20 for cancer diagnosis, the sensitivity, specificity, PPV, and NPV for distinguishing adenocarcinoma from non-cancerous tissues were 91%, 84%, 71%, and 95% (Table 3.1). The area under the ROC curve was 0.89 when only reflectance variables were employed (Fig. 3.6). Using only fluorescence variables, and choosing the threshold of *P(A)* > 0.22 for cancer diagnosis, the sensitivity, specificity, PPV, and NPV for distinguishing adenocarcinoma from non-cancerous tissues were 91%, 78%, 65%, and 95% (Table 3.1). The area under the ROC curve was 0.86 when only fluorescence variables were employed (Fig. 3.6).

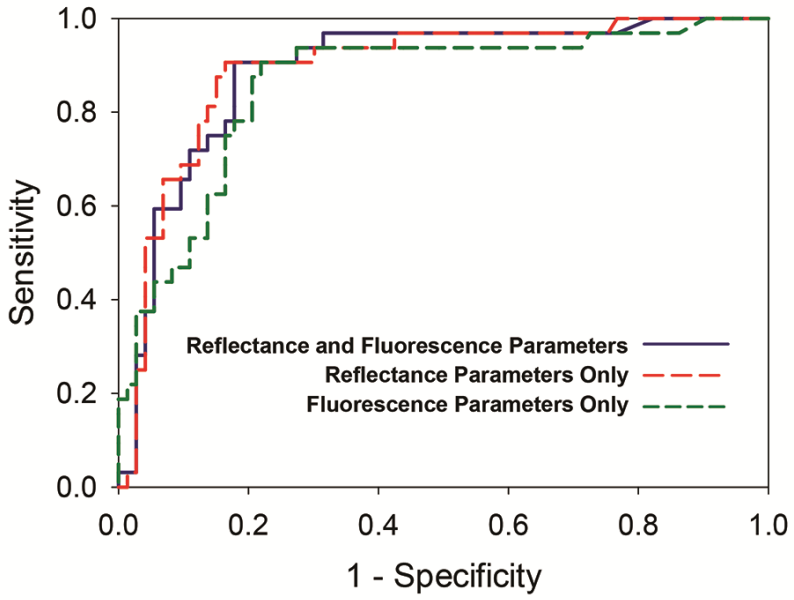

Figure 3.6 Receiver operating characteristic (ROC) curves for distinguishing malignant (adenocarcinoma) tissue sites from non-malignant (normal and chronic pancreatitis) tissue sites using PCA parameters from both reflectance and fluorescence data (solid blue line), PCA parameters from only reflectance data (dashed red line), and PCA parameters from only fluorescence data (dashed green line). The ROC curves were generated by applying a threshold to the optical diagnosis probability of adenocarcinoma. The area under the ROC curve was 0.89 for combined reflectance and fluorescence parameters, 0.89 for only reflectance parameters, and 0.86 for only fluorescence parameters.

These results show that optical spectroscopy accurately classify pancreatic disease from normal tissues. Interestingly, for distinguishing between the tissue types measured in this study, using reflectance alone performed as well as diagnostic accuracy of the reflectance and fluorescence parameters (Table 3.1). This is a significant finding, as an optical device that used only reflectance would be less expensive, more compact, and faster when performing measurements.

Table 3.1 Sensitivity, specificity, positive predictive value, negative predictive value, and area under the receiver operating characteristic curve of optical spectroscopy for distinguishing between pancreatic adenocarcinoma (A), chronic pancreatitis (CP), and normal pancreatic tissue (N).

Method	Classification	Sensitivity	Specificity	Positive Predictive Value	Negative Predictive Value	Area Under Curve
Reflectance &Fluorescence	A vs. (CP and N)	**91%**	**82%**	69%	95%	**0.89**
	(A and CP) vs. N	83%	87%	92%	76%	0.90
	A vs. N	97%	90%	89%	97%	0.96
	A vs. CP	91%	71%	74%	89%	0.81
	CP vs. N	77%	82%	79%	80%	0.84
Reflectance	A vs. (CP and N)	**91%**	**84%**	71%	95%	**0.89**
	(A and CP) vs. N	82%	87%	92%	74%	0.89
	A vs. N	94%	95%	94%	95%	0.97
	A vs. CP	91%	68%	73%	89%	0.81
	CP vs. N	71%	87%	83%	77%	0.83
Fluorescence	A vs. (CP and N)	**91%**	**78%**	65%	95%	**0.86**
	(A and CP) vs. N	76%	87%	91%	68%	0.81
	A vs. N	94%	90%	88%	94%	0.91
	A vs. CP	81%	77%	77%	81%	0.78
	CP vs. N	68%	85%	79%	75%	0.73

3.3.2 Scattering Analysis and Classification Results

Figure 3.7 (A) shows representative reflectance spectra from 630 to 760 nm, measured on three sites of each tissue type. Each of 9 spectra comes from all different patients. At a glance, it is observed that the reflectance from adenocarcinoma sites is lower than those from normal and pancreatitis sites. Goodness of fit in Fig. 3.7 (A) suggests the employed rapid and simple scattering model well describes wavelength-resolved reflectance above 630 nm. Given a linear relationship between the reflectance and the reduced scattering coefficients, mean wavelength- resolved reduced scattering coefficient for normal sites is higher than pancreatitis and adenocarcinoma (Fig. 3.7 (B)). Range (4 ~ 20 cm^{-1}) of the extracted reduced scattering coefficient is consistent with typical human tissues [76]. Reduced scattering coefficients at several discrete wavelengths for each tissue type were listed in Table 3.2.

Table 3.2 Scattering Power and Reduced Scattering Coefficients (mean ± SE)

	SP	$\mu'_s(630\,nm)$ cm^{-1}	$\mu'_s(700\,nm)$ cm^{-1}	$\mu'_s(750\,nm)$ cm^{-1}
Normal (39 sites)	0.21 ± 0.01	15.96 ± 0.36	15.61 ± 0.35	15.38 ± 0.35
Chronic Pancreatitis (34 sites)	0.51 ± 0.06	12.66 ± 0.42	12.02 ± 0.43	11.63 ± 0.43
Adenocarcinoma (32 sites)	0.77 ± 0.06	10.53 ± 0.43	9.70 ± 0.40	9.19 ± 0.38

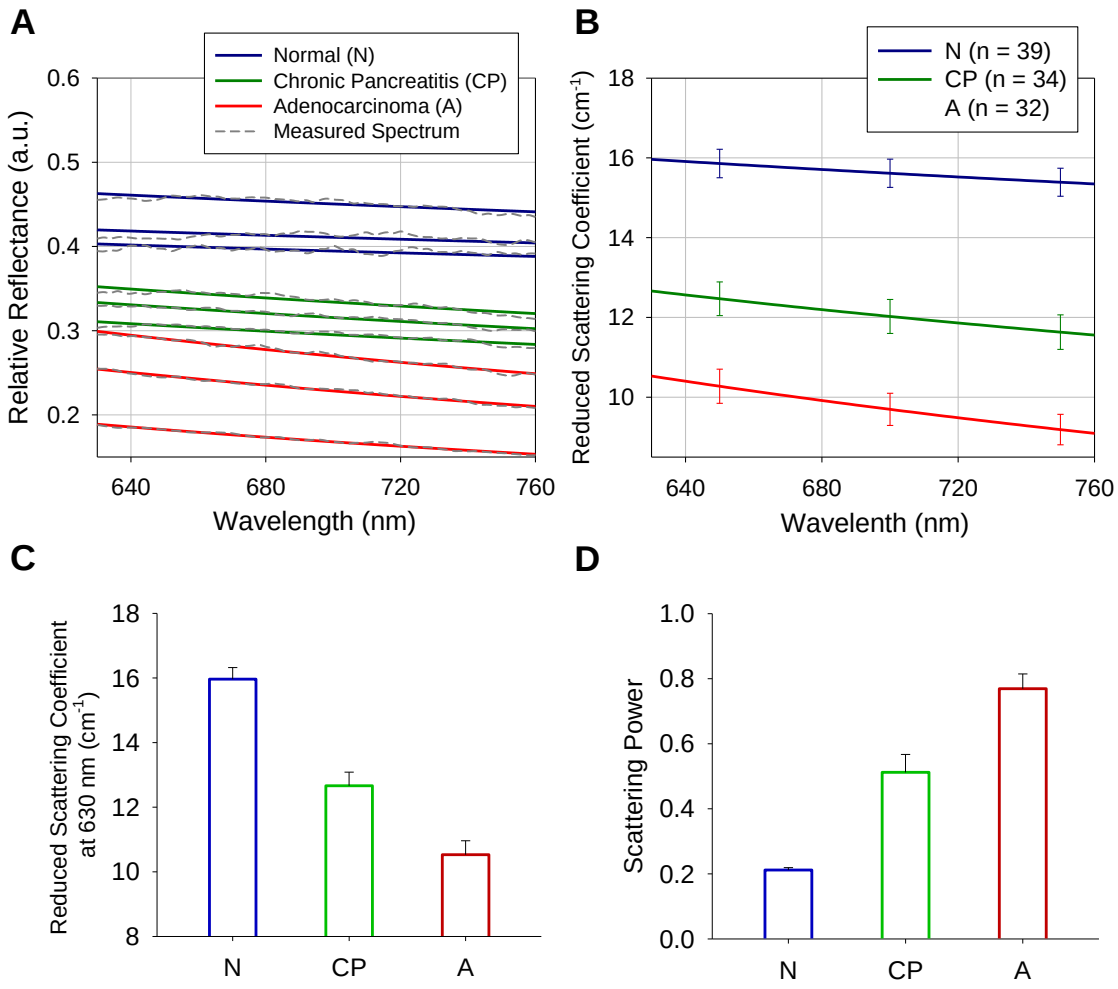

Figure 3.7 Representative measured reflectance spectra (gray-dashed lines) and their fits (colored-solid lines) from different types of pancreatic tissues including normal (blue), chronic pancreatitis (green) and adenocarcinoma (red). Reflectance intensity and slop show a distinct difference between three pancreatic tissue types (B) Mean of estimated wavelength-dependent reduced scattering coefficients for three pancreatic tissue types (39 sites for normal, 34 sites for chronic pancreatitis and 32 sites for adenocarcinoma). (C) Extracted reduced scattering coefficients at 630 nm for three pancreatic tissue types. The reduced scattering coefficients at 630 nm are significantly different for all comparisons (N vs. CP, N vs. A, and CP vs. A) with $p < 0.001$. (D) Extracted scattering power from three tissue types. The scattering powers are also significantly different for all comparison with $p < 0.001$. Error bars in (B),(C) and (D) represent the standard error**.**

Figure 3.7 (C) and (D) display bar plots of the estimated μ'_s(630 nm) and scattering power γ of three tissue types. Compared to normal and pancreatitis sites, μ'_s(630 nm) of adenocarcinoma is significantly lower ($p < 0.001$). In contrast, scattering power of

adenocarcinoma is significantly higher than normal and pancreatitis tissues ($P < 0.001$). It is noted that scattering powers of almost all normal sites converges to 0.2, which is the experimental minimum value [81]. According to Mie theory [79, 88], large scatterer (> 1 μm) such as nuclei are likely to be the major scattering source in normal pancreatic tissues.

Using tissue classification algorithm, two scattering parameters, $\mu'_s(630)$ and scattering power γ distinguish adenocarcinoma from benign tissues with the sensitivity of 94% and specificity of 75%. The result suggests that pancreatic tissue scattering property is diagnostically useful for separating adenocarcinoma in the setting of pancreatitis. Sensitivity and specificity for other classifications are listed in Table 3.3. ROC analysis also demonstrates the diagnostic ability of tissue scattering parameters in discriminating each pancreatic tissue type, as shown in Figure 3.8. The area under the curve (AUC) is 0.89 and 0.97 for distinguishing malignancy from benign and adenocarcinoma from normal, respectively.

Table 3.3 Sensitivity and Specificity for different classification (Confidence Interval with $\alpha = 0.05$)

	Sensitivity	Specificity
Malignant (A) vs. Benign (CP & N)	94 (78 – 99) %	75 (64 – 84) %
All Pathology (A & CP) vs. N	88 (77 – 94) %	90 (75 – 97) %
A vs. N	94 (78 – 99) %	95 (81 – 99) %
A vs. CP	81 (63 – 92) %	71 (52 – 84) %
CP vs. N	88 (72 – 96) %	80 (63 – 90) %

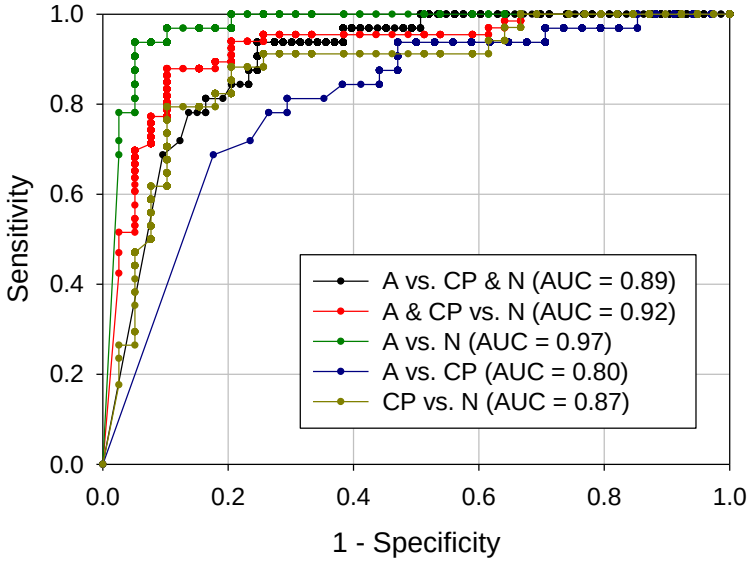

Figure 3.8 The receiver operating curves (ROCs) for different classifications with the area under curve (AUC).

3.4 Discussion

In this pilot study, the clinically-compatible reflectance spectroscopy and the rapid scattering model were employed to investigate the diagnostic potential of pancreatic tissue scattering properties in freshly excised pancreas.

Reflectance Only Dataset In this study, tissue classification employing only reflectance provided nearly identical results to those obtained with a combination of reflectance and fluorescence. This finding can possibly be attributed to an overlap between the information encoded in the reflectance and fluorescence principal components. The reflectance data is known to contain notable information about tissue scattering, which is partially due to collagen in the tissue. However, collagen is also a prominent endogenous fluorophore in human pancreatic tissue, so the information about collagen is also found in

the fluorescence spectra. Therefore, it is to be expected that the reflectance and fluorescence principal components would include overlapping information.

In Figure 3.3 (B), the first fluorescence principal component contains a spectral feature near the peak emission wavelength (~400 nm) of collagen fluorescence, which was previously shown to distinguish between these tissue types in our previous work [68] . Fig. 3.3 (A) shows that the second and third reflectance principal components display spectral features similar to those of hemoglobin absorption, which has a distinctive Soret peak near 420 nm and secondary peaks near 545 nm and 575 nm. Since absorption (from hemoglobin) and scattering (from tissue components including collagen) play prominent roles in determining the measured reflectance spectrum, we can reasonably attribute that the first reflectance principal component to primarily collagen scattering and the second and third reflectance principal components could to hemoglobin absorption. Since the fluorescence spectrum also contains prominent information about collagen, as well as artifacts of hemoglobin absorption, it is quite possible that the fluorescence data is not providing a significant amount of diagnostic information that is different from that provided by the reflectance.

Discussion on scattering In our study, the wavelength-resolved reduced scattering coefficient and scattering power of human pancreatic tissue have been estimated based on calibration using a set of synthetic tissue-simulating phantoms. Although tissue scattering signal reveals tissue morphology or micro-architecture, detailed mechanism on how intracellular components (such as nuclei, mitochondria and membrane) and extracellular matrix (collagen) contribute to the entire scattering is very complex and is not well understood. In previous work [78, 79] attempting to explain power law dependence with

Mie theory, it was found that the scattering power is related to average scatterer size. Our study shows that the scattering power for adenocarcinoma and chronic pancreatitis is larger than that of normal tissues, suggesting an increased contribution of small-size scatterer. According to Mie theory, scattering power does not significantly change below 0.37 if scatterer size is larger than a certain size (~1 μm), implying that relatively large intracellular components such as nuclei (a typical size of normal nuclei is known to be around 9 μm) and mitochondria could be major scatterers in normal pancreatic tissues. Since collagen content is reported to increase in adenocarcinoma and pancreatitis due to stromal fibrosis, the increase of scattering power is possibly attributed to an increase of collagen content. In contrast, the scattering amplitude of adenocarcinoma decreases from normal to pancreatitis, which is an opposite trend to some of the other tissue types.

Study Limitations A key limitation of this work is a small number of patients due to difficulties in frequent attendance to a suitable surgical case. Thus, our study needs to be considered a pilot study that assesses potential of reflectance spectroscopy for real-time pancreatic cancer detection. One potential problem that occurs in a statistical analysis evaluating multiple sites measured from a single patient (*i.e.* intra-patient correlation) is addressed by employing GEE method in tissue classification algorithm. GEE has been previously developed to account for the intra-patient correlation in medical physics studies, including ophthalmologic studies that investigate two eyes in a single patient [89].

Another limitation is that the study is restricted to *ex vivo* measurements from freshly-excised surgical specimen. Given the study focuses only on tissue scattering properties, it is unlikely that scattering properties significantly change within 30 minutes after

excision. The analyzed wavelength range (630 to 760nm) is also independent from blood absorption that could significantly alter either by a drain of internal blood after excision or remaining hemorrhage even after clean up when site is cut for optical interrogation. A preliminary study demonstrating technical feasibility of *in vivo* optical measurement on pancreas showed that *ex vivo* and *in vivo* reflectance spectrum acquired from the same site were almost identical with a minor discrepancy in the main blood absorption wavelength (420 and 550 nm). The advantage of *ex vivo* study is to obtain the gold-standard histopathology, which is impossible via a current standard diagnostic procedure for pancreatic cancer, unlike other type of cancers where core biopsy is available on intact tissues. The gold-standard histology is essential to establish an accurate tissue classification algorithm and is expected to play an important role to expand this technique to a future *in vivo* studies employing endoscopic-compatible fiber optic probe.

3.5 Conclusion

This pilot study revealed that pancreatic tissue scattering properties estimated by reflectance spectroscopy coupled with a simple scattering model, had a diagnostic power to distinguish malignant tissues from non-malignant tissues. Reflectance spectroscopy is suitable for clinical translations because of its rapid acquisition and processing time, and compactness and cost-effectiveness of the device.

Chapter 4.
Ray-traced Monte Carlo Simulation for Fluorescence Measurements in Turbid Media

4.1 Introduction

Fluorescence spectroscopy and imaging have become invaluable tools in biology and biomedicine fields due to their ability to differentiate cells and sub-cellular components which emit fluorescence with a high specificity from a background with no fluorescence [90]. In both fluorescence spectroscopy and imaging system, sample scattering is always a technical issue to address for an accurate analysis of the sample fluorescence. For spectroscopy, intrinsic fluorescence signal or spectrum needs to be recovered from the measured fluorescence that detects the re-emitted fluorescence undergoing absorption and scattering in turbid media. In the imaging system, scattering is the main source of a signal distortion and determination of penetration depth.

As a quantitative method, Monte Carlo (MC) simulation has been employed to evaluate the performance and design the optics in the optical spectroscopic or imaging systems probing turbid biological tissues. Reflectance confocal imaging techniques in turbid media have been assessed using an embedded Monte Carlo function in the commercialized ray-tracing software (ASAP) [91, 92]. Fluorescence collection efficiency in multiphoton microscopy has also been investigated [93], but only fluorescence emission has been modeled. Probably, due to the incomplete implementation and limitations of Monte Carlo function in the software for fluorescence occurrence and propagations, there have not been any previous studies that report the full fluorescence path modeling in turbid media with fluorescence imaging system.

For fluorescence spectroscopic system, Monte Carlo (MC) simulation code [16, 94] has been developed to accurately model fluorescence photon propagation in biological tissues. The code has been extensively employed to design the depth-sensitive fiber-optic probes using different source-detection separations [95], angled fiber [96], ball lens [97], or combined beveled fiber with a ball lens [98]. However, MC simulation code has a limitation in incorporating complex mathematical equations for ray-tracing through the specialized lenses such as graded-index (GRIN) lens and aspherical lens, or compound lenses and series of different lenses.

Thus, the idea of combining ray-tracing software and MC codes could be an effective and useful way to address technical needs in simulation methods for both spectroscopic and imaging applications. In this paper, we introduce a ray-traced MC (RTMC) simulation method to combine ZEMAX® ray tracing software and MC simulation code to model a complete path of fluorescence excitation, propagation and detection on turbid media by optical spectroscopy or imaging system. We verified the RTMC simulations both computationally and experimentally.

4.2 Basic Concept of RTMC Simulation

The RTMC simulation works in a complementary way such that ZEMAX® traces rays through the optical system including a source, lenses, and detector, and MC simulation models photon propagation inside the turbid media. (Fig. 4.1) In detail, the non-sequential mode of ZEMAX® launches a maximum of 10^6 rays from a virtual source for the excitation path tracing. The launched rays pass through the optical components and contact a virtual detector that locates at the surface of targeted samples. When each ray meets the detector, ZEMAX® ray tracing mode exports the array file that contains the geometrical information of the incident rays, including incident positions (x,y and z coordinates), angle ($\cos\alpha$, $\cos\beta$ and $\cos\gamma$) and intensity.

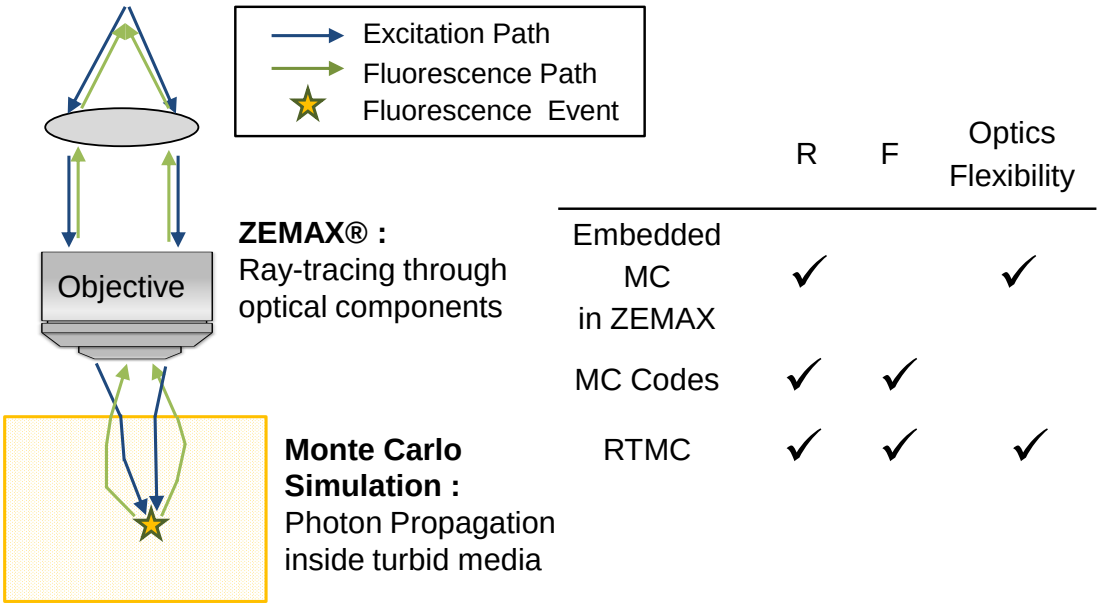

Figure 4.1 Basic concept of the RTMC simulation. ZEMAX® performs ray tracing through optical components from source to media, and from media to detector. Once the ray enters the media, Monte Carlo code simulates fluorescence occurrence and propagation. While the embedded Monte Carlo function in ZEMAX® is able to model diffuse reflectance including scattering and absorption, it has limitations to simulate fluorescence propagation. In the MC code, complex ray tracing equations have to be built manually, which restricts employing a variety of optical components. RTMC method combines these two methods in a complimentary way to enable complete fluorescence ray tracking through optics and turbid samples.

Exported array file from ZEMAX® is imported as the initial photon distribution for MC simulation that is modified from the original code [99]. During simulating fluorescence occurrence and propagation inside turbid media, the geometrical and spectral information of the photons exiting the surface is saved in compatible file format with ZEMAX® source object. Second ZEMAX® ray tracing mode employs this array file as a source object to trace the emitted fluorescence signal from the sample surface to the detector via optical components. Detector in ZEMAX® can display both 2-D graphical distribution of detected ray and the spectroscopic data.

4.3 Computational Verification

To prove the accuracy of interfacing ZEMAX® and MC code via the ray data array file, RTMC simulation was computationally verified with reflectance and fluorescence measurements simulations. The simulations were performed on optical tissue models using two flat-ended optical fibers for light delivery. Simulated reflectance and fluorescence with RTMC simulations were compared with those simulated by the previously developed MC code in MATLAB[100]. Epithelial colon tissue models were employed as two-layered optical model, which consists of a mucosa layer with finite thickness atop a semi-infinite submucosal layer (Table 4.1) Optical transport properties (scattering coefficient, absorption coefficient and anisotropy) at fluorescence excitation and emission wavelength, and fluorophore properties (absorption coefficient and quantum yield) were employed from the previous study [101]. Three different types of models depending on disease status were employed. Tissue 1 was normal colon, tissue 2 was adenomatous tissue having different optical transport properties in mucosal layer, and tissue 3 was also adenomatous model with the same optical properties with tissue 2, but with thicker submucosal layer [101].

Table 4.1 Optical Properties of the Three Epithelial Tissue Models

Wavelength, λ (nm)		Layer 1 (n_1 = 1.35 g_1 = 0.9)				Layer 2 (n_2 = 1.38 g_2 = 0.95)		
		μ_a (cm^{-1})	μ_s (cm^{-1})	μ_{af} (cm^{-1})	z (μm)	μ_a (cm^{-1})	μ_s (cm^{-1})	μ_{af} (cm^{-1})
Tissue 1 (Normal)	355 (Excitation)	12	200	0.5	500	12	200	1.5
	550 (Emission)	3	90			3	9	
Tissue 2 (Adenoma)	355 (Excitation)	20	120	0.5	500	12	200	1.0
	550 (Emission)	10	70			3	90	
Tissue 3 (Adenoma)	355 (Excitation)	20	120	0.5	700	12	200	1.0
	550 (Emission)	10	70			3	90	

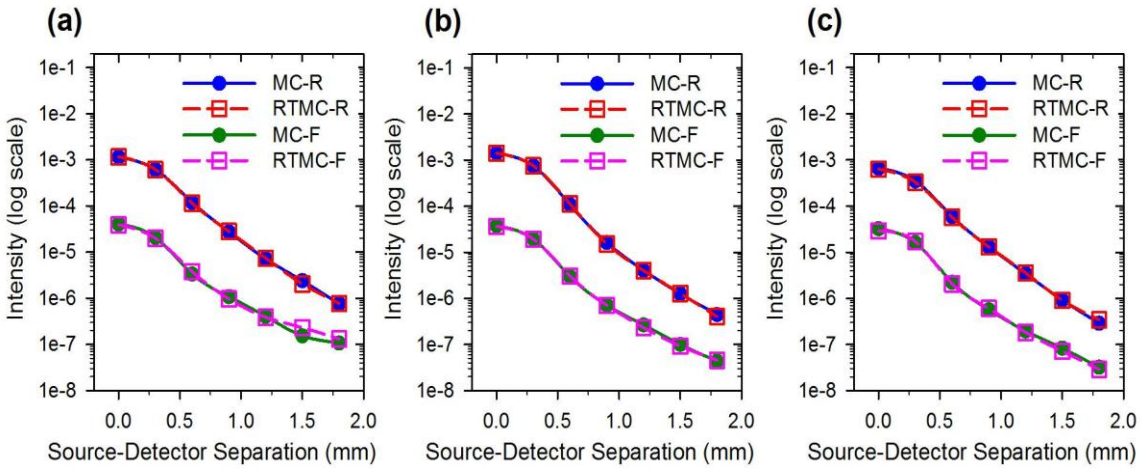

Figure 4.2 Comparison of MC and RTMC simulation results for reflectance and fluorescence measurements using fiber-optic probe on epithelial tissue model 1 (a), model 2 (b) and model 3 (c) at different source-detector separations.

Excitation light from a source was delivered to the tissue samples via an optical fiber with the core diameter of 600 µm and 0.22 NA. The identical fiber delivered the emitted reflectance and fluorescence from the sample. Source-detection separations (ρ) were 0, 300, 600, 900, 1200, 1500 and 1800 µm. In the RTMC simulation, optical fibers were created using two concentric cylinder volume objects with inner and outer radius of 300 and 310 µm respectively from the ZEMAX® library. Refractive indices of inner and outer cylinders were set as 1.450 and 1.433 respectively to create a total internal reflection with 0.22 NA. A total of 1×10^6 photons were launched from the source for each simulation method.

Figure 4.2 shows the comparison of MC and RTMC simulation on three different tissue computational models. Average percent errors between two methods for all the source and detection separations and tissue types are 3.5% and 7.1% for reflectance and fluorescence, respectively. It is noted that accuracy was consistent over a wide range of

detected photon intensities with an order of 10^4, indicating the interface between ZEMAX® and MC code using a geometrical photon array file works as expected.

4.4 Experimental Verification

Experimental verification of the RT-MC simulation was performed on depth-sensitive fluorescence measurement of two-layered optical phantoms as shown in Fig. 4.3. The depth-sensitive optical setup was designed by employing an aspherical lens with high NA as an objective lens, which has not been employed in any previous MC simulation studies, to the best of our knowledge.

4.4.1 Depth-Sensitive Fluorescence Spectroscopy

The depth-sensitive fluorescence measurement system utilized a 355 nm pulsed laser (PNV001525-140, JDS Uniphase, San Jose, CA) for excitation (Fig. 4.3). Laser light emitted from the multi-mode fiber (core diameter = 100 µm) was collimated by a plano-convex lens (LA4936-UV, Thorlabs, Newton, NJ). This collimated beam was reflected by a dichroic mirror (FF365-Di01, Semrock, Rochester, NY) and then focused by an aspherical lens (49-587, Edmund Optics, Barrington, NJ) with NA = 0.5 and working distance of 15 mm. Emitted fluorescence signal from the phantoms was collected by the same aspherical lens, passed through the dichroic mirror and a long pass filter (LP02-355RS, Semrock), and then focused into a detection multi-mode detection fiber with 0.22 of NA and 600 µm of core diameter by another plano-convex lens (LA1131-A, Thorlabs). The collected fluorescence signal was transmitted to a spectrograph (MS 125, Oriel Instruments, Stratford, CT) coupled ICCD (ICCD 2063, Andor Technology, Belfast, UK) for spectra acquisition with 1 nm resolution. All the employed lenses and

fibers were modeled in the ZEMAX® non-sequential mode with the downloaded components provided from the manufacturer's website.

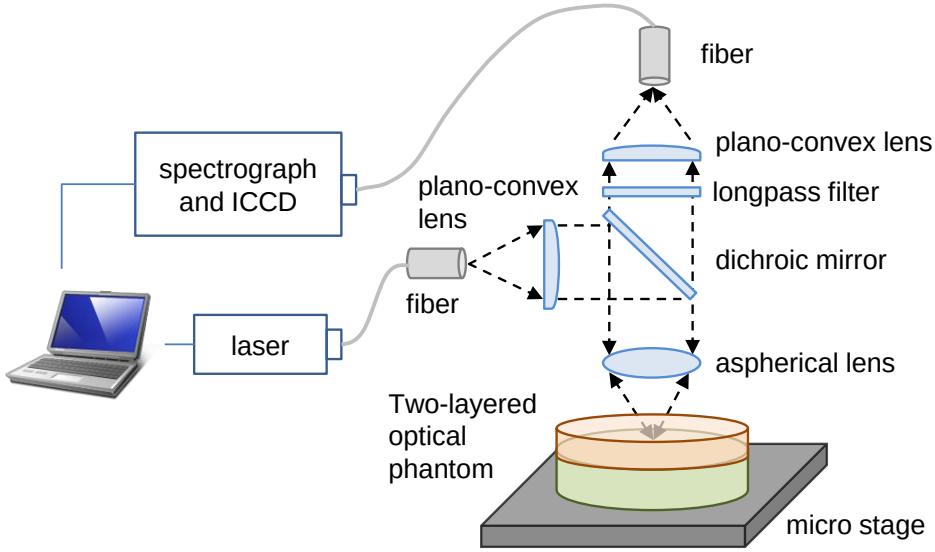

Figure 4.3 Schematic of experimental depth-sensitive fluorescence spectroscopy system setup for tissue-simulating phantom verification

4.4.2 Two-layered Fluorescence Phantom Fabrication and Characterization

Two-layered fluorescence phantoms were constructed with a solid agarose-based top layer and a solid polydimethylsiloxane (PDMS)-based bottom layer. Hydrophobic property of PDMS prevented diffusion of fluorophore from the hydrophilic top layer, eliminating a need of any sheet between two layers, which could have unknown optical effects. Thicknesses of top and bottom layers were 1 mm and 10 mm, respectively. The lateral size of both layers was 60 mm in diameter to ensure a semi-infinite medium. Standard fluorophores, Rhodamine 6G (R4127, Sigma Aldrich, St. Louis, MO) and POPOP (P3754, Sigma Aldrich) were added to the top and bottom layers respectively for spectral separation in measured spectra. An agarose powder (161-3101, Bio-Rad Laboratories, Hercules, CA) was mixed in boiled DI (de-ionized) water with 2%

concentration, and thoroughly dissolved to obtain a homogeneous solution. When the mixture was cooled to 60~70 ˚C, pre-calculated volume of Intralipid (I141, Sigma Aldrich) was added to mimic the scattering coefficients of biological tissues. 1mM of Rhodamine 6G solution in DI water was added to the mixture to be diluted to 0.5 μM. When the temperature of the mixture reached 40 ˚C, a pre-calculated volume of the mixture was transferred into a petri dish to create a top layer of specified thicknesses (1 mm) and then cured for 1 hour in a cool, dark enclosure.

The PDMS-based bottom layer was fabricated according to a previously described recipe [102]. Briefly, a specific weight of titanium oxide (TiO_2) powder (Ti-602, Atlantic Equipment Engineers, Upper Saddle River, NJ) was added as scatterers in PDMS curing agent to mimic biological tissue scattering. To dissolve TiO_2 completely, the mixture was placed in an ultrasonic bath for 20 minute and stirred manually every 5 minutes. Then, the mixture and PDMS (Sylgard 184, Dow Corning, Midland, MI) were mixed with 1:10 ratio. A pre-calculated volume of 1 mM POPOP solution in cyclohaxane was added to this mixture to create 10 μM concentrations. The mixture was transferred to a petri dish, placed in a vacuum chamber for the de-gassing process for 30 minutes, and cured for 24 hours at room temperature.

The absorption coefficients (μ_a) and scattering coefficients (μ_s) of all fabricated layers were determined by the integrating sphere (RT-060-SF, Labsphere, North Sutton, NH) measurements and estimation using an inverse adding-doubling (IAD) algorithm. Detailed setup and procedure has been described previously [82]. The fluorescence absorption coefficients were calculated from the transmission measurement of the spectrophotometer (DU800, Beckman Coulter, Fullerton, CA) using a 1cm path-length

cuvette. Input parameters for optical properties of the manufactured phantoms are shown in Table 4.2. Refractive indices were set to 1.33 and 1.4 for the top and bottom layers respectively, and anisotropy was set to 0.9 in both layers. Two different phantoms were additionally manufactured and measured to add variations in the experimental verification. In the second phantom, Intralipid concentration was three times higher than the first phantom with other properties being the same. The third phantom had only variation of a 0.5 mm-thick top layer compared to the first phantom.

Table 4.2 Optical Properties and Thickness of the Top and Bottom layer for Two-layered Phantoms (μ_s: scattering coefficient, μ_{afx}: fluorescence absorption coefficient, z = thickness)

Wave-length (nm)	Top			Bottom		
	μ_s (cm^{-1})	μ_{afx} (cm^{-1})	z (mm)	μ_s (cm^{-1})	μ_{afx} (cm^{-1})	z (mm)
355	115 ± 5			29 ± 3		
418	100 ± 5		1	26 ± 3	0.46	10
560	76 ± 4	0.016		24 ± 2		

4.4.3 Depth-Sensitive Fluorescence Measurements

For depth-sensitive fluorescence measurements, a focal point was scanned in z-direction from the surface to 1 mm deep, in step sizes of 250 μm, using a micro linear actuator (LTA-HS, Newport, Irvine, CA). Excitation laser intensity was set to make sure of no photo-bleaching. Acquisition time per one depth was around 2 seconds. Recorded fluorescence spectra were background subtracted and corrected with ICCD spectral response [75]. Figure 4.4 displays fluorescence emission spectra at different focal depth, showing a distinct separation of peak emission wavelength between POPOP (420 nm) and Rhodamine 6G (550 nm). As the focal point goes deeper, fluorescence emission

intensity of Rhodamine 6G increases with a corresponding decrease in POPOP intensity. Top layer sensitivity was defined as Rhodamine 6G emission intensity (that is the integrated intensity from 520 to 630 nm) divided by the sum of Rhodamine 6G and POPOP emission intensity (from 360 to 480 nm).

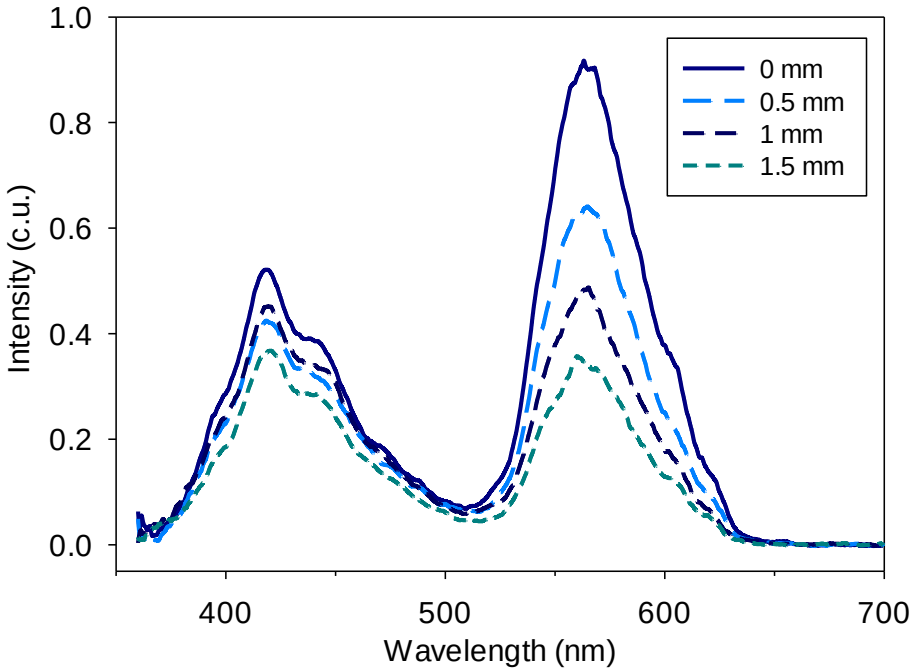

Figure 4.4 Fluorescence emission spectra variation of two-layered optical phantom at different focal depths. As the focal point goes deeper, a relative intensity of the top layer (Rhodamine 6G, 560 nm peak emission) decreases while the one of the bottom layer increases (POPOP, 420 nm peak emission)

4.4.4 Comparison between simulation and the actual measurement

Figure 4.5 shows the top layer sensitivity at each focal depth estimated from RTMC simulations and calculated from the actual measurements for three different phantoms. For all phantoms, top layer sensitivity reduces as the focal point goes deeper and closer to the bottom layer. Overall, the RTMC simulation predictions and the experimental measurements are well agreed in terms of a decreasing trend over the scanning depth

range and the absolute values of top layer sensitivity in all three different phantoms. Mean percent error for all depth points is less than 15%. In particular, RTMC simulation estimates the top layer sensitivity at the surface accurately.

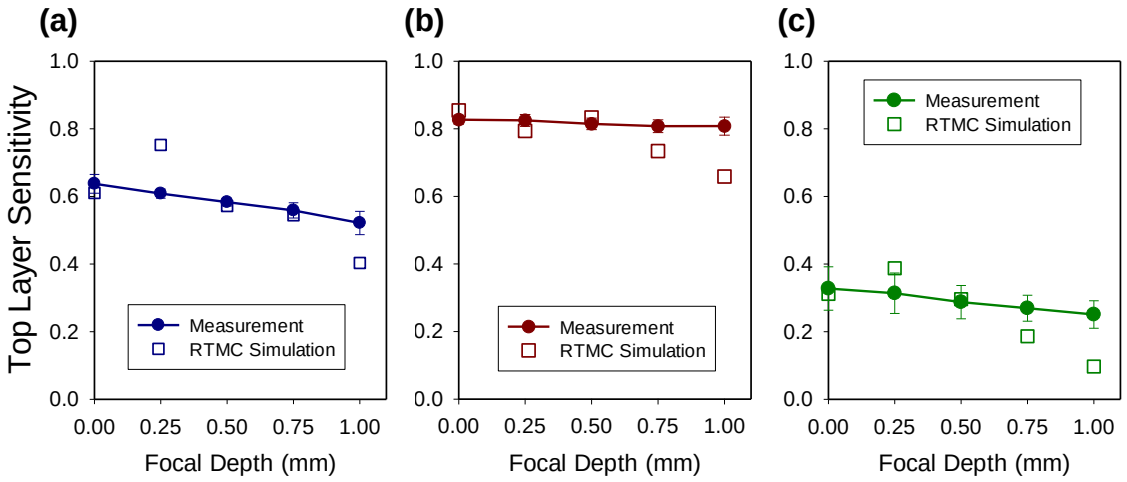

Figure 4.5 Experimental verification results on three manufactured two-layered phantoms (a) phantom 1 (b) phantom 2 and (c) phantom 3. Top layer sensitivity is compared between measurements and simulations by 0.25 mm step size of focal point until 1.00 mm. Solid lines with solid circles indicate actual measurements and empty rectangles indicates RTMC simulation results. In the measurements, error bars present the standard deviations

The simulation and experiments well predicts an understandable variation of the top layer sensitivity in three phantoms as intended in phantom design. The top layer sensitivity of the second phantom is higher than the first phantom due to higher scattering coefficients of the top layer causing more fluorescence photons to scatter, which increases a chance of detection. The lower top layer sensitivity of the third phantom is attributed to a thin top layer with less amount of Rhodamine 6G fluorophore amount and more interference of POPOP fluorescence from the bottom layer.

Difference between the simulations and experiments is observed at deeper focal points (between 0.75 and 1 mm) in all three phantoms. This could be attributed to either

experimental or computational errors. The decreasing slope of the top layer sensitivity is relevant to the overall depth sensitivity of the device. The gradual slope in the experimental results compared to the one from the simulations would indicate the imperfection of optics alignment in the instrument set up. In the RTMC model, the fixed values of anisotropy, which is likely to be wavelength-dependent, also could cause some incomplete tracking of photon propagations.

In spite of these small errors, the good agreement between the RTMC simulations and experiments verifies that RTMC simulation is a computational tool to provide an accurate estimation of fluorescence excitation and detection by optical spectroscopy system, as well as a transport inside by-layered turbid media model.

4.5 Conclusion

In this chapter, RTMC simulation method was proposed and developed with an aim to fill a technical gap of current computational tools by providing an accurate modeling of a complete path of fluorescence excitation, detection and propagation through optical system and turbid media. Applications of RTMC are not limited to employing a traditional optical component such as lens and filter. Due to flexibility and ongoing-update of a huge ZEMAX library, the RTMC has a potential to computationally model an optical fluorescence sensing in turbid media by optoelectronic devices such as light-emitting diode, laser diode and photodiode, which have not been employed in the previous simulation works.

Chapter 5.
Prototype Design of Optoelectronic Microprobe

5.1 Introduction

5.1.1 Motivation

Optical diagnostics have made considerable advancements in recent years as a method to provide non-invasive, quantitative, and rapid sample/tissue analysis in a clinical setting. In cell biology alone, numerous advancements have been enabled through the development of fluorescence-based analysis methods. Furthermore, biomedical studies (including studies involving cancer and other diseases) have been transformed through commercial technology for whole body animal imaging (*e.g.*, Caliper Life Sciences IVIS imaging system). In more clinical settings, optical FDA approved technologies are routinely employed (such as the pulse oximeter, Philips BiliChek bilirubinometer, the DentalEZ Identafi oral cancer screening system, and MELA Sciences MelaFind system for early melanoma detection).

For many clinical applications, including those discussed above, optical technologies are not subject to a confined space because the studied tissue is readily accessible from outside the body (*i.e.*, oral cavity or skin). Therefore, developed technologies are typically large footprint instruments, including robust and expansive spectroscopy/imaging systems that access human tissue via remote fiber-optic probes. Reports in recent literature describe numerous technologies developed with fiber-optic probes [97, 103-107], employed because they are easy-to-use, reliable, and enable remote sample sensing (*i.e.*, away from equipment). Critical limitations to such approaches

include the relative rigidity of fiber-optic probes (inability to undergo tight bends) and inability of fiber-optic probes to enable volumetric mapping within a confined space.

Here, we consider the clinical application of needle-based clinical methodologies, including for tissue diagnostics and drug/treatment delivery. Needle-based methodologies have numerous applications, including fine-needle aspiration for cancer detection (employed for breast [104, 108], lung [36, 109, 110], prostate [111, 112], and pancreatic cancers [22, 55-57] diagnosis) as well as for nerve block treatments (researched by Philips) [113-115]. There are two common approaches for needle-based analysis of tissues: imaging and spectroscopy. Imaging through a hollow needle has been demonstrated with the development of the needle-based confocal imaging system Cellvizio [50, 116, 117], commercialized by Mauna Kea. Limitations to imaging based systems include their small field-of-view and complicated/time expensive requirement for real-time quantitative image analysis. Such applications employing fiber-optic probes are limited by their rigidity, lack of volumetric mapping, and/or constrained center-to-center spacing between source and detectors.

We proposed to develop an optoelectronic microprobe, constrained within a hollow needle (including common 19, 22, and 25 gauge needles), for quantitative volumetric optical mapping within tissues. Primary advantages, compared to fiber-optic based technologies, include the robustness of miniature microelectromechanical systems (precisely manufactured to dimensions < 1 mm) and their compactness (provide ability to withstand tight bending radii). Furthermore, optical modules were designed to preserve center-to-center spacing (utilizing long axis of the needle) of optical sources and detectors typical of fiber-optic probe-based measurements [55], critical for accurate tissue

diagnostics by increasing the tissue volume studied. Additionally, the optoelectronic microprobes can be manufactured with numerous probe geometries to enable volumetric mapping that is impossible with current fiber-based approaches.

5.1.2 Scientific Background

EUS-compatible optoelectronic sensing technology provides additional diagnostic information to supplement cytology based diagnosis and overcome its limitations, either by providing independent diagnosis of the pancreatic abnormality or by guiding the endoscopist performing EUS to select the most likely areas to obtain diagnostically relevant cytological material.

Preliminary studies in the human pancreas including works in the chapter 3, have shown that optical sensing can provide a new source of contrast for the detection of pancreatic cancer (Fig. 5.1) [22, 55-57]. The interaction of light with tissue can be measured and analyzed to obtain diagnostic information *in vivo* [7, 66, 90, 94, 101]. In the pancreas, histopathological analysis shows enlarged cell nuclei and abundant collagen in adenocarcinoma, which can be accurately detected by tissue optical sensing, thereby providing an opportunity to improve pancreatic neoplasia diagnosis [22, 55-57].

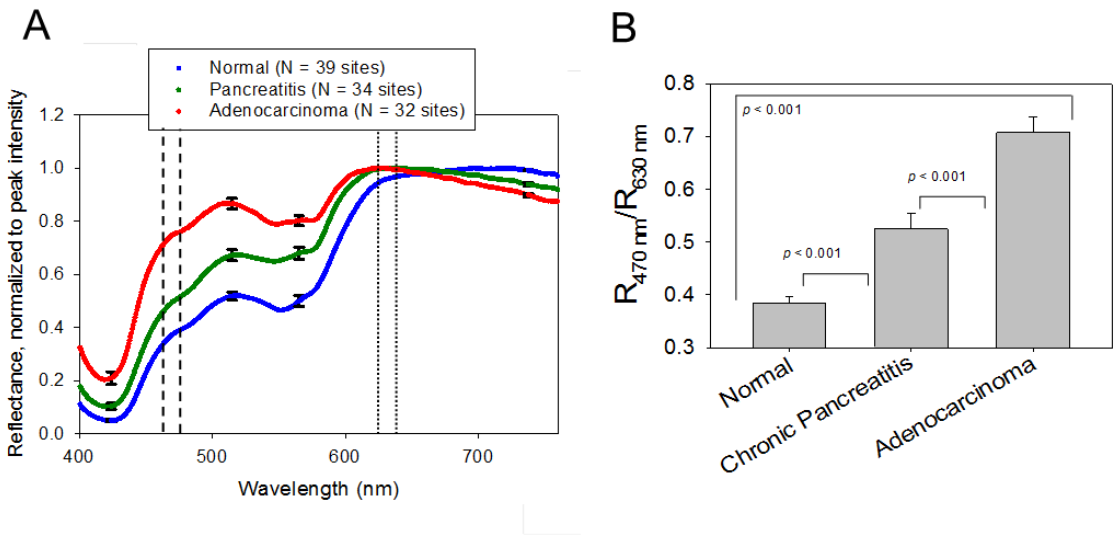

Figure 5.1 Results are presented from a clinical pilot study from freshly-excised pancreatic tissues from 18 patients. (A) Averaged reflectance spectra revealed significant differences between normal, chronic pancreatitis, and pancreatic adenocarcinoma. (Normalized spectra of Figure 3.1 in the chapter 3). Dotted vertical lines identify two wavelength bands (centered at 470 and 630 nm) proposed for the optoelectronic microprobe. (B) The ratio of summed intensities within each wavelength band accurately distinguished among the three most prevalent pancreatic tissues. All error bars represent standard error.

5.1.3 Basic Concept

Based on the strong preliminary results, we believe optical diagnostics will enhance the technical capability of the endoscopist to provide a more accurate diagnosis and dramatically alter clinical practice by improved triage of patients to appropriate therapy (surgery or not). In addition to the enhanced accuracy of diagnosis, the technology outlined here (see microprobe technology compatible with commercially-available FNA needles in Figure 5. 2) will provide volumetrically mapped tissue assessment by rapidly measuring multiple tissue sites, unlike EUS-FNA, which requires multiple needle passes into tissue for a single aspirate collection. Thus, the proposed approach has the potential to address the important unmet need of pancreatic neoplasia diagnosis (low negative

predictive value of cytology) by improving the diagnostic capability of EUS, thereby leading to improved triage of patients to appropriate therapy.

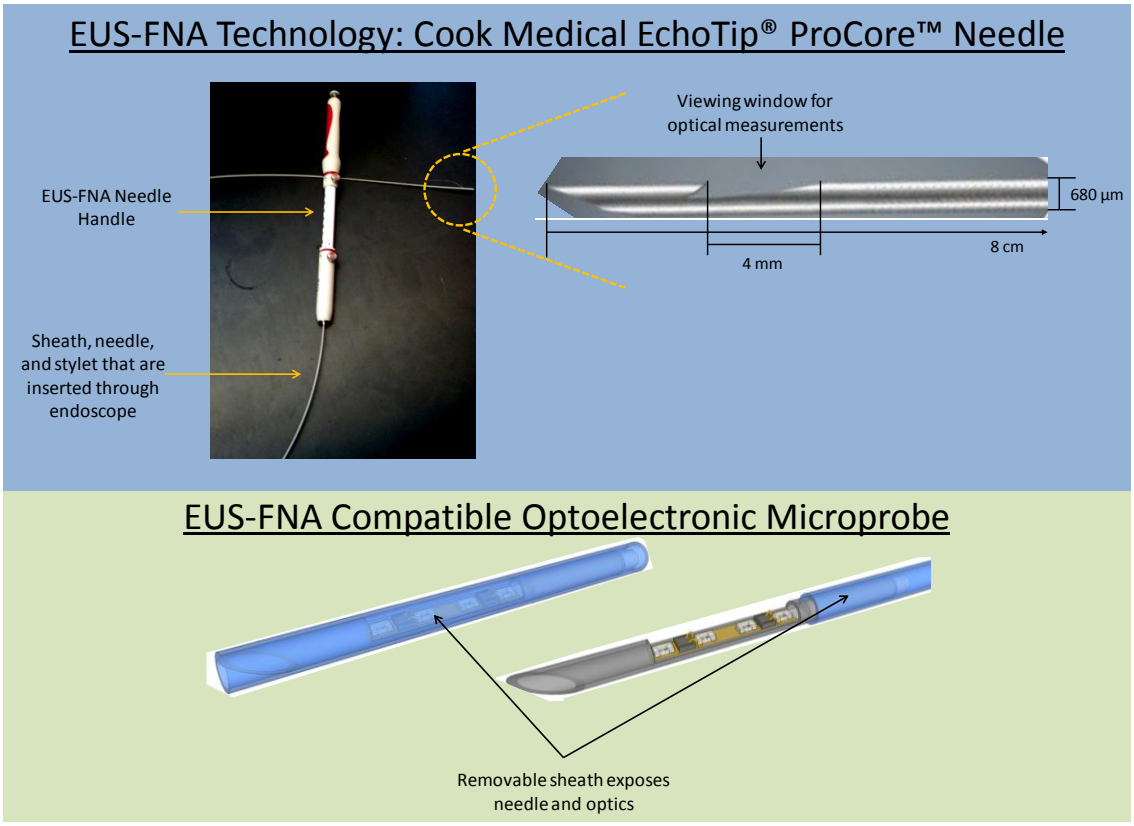

Figure 5.2 The optoelectronic microprobe is compatible with commercially-available EUS-FNA technology. Specifically, we have designed our microprobe to be compatible with FNA needles similar to the Cook Medical EchoTip® ProCore™ needles. (top) The EUS-FNA needle is compatible with current standard-of-care endoscopes employed for pancreatic procedures. The ProCore™ needle has a ~4mm window opening that will allow optical interrogation of tissue. (bottom) The microprobe electronics will be exposed when the protection sheath is removed to expose the needle tip. Once the sheath exposes ~2 cm of needle, the microprobe will be ready for optical measurements

5.1.4 Innovation

Using optical contrast for clinical tissue diagnostics is not a new idea [66, 90]. However, due to the challenges associated with accessing this internal organ, relatively little research in biomedical optics has been conducted in the human pancreas. Field effect

analysis [53, 118] of duodenal tissues adjacent to the pancreas and limited optical coherence tomography [119, 120] studies in the pancreas do not address the targeted clinical problem discussed here. Recent studies have established only feasibility for needle-based confocal laser endomicroscopy [116, 121, 122], as diagnostic utility has proven elusive even in large clinical studies [50, 121, 123].

In this chapter, we report optical-fiber-based technology to obtain the first optical spectroscopy data during pancreatic EUS-FNA procedures, based on the success of optical spectroscopy on freshly excised human pancreatic tissues [55] and corresponding pancreatic tissue classification algorithms using such optical data as inputs [22, 56, 57]. Our *ex vivo* data set has grown considerably and enabled the first robust analysis of the potential of optical spectroscopy to differentiate between malignant and non-malignant pancreatic tissues (Fig. 5.1).

Technically, the novel design of microfabricated optoelectronic components proposed here promises to revolutionize minimally-invasive tissue optical spectroscopy. To the best of our knowledge, this is the first-ever development of an integrated optoelectronic system for EUS-FNA compatible tissue diagnosis. Compared to the optical-fiber-based system we developed previously [10, 55], the proposed technology dramatically reduces cost (~ 20x) and instrumentation footprint (~100x) with comparable (and sometimes superior) optical performance including source power and detector sensitivity[12], and durability. Further, the proposed concept (Fig. 5.3) enables rapid volumetric mapping of pancreatic tissues to interrogate larger tissue volumes than those aspirated by EUS-FNA.

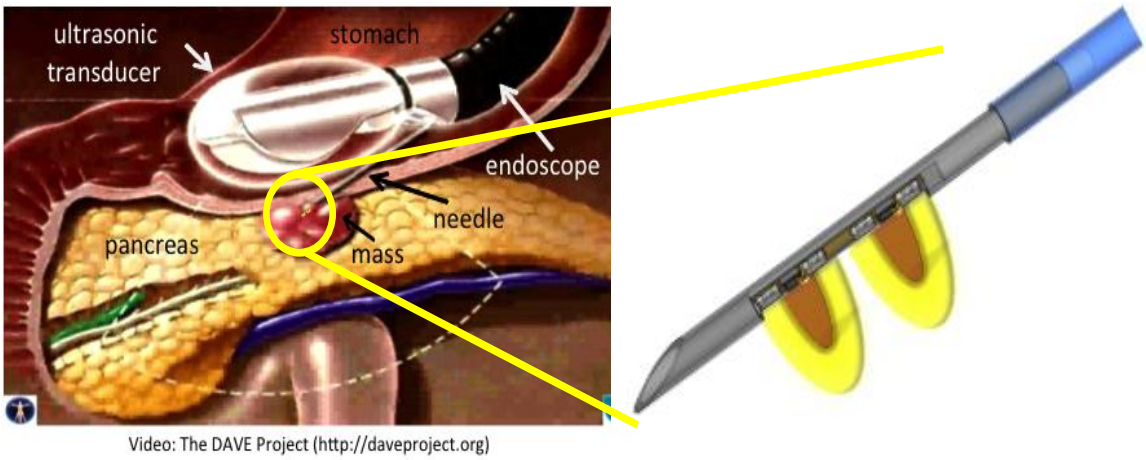

Figure 5.3 The optoelectronic microprobe is inserted through the hollow needle employed for EUS-FNA and rapidly interrogates tissue with pulses of light, providing real-time guidance for FNA (thereby improving sensitivity) or classifying tissue for diagnosis (proving the absence or presence of malignant disease). Shown are two source-detector sub-units to illustrate the technology's volumetric mapping capabilities with linear translation. Future designs could incorporate multiple repeated sub-units for tissue assessment over an extended tissue volume.

5.1.5 Design Concept and Requirement

To estimate a reflectance ratio at multiple points, the microprobe has two source-detector sub-units that consist of two LEDs (470 nm and 630nm) and one phototransistor (Fig. 5.4). The source-detector modules are arranged on a fabricated printed circuit board with contact pads and patterned electrical interconnections for all probe wiring. Measurements will be collected from both sub-units simultaneously, enabling real-time volumetric optical mapping of pancreatic neoplasia. Within each sub-unit, the two LEDs will be fired sequentially to avoid detector cross-talk.

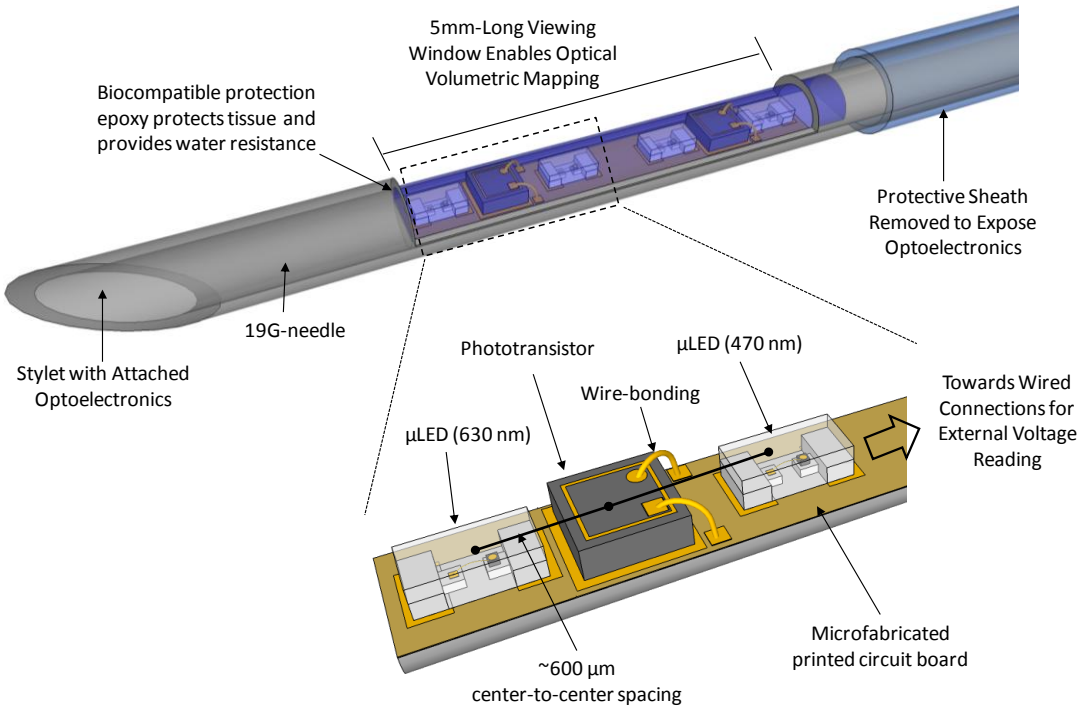

Figure 5.4 Illustration of proposed microprobe. The microprobe will be guided to the tissue site within a retractable protective sheath in the EUS hollow needle. Prior to measurement, the protective sheath will be retracted from the optical sensing window which is encapsulated with a transparent biocompatible epoxy to protect optoelectronics and electrical connections. The 5 mm long sensing window is created within a 19 Gauge EUS-FNA needle.

Successful integration with EUS-FNA requires the fabricated optoelectronic sensor (including optical sources, detectors, wiring, and connections) to fit within a hollow 19 Gauge [36, 50, 124] needle with a 0.85 mm inner diameter. For reflectance optical sensing, the diffused reflectance at multiple wavelengths must be measured with a high SNR. In particular, optical sensing must not be distorted by blood absorption, which has been demonstrated by our *in vivo* study on pancreatic surgery patients [125]. To correctly interrogate tissue sites, the probe must be moisture-proof. Heat dissipation from the optoelectronic components must be minimized to neither damage nor alter the optical properties of the target tissues. To minimize the error due to patient motion artifacts, the

optoelectronic probe must provide a real-time data analysis. Mechanically, the system must withstand endoscopic delivery. Critical design requirements and specification are described in Table 5.1.

Table 5.1 Design Requirements and Specifications of the Proposed Optoelectronic Microprobe compatible with a 19G hollow needle

Design Requirements	Specifications
Fit within 19G Needle	Diameter < 850 μm; Length < 5 mm
Multi-Spectral Sensing	SNR > 25 for 460 nm and 650 nm
Real-Time Analysis	< 1 s
Waterproof	No performance degradation in water during 5 minutes
Low Heat Generation	Temperature increase < 1°C
Mechanically Durable	No breakage or performance degradation during insertion

5.1.6 Objective and Design Scope

In this chapter, we describe the first prototype of optoelectronic microprobe. First, we fabricated a relatively large-scale printed circuit board with metal patterns to test assembly process and to characterize the performance of each optoelectronic component. The microfabricated board also has different designs on source-detection separations in the assumption of tissue optical sensing inside a 19G hollow needle in order to test the feasibility of reflectance and fluorescence sensing.

5.2 Methods

5.2.1 Engineering Analysis - Optical Simulation

Based on our preliminary surgical studies on human pancreatic tissues [55-57, 126], the die-level LED chips were selected for wavelengths of 460 nm (460DA3547, Cree, Durham, NC) and 650 nm (C4L 12T5, Chip4Light, Germany) because of their sufficient optical power with relatively low electrical power consumptions [11]. Furthermore, a suitable die-level chip detector for visible wavelengths (LA PD23HP1, Light Avenue, Germany) has a high radiant detection efficiency with adequate sensitivity [106]. Optical design feasibility was further demonstrated by Monte Carlo (MC) photon propagation simulations embedded in the commercially-available optical design software (ZEMAX®)[127] (Fig. 5.5 (a). Simulations employed performance specifications of the chosen components and optical tissue properties from *ex vivo* human tissue studies [57, 126]. Simulations predicted that when the LED emitted 0.5 mW of angularly distributed power, the phototransistor detected a power of > 3 mW/cm^2, generating a photocurrent of > 50 µA, which can be detected with high SNRs.

In addition, the ZEMAX® MC simulation results display the propagation paths of an individual photon that is detected by a photodetector (Fig.5.5 (b)). The distribution of these paths shows an optical interrogation volume of the optoelectronic microprobe. The depth of the optical sensing is approximately 500 µm. The assumption that the shape of this interrogation area is a hemisphere, results in a total volume of ~ 0.25 mm^3 for this arrangement, which is comparable to the volume simulated with a geometry of our previously adoped fiber optic probe.

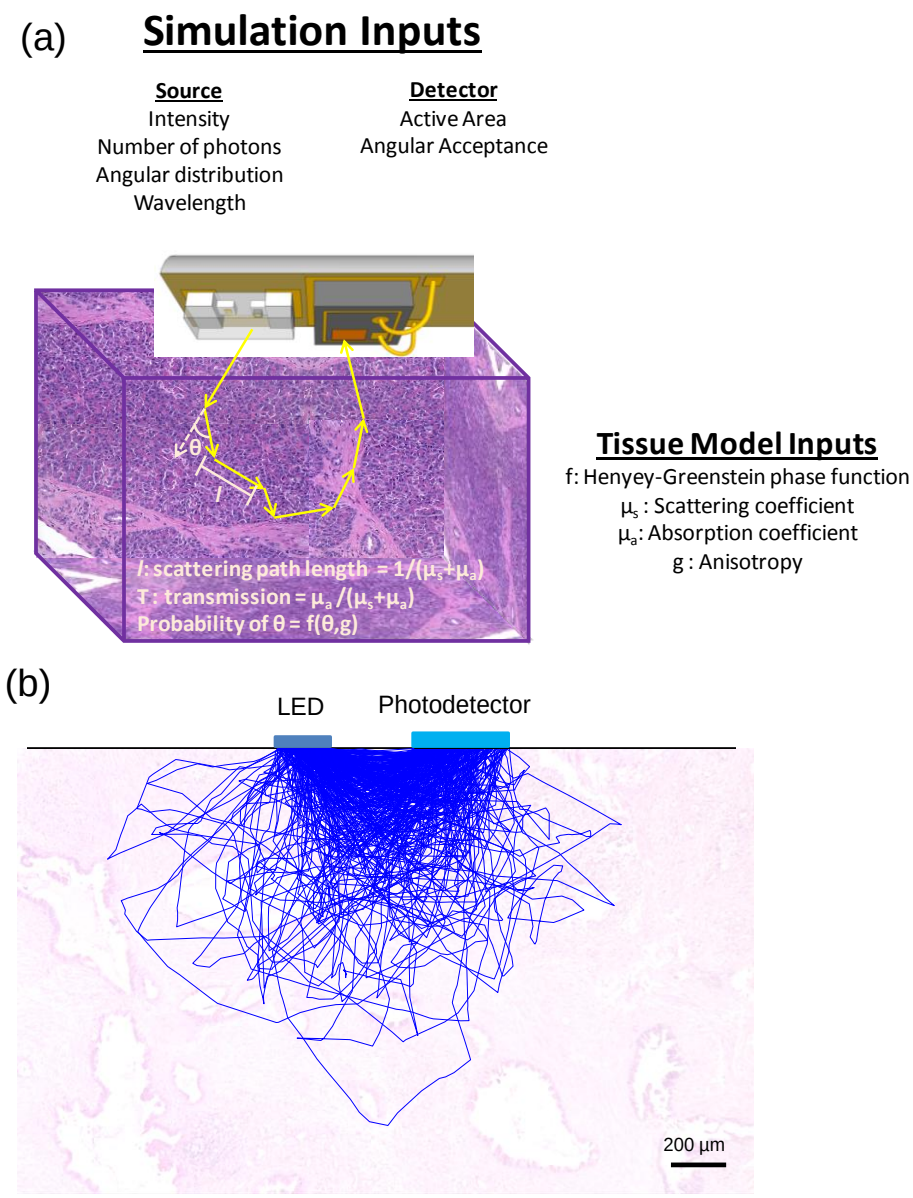

Figure 5.5 (a) ZEMAX® Monte-Carlo simulations were employed to assess the optical performance of the selected LED and PD. The LED is modeled as a source with the parameters of intensity, angular distribution and wavelength. The PD is modeled as a detector with the specific active area and angular acceptance angle. Launched photons from the LED propagate inside tissues according to pancreas-simulating tissue optical properties, including scattering and absorption coefficients. The mean pathlength and transmission are calculated from the tissue scattering and absorption coefficients. The angle of each scattering step is determined by a Henyey-Greenstein phase function. Photons reaching the active area of the phototransistor within the acceptance angle were detected. (b) Photon path visulization. The simulation result displays the propagation paths of the photons that are detected by the photodetector. The background histology image of an invasive adenocacinoma has the same scale bar with the photon path image to represent the areas that photon paths can cover when compared to a tissue structure.

The feasibility of the microprobe in distinguishing three different tissue types was also simulated. As the inputs for bulk scattering models in ZEMAX® , the mean pathlength and transmission for normal pancreatic tissues, chronic pancreatitis and adenocarcinoma were calculated from the estimated reduced scattering coefficients and absorption coeffficients obtained in the previous study (Table 5.2) [68]. The LED light intensities were 0.6 mW and 0.5 mW for the Blue and Red LEDs, respectively, according to their specifications.

The resulting intensity ratios R_{460}/R_{630} of detected photons are 0.76, 0.91 and 1.21 for normal, chronic pancreatits and adenocarcinoma respectively. To account for the difference in excitation intensity of two LEDs, the ratio of adenocarcinoma is scaled down to 0.71 (the averaged ratio from the experiments shown in the Figure 5.1 B) which makes the ratio of normal tissues and chronic pancreatitis 0.44 and 0.53, respectively, which are consistent with the ratios obtained from the experiments. This result reveals that optoelectronic microprobe employing reflectance intensity ratio at specific narrow wavelengths has potential to differentiate adenocarcinoma from normal and chronic pancreatits.

Table 5.2 Mean pathlength and transmission of three pancreatic tissue types

	Normal Pancreas		Chronic Pancreatitis		Adenocarcinoma	
	460 nm	630 nm	460 nm	630 nm	460 nm	630 nm
Mean Pathlength (1/mm)	0.113	0.076	0.080	0.063	0.049	0.061
Transmission	0.9933	0.9994	0.9958	0.9998	0.9974	0.9999

5.2.2 Engineering Analysis - Heat Simulation

Energy dissipation resulting from conversion of electrical power to optical power in emitting LEDs generates heat. Ensuring that no tissue is damaged by this heat is another important factor to be considered while designing devices that are to be inserted into the human body for *in vivo* sensing.

The ANSYS software is employed to simulate temparature changes around the pancreatic tissues when the microprobe is working. A human pancreatic head was modeled as a cube with an edge of 3 cm [128]. For the microprobe, two LEDs were located 1.2 mm apart from each other on a 150 µm-thick silicon wafer that was attached onto a steel stylet shaped in a half cylinder (Fig. 5.6 (a)). The properties related to heat tranfer, including heat capacity, density and thermal conductivity, of the pancreatic head, silicon wafer and steel stylet were inputs to the model for both steady-state and time-transient simlulations (Table 5.3) [129-131]. Because of the symetrical structure of the model, the simulation was perfomed only on one half of the model. Around 230,00 nodes were used to analyze this model. Specially finer sized elements were meshed around LEDs and silicon wafer since more significnat temperature variations exist in these areas. The power of heat was determined by equating it to the electrical power of 10 mW, which is necessary to emit the required optical power of ~ 1mW, estimated from the previous optical simulations. An initial temperature of the pancreas was set to 36.5 ˚C.

Table 5.3 Hear transfer properties of three components

	Pancreas	Silicon Wafer	Stylet (steel)
Thermal Conductivity (W/m˚C)	0.54	130	60.5
Heat Capacity (J/g˚C)	3.16	0.70	0.43
Density (g/cm3)	1.09	2.33	7.85

Simulation results show that the maximum temperature increases up to 37.4 ˚C, a second after both LEDs are switched on (Fig. 5.6 (c)). One second is our expected optical sensing time for a real-time feedback. While the maximum temperature shown in the graph occurs inside the LED bodies, the maximum temperature of the surrounding pancreatic tissues is found to be around 37.0˚C, which shows a less than an 1˚C increase. Even at a time point of 10 seconds when the temperature reaches near the steady-state point, the maximum temperature of the model is 38.1 ˚C and the maximum tissue temperature is about 37. 6˚C (Fig. 5.6 (d)). It is also noted that the area with temperature changes is limited to within 5 mm around the microprobe. These results demonstrate that the optical sensing of the microprobe would not damage assessed tissues and adjacent tissue area. Without the assumption of a perfect contact between LEDs and the surrounding tissues, indicating no thermal contact resistance, the maximum tissue temperature would reduce a bit more.

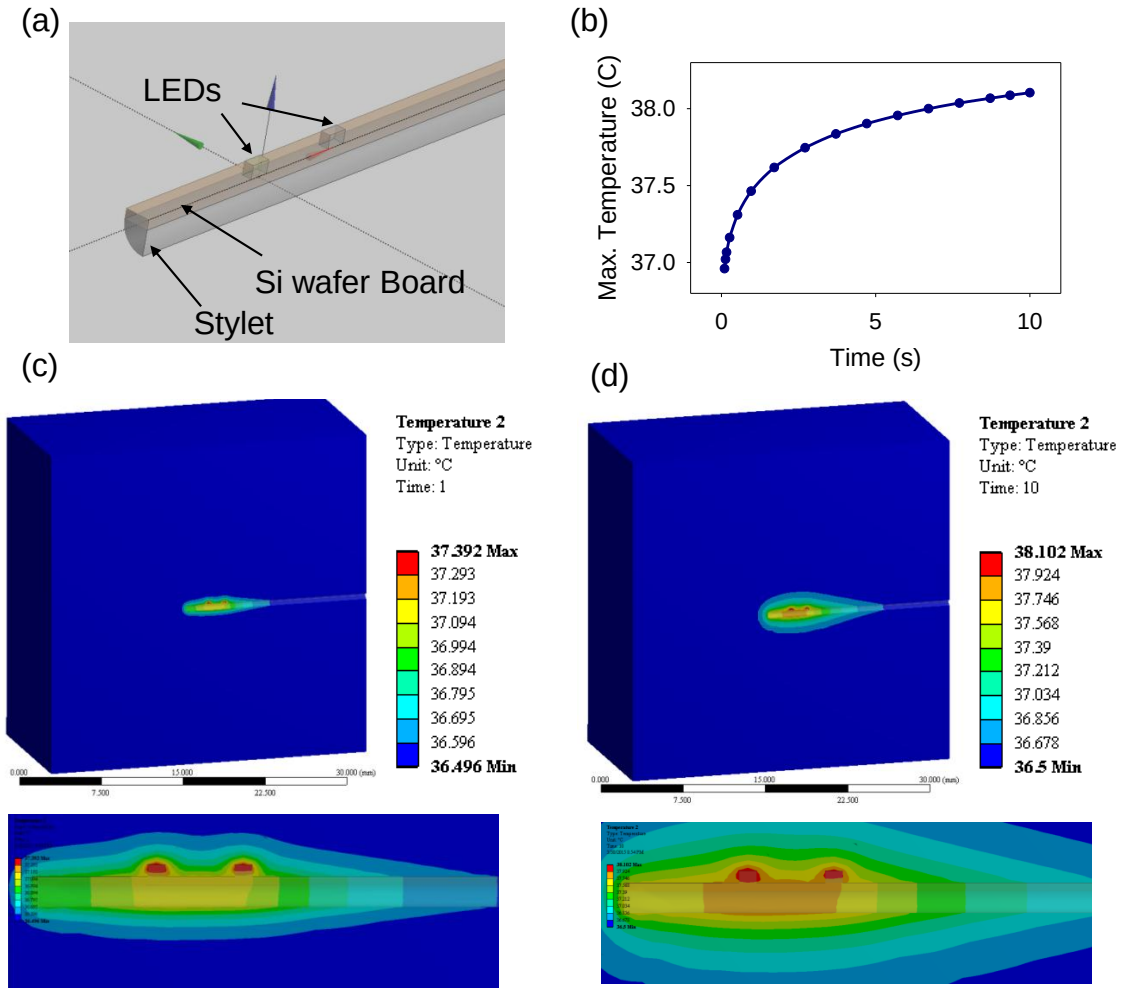

Figure 5.6 (a) 3D model of each component in the optoelectronic microprobe that affects heat distribution inside a tissue block (3 × 3 × 3 cm) mimiking the heat properties of human pancreas. The LED size is 300 × 300 × 200 µm (W × D × H) and legnthes of the silicon board and the stylet are both 17 mm (b) A transient curve shows that the maximum temperature increases by time. The maximum temperature reaches the steady-state in almost 10 second. (c) 3D temperature distribution 1 second after LED emission and 2D zoomed-in images of the heat distribution surrounding the microprobe. Colored bar indicates different temperatures for both images. (d) 3D temperature distribution 10 seconds after LED emission and 2D zoomed-in images of the heat distribution surrounding the microprobe. Although the area with the increased temperature become wider, it is only limited to about 5 mm around the microprobe, and the maximum temperature occurs only inside the LED bodies and is 1.5 ˚C higher than the initial temperature.

5.2.3 Fabrication

A prototype board for the optoelectronic microprobe was fabricated on a silicon wafer with 500 µm thickness (2 µm-thick oxide layer on the top for insulation) based on the well-established microfabrication procedures illustrated in Fig. 5.7. Cr/Pt/Au and In/Au layers were patterned by lift-off process for pad contacts of the light emitting diode (LED) and the photodiode (PD), and interconnections to external electrodes. Detailed steps are listed as follows.

a) A silicon wafer with 500 µm thickness was used

b) Photoresist (PR, SPR220 3.0, Microchem, Westborough, MA) was spin-coated and then patterned by a photolithography technique

c) Cr/Pt/Au (200/300/2500Å) were deposited onto the patterned photoresist by an electron beam (E-beam) evaporator (Enerjet Evaporator)

d) Then, the PR with undesired Au/Cr layer was lifted away to leave Cr/Au pattern

e) To bond the bottom side (Au) of the red LED (C4L 12T5, Chip4Light, Germany) and PD (LA PD23HP1, Light Avenue, Germany), Indium (In)-Au eutectic bonding process was chosen [132, 133]. Thus, In pads were defined within Cr/Au pattern by the second lift-off process. To pattern thick (6 µm) In pads, liftoff resist (LOR, LOR 30B, Microchem) was coated as an under-cut layer in a bi-layer lift-off process

f) The PR was coated onto the LOR. PR and LOR were developed by the photolithography

g) E-beam evaporator (Cooke Vacuum Products, South Norwalk, CT) deposited Au/In (1 nm/6 µm)

h) Lift-off process followed by soaking the device in the positive resist stripper (PRS 2000, Philipsburg, NJ) in 85℃ for 20 minutes and sonication until the pattern was completely defined

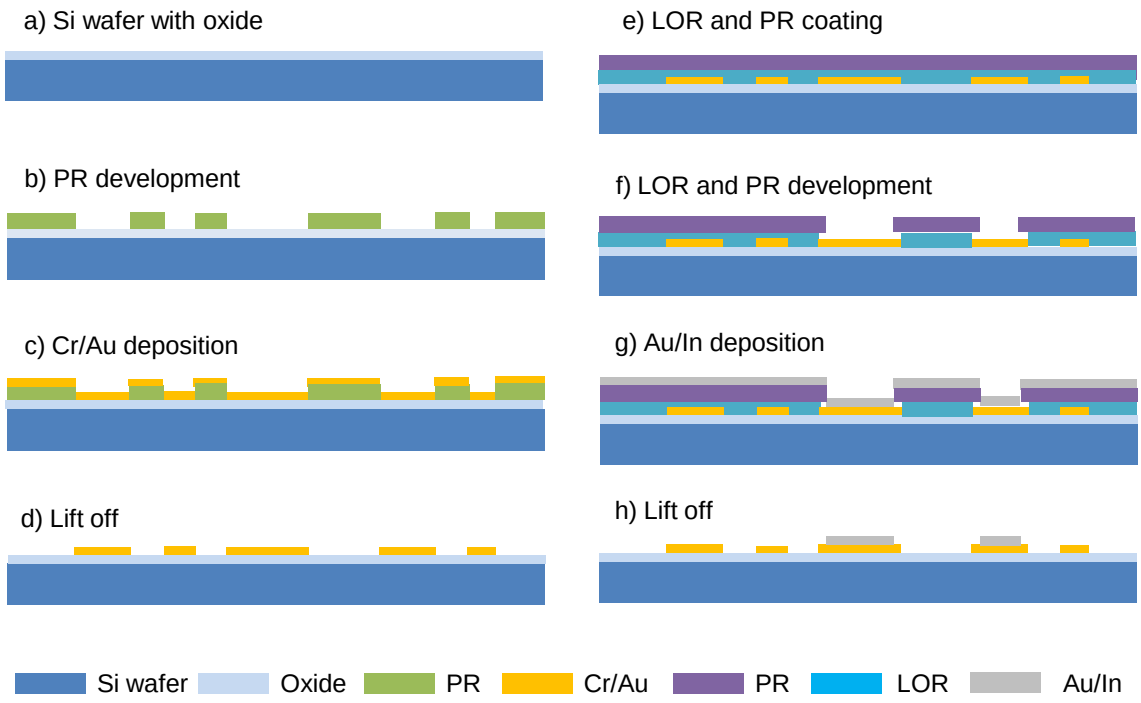

Figure 5.7 Prototype Fabrication Process

5.2.4 Assembly and Packaging

Prior to assembly, the fabricated bare board was rinsed by being immersed in acetone for 10 minutes and then in isopropyl alcohol (IPA) for 5 minutes. Assembly process consisted of four steps (Fig.5.8 (a)) First, In-Au eutectic bonding was performed by employing customized recipes to bond the bottom side of PD and Red LED onto the defined In pads. Temperature profile was programmed to provide the optimal temperature in the rapid thermal process tool (Jetfirst-100, Jipelec, Montpellier, France). 250 ℃ was maintained for 5 minutes to provoke In-Au eutectic bonding. Then, since the bottom side metal of the blue LED die (460DA3547, Cree, Durham, NC) was Au-Sn alloy (solder), which was known to a eutectic alloy, the temperature was up to 280 ℃ in 5 second based on the recommended flux eutectic reflow process [134]. Higher temperatures (290℃ and 300℃) were additionally attempted to find the optical condition. Once the eutectic bonding was formed between Au and In, higher temperature for Au-Sn eutectic bonding (~ 280˚C) than the eutectic temperature for In-Au (250 ℃) did not affect the bonding status [133]. The cathode pad on the top of the PD and Red LED were wire-bonded to the interconnections at the bottom of the board via 0.007 inch-thick Au wire. An optically transparent epoxy (NOR-61, Norland, Cranbury, NJ) encapsulated the bonded components (Fig. 5.8 (c)). A 30G-needle (Becton Dickinson, Franklin Lakes, NJ) delivered a drop of the epoxy to confine the volume covering all the three components. The epoxy was cured by 365 nm UV light exposure for 10 seconds. The fabricated prototype board was further cut to demonstrate the size of the optoelectronic probe that can be compatible with the inner diameter of a 19G hollow needle in comparison with a US dime (Fig. 5.8 (d)).

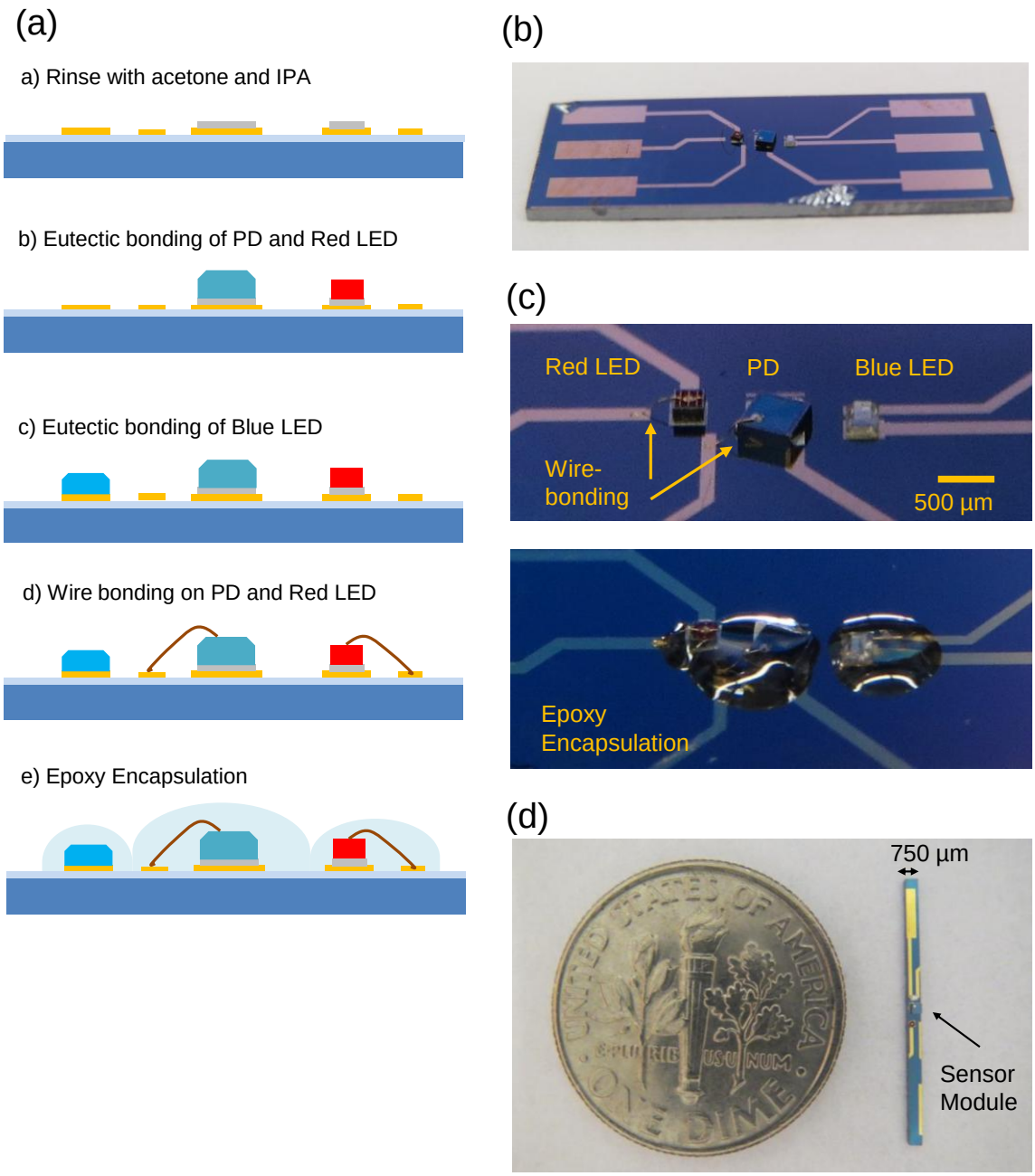

Figure 5.8 (a) Assembly process. (b) Assembled LEDs and PD on a large-scale fabricated prototype board (c) Zoomed-in image of eutectic bonded LEDs and PD, and epoxy encapsulation to protect the wire bonding and components. (d) Size comparison between the optoelectronic microprobe and a US dime.

5.2.5 System Controller Design

A custom electronic control module was designed and developed to drive two LED sources, read a current generated by detected photons on the PD. (Fig. 5.9) A microcontroller unit based on a 32-bit ARM core (ST32F405OE, STMicroelectronics, Geneva, Switzerland) was employed to sequence two LEDs, set the gain on a programmable gain amplifier (PGA), read the analog-to-digital converted (ADC) values and send the data to PC via a serial communication.

A single supply low noise LED current driver was implemented by employing a current output digital-analog converter (AD5452, Analog Device, Norwood, MA)[135]. A trans-impedance amplifier (TIA) was designed to convert the phototransistor current to a voltage signal with an amplification of 10^5 and 1^{st} order low-pass filter characteristics (cut-off frequency: 1 kHz). A programmable gain amplifier (LTC6910, Linear Technology, Milpitas, CA) enabled an additional gain adjustment via digital control, providing a high dynamic range [136]. The amplified voltage was subsequently filtered to yield a high SNR signal. A 16-bit analog-digital-converter (ADS1115, Texas Instruments, Dallas, TX) read the resulting voltage at 50 kHz.

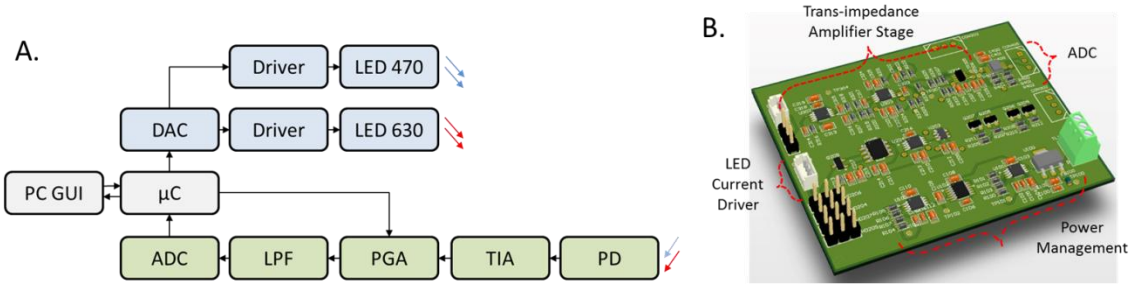

Figure 5.9 A. Block diagram of the custom electronic module (GUI: graphical user interface, µC: microcontroller, DAC: digital-analog converter, ADC: analog-digital converter, LPF: low pass filter, PGA: programmable gain amplifier, TIA: Trans-impedance amplifier) B. 3D rendered image of the designed signal conditioning module

5.2.6 Components Characterization

5.2.6.1 LED Characterization

I_f-V_f curves for both LEDs were obtained by adjusting the forward voltage in a 0.1 V step size using a digital power supply (E3631A, Keysight Technology, Santa Clara, CA), and recording the corresponding forward current flowing through the LEDs. For the blue LEDs, I_f-V_f curves of three different sets according to different bonding temperatures (280, 290 and 300 ℃) were measured to find the best bonding tempereture. For the red LEDs, to investigate the effect of the second eutectic bonding of the blue LEDs, two sets of the red LEDs were measured before and after the eutectic bonding for the blue LEDs. Optical powers of the emitted beam were measured using an integrating sphere coupled with a photodetector (3A-IS-V1, Ophir-Spiricon, North Logan, UT) to account for the diverging emission of both LEDs. The emission wavelength was recorded by an optical spectrometer (HR2000, Ocean Optics). Forward voltages were also varied for each LED to check for potential wavelength shift.

5.2.6.2 PD Characterization

The linearity between the detected optical power and the PD output was assessed by emitting blue and red LEDs, which were characterized with I_f-optical power curves in the chapter 5.2.5.1, towards the PD at a specific distance. The blue LED was located 45 mm away from the PD and driven with the forward voltage varying from 2.9 V to 3.5 in 0.1 V step. The output voltage at the TIA coupled with the PGA was read by an oscilloscope (TDS220, Tektronics, Beaverton, OR). The resistance determining a gain in the TIA was 100 K to provide the gain of 10^5. With the gain of the PGA set to 100, the total gain of the system was 10^7. The distances between PD and LEDs were determined to make the

output voltage swing from 0 to 5V, which was a supply voltage of the TIA and PGA. The red LED located 60 mm away from the PD because the sensitivity of the PD in 630 nm was higher than in 460 nm. The same measurement was performed on the red LEDs.

5.2.6.3 Feasibility on Reflectance Sensing

To test the feasibility of reflectance sensing of the fabricated prototype, optical tissue-simulating phantoms were created. The phantoms comprised Intralipid (I141, Sigma Aldrich, St. Louis, MO) as a scatterer in an agar-based matrix. Specifically, a set of optical phantoms with three different IL concentrations (0.4, 0.8 and 1.2 mL of IL in 20 mL of de-ionized water) were manufactured to investigate the relationship between scatterer concentration and detected reflectance at the given geometry and angular sensitivity of source and detector. The phantoms were prepared in the petri dish with a diameter of 60 mm and a height of 15 mm, and placed on the black holder to prevent the reflectance from the bottom. The prototype sensing module was placed onto the solid phantom and slightly pushed to make sure the LED and PD contact the surface (Fig. 5.10). The probe interrogated three spots on the phantoms and the measured voltages accounted for ambient voltage background.

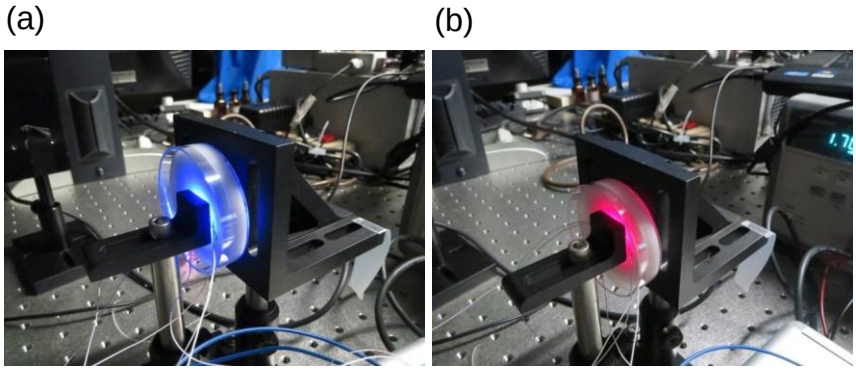

Figure 5.10 Reflectance sensing on tissue simulating optical phantoms with (a) 460 nm and (b) 650 nm.

5.2.6.4 Feasibility Test for Fluorescence Sensing

The feasibility of fluorescence sensing of the developed microprobe was assessed using standard fluorescence solutions. For tests, a small and thin long pass filter passing only fluorescence to the detector was not available. Thus, two microprobe modules were employed, one each for 460 nm blue LED emission and PD detection, respectively (Fig. 5.11 (a)). The blue LED in one device excited 10 µM Rhodamine B in a cuvette with a 1cm-pathlength, and an off-the-shelf long pass filter with a 488 nm cutting wavelength (FF01-488/LP, Semrock, Rochester, NY) (Fig. 5.11 (b)) blocked 460 nm excitation light and passed only fluorescence emission (peak emission was around 580 nm) towards the PD in another device. The forward voltage of the LED increased and the corresponding voltages on the TIA were obtained.

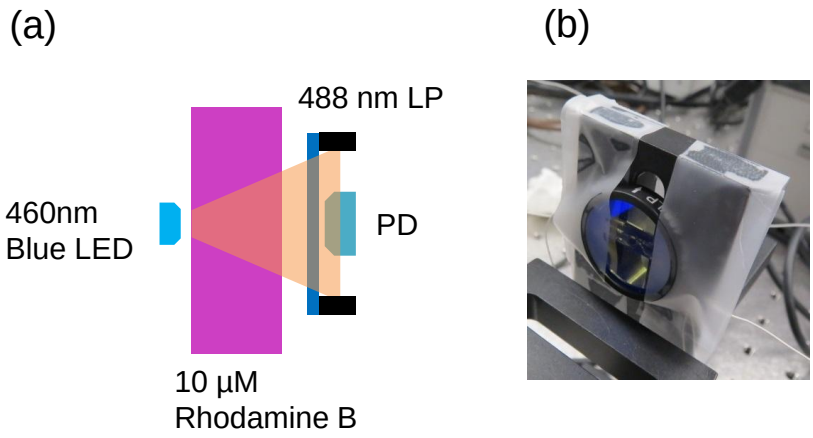

Figure 5.11 (a) Fluorescence Measurements Setup (b) A long pass filter (LP) with 488 nm cutting wavelength was set up very closely to the PD so that only light passed the LP can be detected by the PD

5.3 Results

5.3.1 Characterization of the Assembled Components

5.3.1.1 Blue LED - Cree DA460

Figure 5.12 (a) shows I_f-V_f characteristics of assembled blue LEDs depending on different temperatures applied for the eutectic bonding process. At the temperature higher than 280 ℃, I_f-V_f performance is deteriorated and inconsistent. Measured If-Optical power curves show a good linear relationship and consistency between three samples (Fig. 5. 12 (b)). Peak emission wavelength is 457 nm with a full-width-half-maximum of around 30 nm (Fig. 5. 12 (c)). No prominent wavelength shift depending on the forward voltage is observed (Fig. 5. 12 (d)).

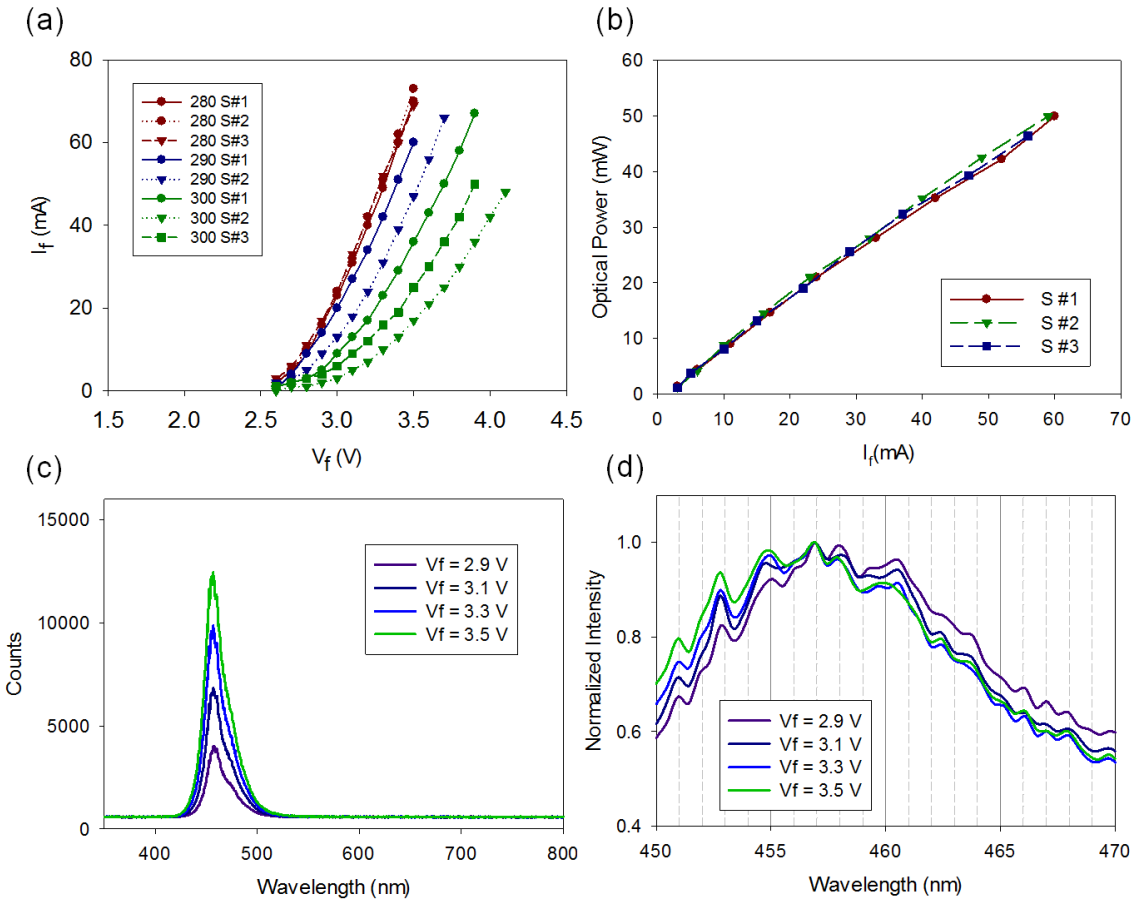

Figure 5.12 (a) V_f-I_f curves of bonded blue LED depending on different bonding temperatures (b) Measured optical power versus the forward current on three different samples (c) Emission spectrum depending on V_f (d) Zoomed-in spectrum at the peak emission wavelength

5.3.1.2 C4L Red LED

The bonded red LEDs after the eutectic bonding of blue LEDs shows the same performance as the LEDs before the bonding (Fig. 5.13 (a)). This indicates the second eutectic bonding does not affect the results of the first eutectic bonding. Measured optical powers are proportional to the applied forward voltages with consistency between three samples. At a regular forward current of 50 mA, the optical power is 22.5mW. The measured peak emission wavelength is around 650 nm with a FWHM of 20 nm. The wavelength is shifted at 1/15 nm/mA rate.

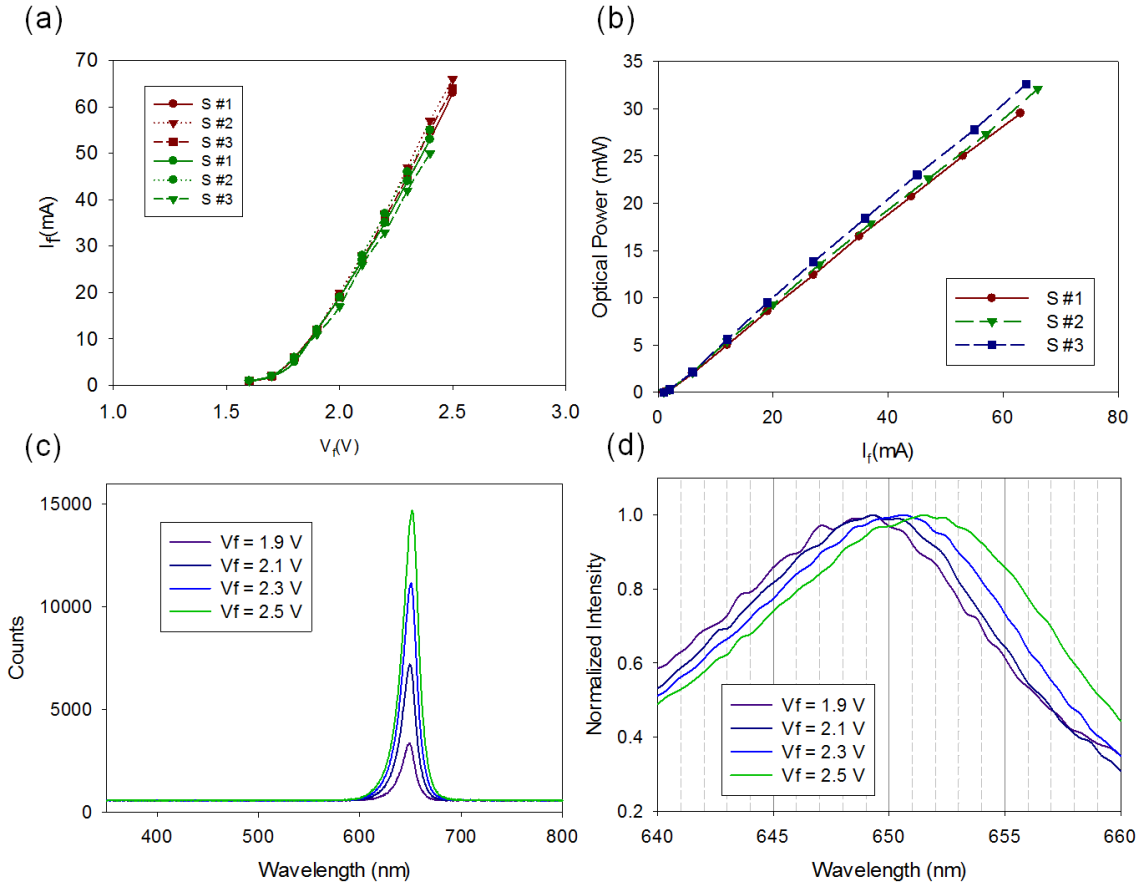

Figure 5.13 (a) V_f-I_f curves of bonded red LED before (Green) and after (Red) the second eutectic bonding. Each set has three samples (b) Measured optical power versus the forward current on three different samples (c) Emission spectrum depending on V_f (d) Zoomed-in spectrum at the peak emission wavelength

5.3.1.3 Photodiode

Figure 5.14 displays a linear relationship between the forward current of the sources (optical powers detected on the PD) and detection voltage (current flowing in the PD) at the TIA output in two PDs at both wavelengths. Given the total gain is 10^7, the dark current of the PD can be calculated as ~1V/10^7 (A/V) = 0.1 µA. Two PDs show the consistent performance in the red wavelength, as indicated by the same slope only with a slight difference in dark voltages. However, the PD sample #2 shows a higher slope in the blue wavelength.

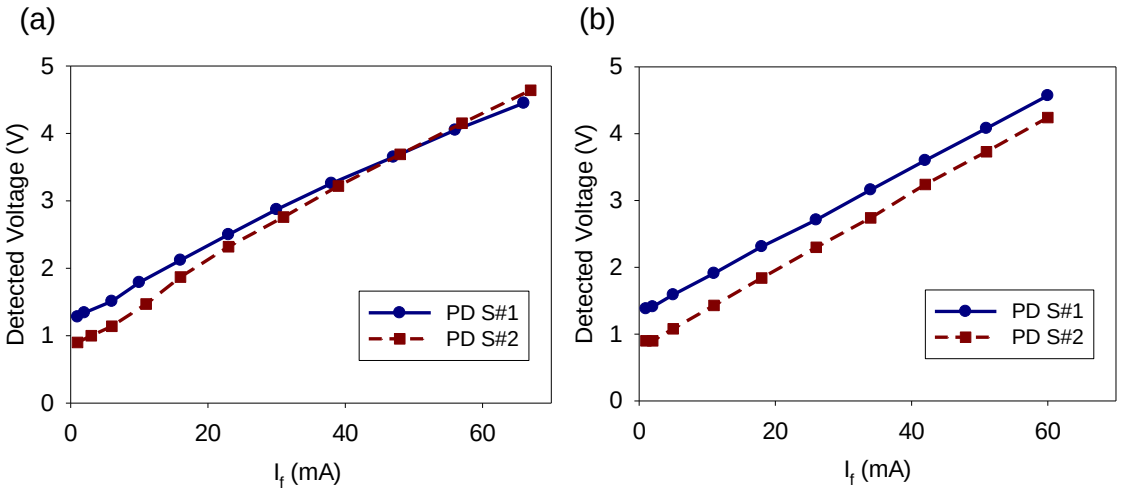

Figure 5.14 Voltage at the TIA output according to the forward currents on (a) blue LEDs and (b) red LEDs

5.3.2 Characterization of Reflectance Sensing on Tissue Simulating Phantoms

For reflectance sensing, the total gain of TIA was set to 10^5 and the forward currents were 2 mA and 6 mA for red and blue LED, respectively in order to avoid the saturation in the TIA output voltage by the direct detection of the emission light. With gain of 10^5, the dark voltage was 0.1 mV. The voltages measured by the direct detection were 0.23 mV in 460 nm and 0.39 mV in 650 nm, respectively. The detection voltages increased in

higher concentrations of Intralipid, indicating the reflectance sensing is feasible (Fig. 5.15). Larger error bar in 460 nm sensing probably indicates that 460 nm sensing could be more sensitive than 650 nm sensing setup.

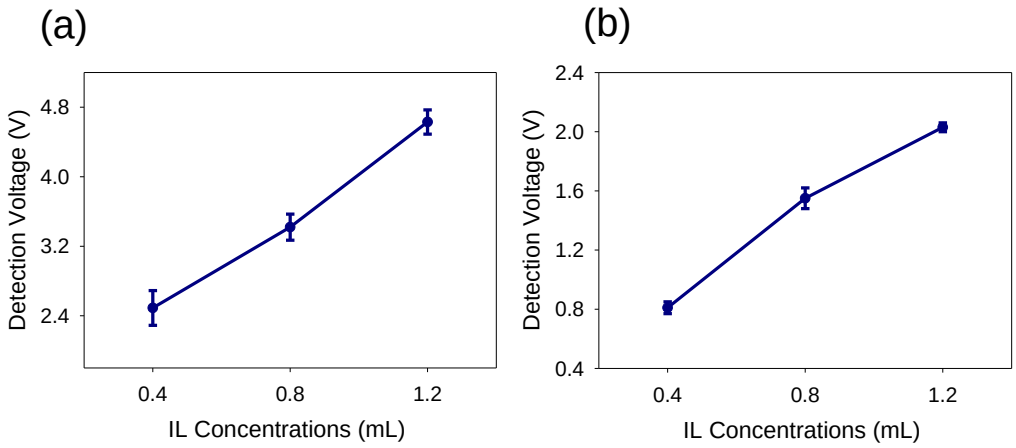

Figure 5.15 Reflectance sensing results on optical phantom with different scatterer concentrations at (a) 460 nm and (b) 650 nm. Error bar presents the standard deviation.

5.3.3 Fluorescence Feasibility Test

With a total gain of 5×10^6 and a forward current of 40 mA on blue LED, the PD detection voltage was 0.10 V without a fluorescence sample, close to the dark voltage of 0.09 V ensuring the block of 460 nm emission light by the 488 nm LP filter. When the sample is placed in the excitation and detection path, the fluorescence detection voltage is up to 1.31 V (Fig. 5. 16 (a,b)). Fluorescence detection voltage increases as the excitation power increases. (Fig. 5.16 (c))

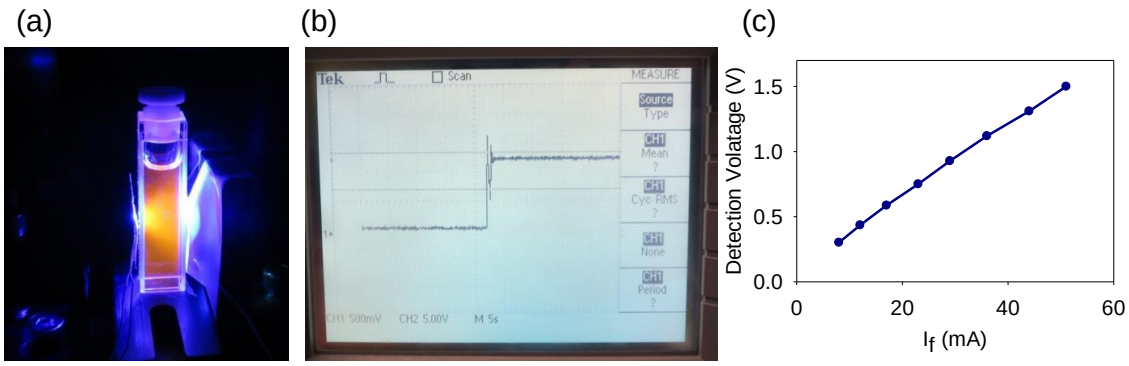

Figure 5.16 (a) Rhodamine B fluorescence emission excited by 460DA3547 blue LED (b) Oscilloscope screen shows the voltage at the TIA output increases when a cuvette containing 10 µM of Rhodamine B solution is placed between the blue LED and PD. (c) Detection voltages corresponding to different forward currents on blue LED. Fluorescence emission increased linearly to the excitation intensity.

5.4 Conclusion

The first prototype optoelectronic microprobe prototype was successfully fabricated and assembled. Along with the characterization of optoelectronic components, the results of the feasibility tests on reflectance and fluorescence sensing demonstrate that the optoelectronic microprobe has the potential to non-invasively assess human tissues located at the sites with a constrained geometry.

Chapter 6.
Conclusion and Future Direction

6.1 Summary and conclusions

The primary goal of this dissertation was to develop (a) mathematical (b) computational and (c) instrumental tools to address technical needs to promote the clinical translation of quantitative tissue optical sensing.

In Chapter 2, we developed the Direct Fit Photon Tissue Interaction (DF-PTI) model to rapidly and quantitatively analyze reflectance spectra obtained from human tissues. The new DF-PTI model showed increased rapidity and accuracy in fitting the acquired tissue reflectance than the previously developed PTI model because of the adoption of a non-linear least mean square algorithm. Additionally, the DF-PTI model extracted the more numbers of biophysically-relevant parameters such as blood vessel size and nuclear refractive index, which are fixed in the original model, and did not require *a priori* information like "the canonical normal" to scale the spectra of unknown tissue types.

The developed DF-PTI model was employed to assess Intraductal Papillary Mucinous Neoplasia (IPMN), a common precursor lesion of pancreatic cancer. With difficulties in data acquisition, this pilot study investigated 8 IPMN sites in the freshly excised pancreas specimen from 2 patients and compared the analysis results to normal and adenocarcinoma. The extracted parameters associated with cellular nuclear size and refractive index of IMPN were higher than normal and similar to those associated with adenocarcinoma, which is consistent with pancreatic tissue histology and the previous studies reporting the refractive index in neoplastic tissues. The extracted parameters

associated with collagen fluorescence contribution were also higher in IPMN and adenocarcinoma than in normal. The higher collagen contribution was attributed to abundant fibrotic stroma. The results demonstrated the potential of optical spectroscopy coupled with an analytical model for characterizing pre-cancerous neoplasms in human pancreatic tissues.

In Chapter 3, we proposed a simple and rapid scattering analysis model to evaluate the potential of real-time cancer detection in the pancreas using reflectance spectroscopy. Clinically-compatible reflectance and fluorescence spectrometer was employed to interrogate the freshly excised pancreas during the surgery. In total, 105 sites from 18 patients, including 39 normal, 32 chronic pancreatitis and 34 adenocarcinoma sites, were analyzed. Prior to employing the scattering model, a Principal Component Analysis (PCA) was performed on both fluorescence and reflectance, and a tissue classification algorithm employing PCA parameters revealed that the reflectance-only dataset showed the classification performance comparable to the performance of hybrid approach (reflectance and fluorescence), which provide a scientific rationale for the following reflectance analysis.

The simple scattering model was employed to accurately extract the reduced scattering coefficients and scattering power from the obtained reflectance spectra. The estimated reduced scattering coefficient of adenocarcinoma (10.53 ± 0.43 cm^{-1}, mean ± SE) was statistically lower than normal (15.96 ± 0.36 cm^{-1}) and chronic pancreatitis (12.66 ± 0.42 cm^{-1}), while the scattering power increased in adenocarcinoma (0.77 ± 0.05, mean ± SE), compared to normal (0.21 ± 0.01) and chronic pancreatitis (0.51 ± 0.06). The classification algorithm employing these two scattering parameters distinguished

malignant tissues (adenocarcinoma) from non-malignant tissues (normal and chronic pancreatitis) with 94% sensitivity and 75% specificity. Because of its compact/cost-effective instrument, rapid data acquisition and quantitative analysis, and the diagnostic power of scattering parameters, diffuse reflectance spectroscopy has the potential to become real-time optical biopsy compatible with current clinical procedures.

In Chapter 4, we devised the Ray-Traced Monte Carlo simulation method to computationally model fluorescence excitation and detection by optical spectroscopy and imaging systems on turbid media. The RTMC combined the optical design software, ZEMAX® for ray-tracing through optical systems and Monte Carlo simulation for modeling photon propagations inside turbid samples. The developed RTMC method was first verified computationally on epithelial tissue models mimicking colon cancer. The source-detection configurations employing fiber optic probes with flat-ended tip were modeled by both RTMC method and the original gold-standard MC code, and the simulation results were compared. The percent errors between the MC and RTMC were 3.5 % and 7.4 % for reflectance and fluorescence, respectively. Additionally, the RTMC method was experimentally verified on optical phantom measurements with a depth-sensitive fluorescence spectroscopy system. Two-layered solid phantoms were fabricated with a top agarose-based layer with Rhodamine 6G on top of the PDMS-based bottom layer with POPOP. Depth-sensitive spectroscopy measurements were performed by scanning a focal point in the z-direction up to 1 mm. Top layer sensitivity was calculated from the measured fluorescence spectra and compared with results of the RTMC simulation that optically modeled phantoms and optical systems. The simulation results predicted the actually measurements within 15%, indicating that the RTMC was able to

accurately model fluorescence excitation and detection on turbid media by spectroscopy/imaging systems that employ complex optical components. The verification results suggested that the developed RTMC method has potential as an efficient and useful computational tool for designing or assessing fluorescence detection systems in turbid media.

In Chapter 5, we designed and developed a prototype of the optoelectronic microprobe for volumetric optical sensing during the EUS-FNA procedure with an aim of more accurate diagnosis of pancreatic neoplasia. Die-level optoelectronic components (two LEDs at 460 nm and 650 nm and one PD) were selected to meet the mechanical, electrical and optical requirements. The prototype board was fabricated based on standardized microfabrication technology, including photolithography and a lift-off process. LEDs and PD were bonded onto the fabricated board via two consecutive eutectic bonding processes, and wire-bonding followed to connect the top electrodes of the LED and PD to the bottom pads. The low-noise LED driver and trans-impedance amplifier coupled with the programmable gain amplifier were designed and implemented for controlling the optical sensing and monitoring.

The assembled LEDs were characterized by obtaining I_f-V_f curves, I_f-Power curves and emission wavelength, and the PD was characterized by measuring dark current and the detected optical power-I_{PD} curve, to ensure that the assembly process did not affect the performance of the chips. The feasibility of reflectance sensing was tested on tissue scattering phantoms with different concentrations of Intralipid, and the results showed a linear relationship between the scattering properties and the detected reflectance. For fluorescence, a 10 μM Rhodamine B solution was excited by the 460 nm LED and the

fluorescence was able to be detected by the PD coupled with a long-pass filter that cut excitation wavelength. These test results demonstrated that the optical sensing module employing micro-optoelectronic chips was feasible. Further characterization and upgrading of the board design to make it compatible with a 19G needle will be the next step for this project.

The major contribution of this dissertation can be summarized as follows:

- We developed an improved mathematical model called DF-PTI that can rapidly extract the parameters associated with nuclei size, refractive index, blood vessel size and collagen contribution in human tissues without a need of *a priori* information.
- We reported the first-ever optical spectroscopic analysis on a precursor lesion of pancreatic cancer, IPMN.
- We revealed that reflectance spectroscopy alone could be as useful as the multimodal approach in terms of an accurate diagnosis of pancreatic cancer, representing the potential of real-time optical biopsy resulting from its compactness, cost-effectiveness and speed of analysis.
- We made the first estimation of the reduced scattering coefficient and scattering power at a specific wavelength range in human pancreatic tissues. This estimation was based on tissue-simulating scattering phantoms.
- We presented the first-ever assessment of pancreatic tissue scattering properties as an optical biomarker for pancreatic cancer diagnosis by employing a novel tissue

classification algorithm constructed with GEE that accounts for he intra-patient correlation.

- We created the first-ever ray-traced Monte Carlo (RTMC) computational method to model a complete ray path on fluorescence excitation and detection in turbid media.
- We manufactured the first two-layered optical phantom, in which both layers are solid; an agar-based top layer containing Rhodamine 6G and Intralipid and a PDMS-based bottom layer mixed with titanium oxide and POPOP. This phantom required no additional sheet which could potentially have an unknown impact on the optical measurement between the two layers because of the hydrophilic and hydrophobic properties of top and bottom layer, respectively.
- We designed and developed the first-ever prototype of an optoelectronic microprobe including micro-sized die-level chip LEDs and PD, which will fit within a 19G hollow needle and potentially provide the flexibility of source-detector configurations for adjustment of optical interrogation volumes.
- We evaluated the performance of assembled components in the prototype, and tested the feasibility of reflectance sensing on tissue-simulating scattering phantoms and fluorescence sensing on standard fluorophores.

The work in this dissertation has been presented and documented as cited below:

Chapter 2

- **Lee, S.Y.,** Lloyd, W.R., Chandra, M., Wilson, R.H., McKenna, B., Simeone, D., Scheiman, J., and Mycek, M.-A., "Characterizing human pancreatic cancer precursor using quantitative tissue optical spectroscopy," *Biomedical Optics Express*, 2013; 4(12):2828-34
- Lloyd, W.R., Wilson, R.H., **Lee, S.Y.**, Chandra, M., McKenna, B., Simeone, D., Scheiman, J., and Mycek, M.-A., "*In vivo* optical spectroscopy for improved detection of pancreatic adenocarcinoma: a feasibility study," *Biomedical Optics Express*, 2014; 5(1):9-15
- **Lee, S.Y.,** Lloyd, W.R., Wilson, R.H., Chandra, M., McKenna, B., Simeone, D., Scheiman, J., and Mycek, M.-A., "Photon-tissue interaction model for quantitative assessment of biological tissues" *Proc. of SPIE, 8935-80*, San Francisco, CA, USA, 2014

Chapter 3

- **Lee, S.Y.,** Wilson, R.H., Lloyd, W.R., Chandra, M., Lee, O., Scheiman, J., McKenna, B., Simeone, D., Taylor, J., Lloyd, W.R., Mycek, M.-A., "The Prospect of Real-Time Cancer Detection in the Pancreas Using Diffuse Reflectance Spectroscopy" (journal manuscript in preparation)
- Wilson, R.H., Chandra, M., Scheiman, J., **Lee, S.Y.,** Lee, O., McKenna, B., Simeone, D., Taylor, J., Mycek, M.-A., "Tissue classification Using Optical

spectroscopy accurately differentiates cancer and chronic pancreatitis" (submitted)

- Wilson, R.H., Scheiman, J., Chandra, M., Lloyd, W.R., L.–C. Chen, **Lee, S.Y.,** Taylor, J., Lee, O., Simeone, D., McKenna, B., Mycek, M.-A., "Optical Method for Real-Time Diagnosis of Pancreatic Cancer", *Pancreas*, 43, 8, 1405, 2014
- Scheiman, J., Wilson, R.H., Chandra, M., Simeone, D., McKenna, B., Taylor, J., Lee, O., Lloyd, W.R., **Lee, S.Y.,** Mycek, M.-A., "Optical Method for Real-Time Diagnosis of Pancreatic Cancer", *Pancreas*, 43, 8, 1422, 2014
- Scheiman, J., Wilson, R.H., Chandra, M., McKenna, B., Simeone, D., Taylor, J., Lee, O., Lloyd, W.R., **Lee, S.Y.,** Mycek, M.-A., "Optical Spectroscopy Distinguishes Pancreatic Cancer from Non-malignant Pancreatic Tissues", *Gastroenterology*, 146, 5, S-574, 2014

Chapter 4

- **Lee, S.Y.,** and Mycek, M.-A., "Ray-traced Monte Carlo Simulation for Fluorescence Measurements in Turbid Media" (to be submitted)

Chapter 5

- Mycek, M. -A., **Lee, S. Y.,** Lloyd, W. R., Scheiman, J., Yoon, E., Fan, W., "Optoelectronic Microprobe for Tissue Diagnostics", (Invention report submitted OTT #6217)

6.2 Future Research Direction

6.2.1 Optical Detection of Pancreatic Cancer

The reflectance spectroscopic technique reported in Chapter 2 and 3 is potentially compatible with the current EUS-FNA procedure. FNA-needle compatible fiber-optic spectroscopy has been demonstrated to be capable of characterizing lymph node physiology *in vivo* [36, 67]. A single channel fiber optic (600 μm) was employed in this study coupled with a mathematical model to evaluate physiological parameters related to blood content. Although the same dimension of optical fiber with the mathematical model may possibly be employed for future *in vivo* pancreas studies, a dual channel with smaller diameter (~ 300 μm) would also appear to be feasible, considering the internal diameter of conventional FNA needles.

Because of its great classification performance for distinguishing adenocarcinoma sites from normal tissues, (sensitivity 94% and specificity 95%), reflectance spectroscopy can be employed for surgical margin detection during the surgery. The rapid acquisition and analysis of one reflectance spectrum could potentially enable an advanced design for a scattering imaging system by incorporating 2-dimensional scanning in order to provide spatial information [137].

6.2.2 Ray-Traced Monte Carlo Simulation

Upgrade for time-resolved fluorescence model

The current RTMC method enables steady-state fluorescence only simulations. However, time-resolved fluorescence simulation could be achieved by adopting lifetime determination methods commonly employed for a time-gated fluorescence lifetime imaging (FLIM) system. Inside the current MC codes, an internal function records the

traveling time of each individual fluorescence photons. A virtual gating could be implemented in the code to collect all the fluorescence photons exiting the sample surface within a specific time range and then export them as one geometrical distribution file that can be fed into a ZEMAX® detection model. For the four-gate model, four geometrical distribution files will be generated, and the ZEMAX® detection model will run four times with the corresponding distribution files as a source, resulting in the simulated gated-fluorescence intensity. A ZEMAX® macro program could automate this repetitive process. The four intensity values detected by ZEMAX® would be employed in an analytical least square lifetime determination based on equation 6. 1

$$\tau = -\frac{N(\sum t_i^2) - (\sum t_i)^2}{N\sum t_i \ln I_i - (\sum t_i)(\sum \ln I_i)} \qquad \text{Equation 6.1}$$

where τ is the lifetime, I_i is the gated intensity at the gate i, t_i is the gate delay of the gate i, and N is the number of gates. All sums are over i.

Further Validation of the design of a confocal fluorescence probe in the Tissue Engineering Field

To evaluate the applicability of the developed RTMC method, it could be validated on the design of a confocal fluorescence probe to assess the viability of manufactured tissue-engineered constructs for oral or skin grafts in functional tissue recovery. The viability can be assessed by measurement of the endogenous fluorescence of metabolic co-factors such as NAD(P)H and FAD. However, selectively measuring the fluorescence from the thin cell layer is very challenging to because of high scattering in the top keratin layer and the abundant collagen fluorescence from a bottom dermal equivalent of the constructs. Compared to previously implemented fiber-optic system, the confocal

fluorescence probe is capable of finer resolution depth-sectioning that effectively suppresses the strong keratin and collagen fluorescence and extracts only the epithelial fluorescence.

An example of the preliminary design is shown as Figure 6.1.All the selected lenses are commercially-available and have small footprints (diameter < 5 mm), which would enable a future probe to access the various human sites. RTMC simulation could be employed to determine the optimal design parameters. The optical probe system could be modeled in the non-sequential mode of ZEMAX® and fluorescence emission and propagation inside the constructs could be simulated via MC codes based on the optical properties of the constructs.

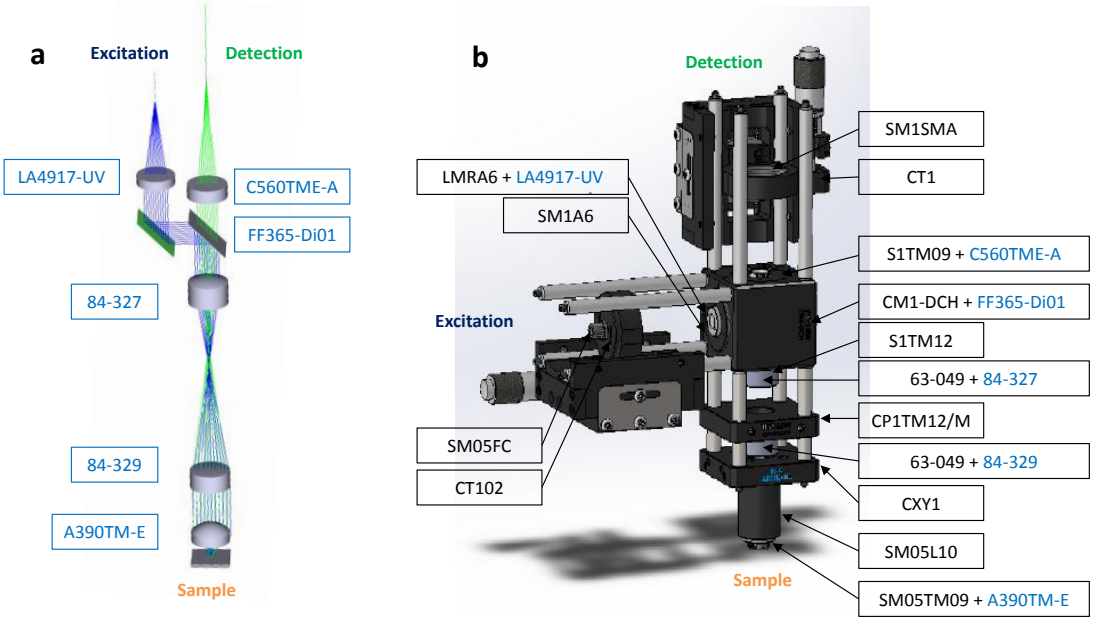

Figure 6.1 (a) Optical ray trace of the preliminary design of the future hand-held probe for non-invasive sensing of implanted tissue-engineered constructs in human. An aspherical lens was employed for an objective lens and two achromatic lenses for higher resolution via further magnification without chromatic aberration. (b) Design of non-miniaturized proof-of-concept system proposed here, based on 30 mm- cage optical mounts. Model names for commercially-available lenses and mounts are labeled

6.2.3 Optoelectronic Microprobe

2nd Prototype Design and Fabrication

The next version of the prototype will have a physical dimension that fits within the inner diameter of a 19G needle (~850 µm). While the current prototype was developed on 500 µm-thick wafer, the bottom side of the next version could be etched to a ~ 100 µm for needle integration. Relative position of two LEDs to PD could be changed to increase an overlapping area of the optical detection path of each source-detection module. In the current version, the blue LED is located on the other side across the PD, which separates optical detection path of two LEDs (Fig 6.2 (a)). The red LED could be located on the other side of Blue LED as shown in Fig. 6.2 (b). The effect of a prolonged optical path for the red LED (> 600 µm) could be simulated by the developed RTMC simulation.

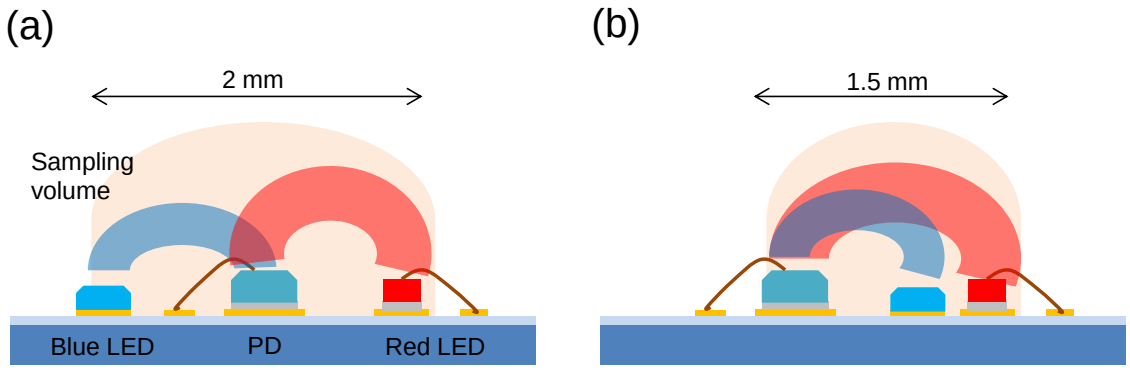

Figure 6.2 (a) Current configuration of the PD and LEDs in the prototype assumes the homogeneity of the sample (~ $1mm^3$) interrogated by optical path (which is shaped like "banana pattern") of detected photons in each Blue LED-PD and Red LED-PD module although each path separates. The optical sampling volume is comparable to a biopsy volume acquired by EUS-FAN procedure. (a) However, if Red LED is moved to the next to Blue LED, the interrogation volume could be reduced and overlapping area of the optical path could increase, thus increasing the overall resolution of optical sensing.

In vivo Validation on Mouse Model

Once the second prototype is developed and fully verified, the prototype could be integrated with the 19G needle (EchoTip ProCore^{TM} 19G, Cook Medical) and tested on *in vivo* mouse model. Since the measured reflectance from human pancreatic xenografts in mice with immunodeficiency showed the similarity of human study [55], the same xenograft model could be employed. Genetically-engineered mouse model [138] mimicking pancreatic tumorigensis developed by Magliano Group in the University of Michigan could help to investigate the potential of microprobe in staging the carcinogenesis, as well as the effect of fibroinflammatory stroma along with changes in cellular structures of pancreatic tissues.

Quantification on Quasi-Spectral Sensing

Besides a simple ratio metric the current prototype can provide as diagnostic parameter, adding more LEDs with different wavelengths could enable a quantitative analysis based on quasi-spectral information. In our preliminary study, mathematical models on human pancreatic reflectance spectra with only four wavelengths could extract almost the same scattering parameters with the ones from full-wavelength spectrum (176 discrete wavelengths). The optimal selection of those wavelength and arrangement of each LED will need to be further investigated.

Realization of fluorescence sensing

To realize fluorescence sensing in the microprobe, a micro-sized long-pass filter must be fabricated. The feasibility of fabrication has been demonstrated by staking layers of TiO_2 and SiO_2 based on Fabri-Perot thin-film optical resonator [139]. The performance (e.g. quantum yield and low dark current) of the current silicon photodiode will need to be

more thoroughly evaluated that it is capable of high-SNR fluorescence measurements. Alternatively, a silicon photo-multiplier [140] could be employed if the dimension is compatible with a needle.

Testing Mechanical Integrity

A mechanical break down of the microprobe during the procedure will cause a serious problem to the patient. Thus, a complete packaging of the device is essential and thorough mechanical tests must be performed prior to being inserted inside the needle for *in vivo* measurements. In particular, the fabricated microprobe must endure the acute curvature that the end of an endoscope and a needle elevation form together to reach the pancreas. To test the mechanical integrity of the fabricated microprobe, the Erlangen Active Simulator for Interventional Endoscopy (EASIE™), a clinical endoscopic training simulator will be employed (Fig. 6.3). The FNA hollow needle, containing the microprobe, will be inserted through the instrument channel of the endoscope, protruded through the swine stomach, and into the pancreas-simulating phantom. The microprobe will be removed from the endoscope and reinserted. Optoelectronic performance will be assessed by acquiring optical data pre- and post-insertion. Mechanical integrity will be verified via microscopic visual examination and electronic testing.

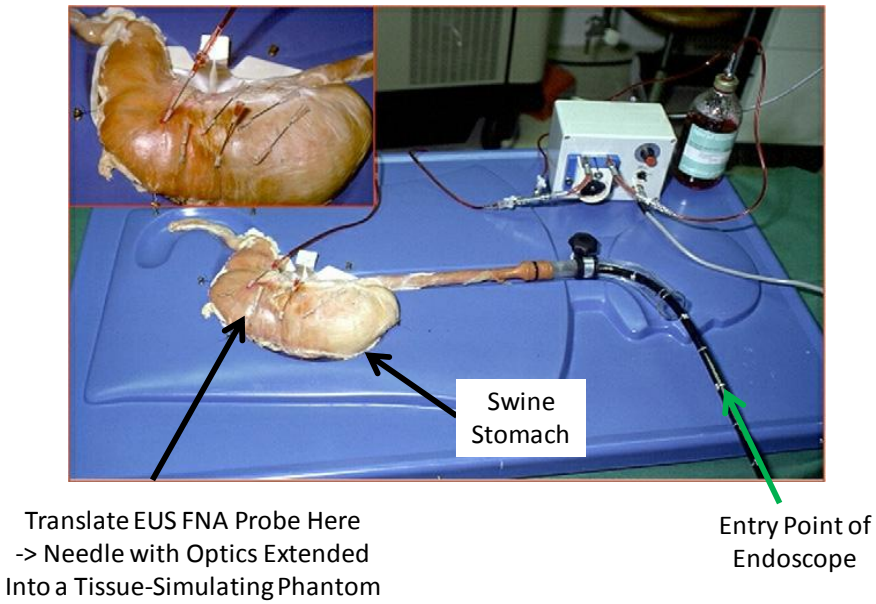

Figure 6.3 Erlanger Active Simulator for Interventional Endoscopy (EASIE™). Mechanical performance of the miniaturized optoelectronic probe will be validated by passing a needle containing the microprobe through the working channel of an EUS scope, placed into the model stomach to simulate the human procedure. Once the EUS scope is within the stomach, a tissue-simulating phantom will be placed in the position of the pancreas outside the stomach to validate the optical performance when the needle is manipulated as in the clinical exam [141] The FNA needle with microprobe will be protruded into the phantom for measurements; baseline measurements will be acquired immediately prior to the procedure. Measurements will occur from both optical modules at 5 locations in the homogeneous phantom, yielding ten optical measurements. Measurements will be compared to each other and baselines.

In case that a continuous or chronic monitoring is necessary, hermetic sealing can be carried out to provide superior integrity and protection against the device degradation. A glass cap would be bonded on the Indium pattern surrounding the optoelectronic components using a proper temperature and pressure [142].

References

1. D. J. Evers, B. H. W. Hendriks, G. W. Lucassen, and T. J. M. Ruers, "Optical spectroscopy: current advances and future applications in cancer diagnostics and therapy," Future Oncol 8, 307-320 (2012).
2. R. L. William, C. Leng-Chun, and M. Mary-Ann, "Fluorescence Spectroscopy," in Optical Techniques in Regenerative Medicine (Taylor & Francis, 2013), pp. 171-204.
3. I. Georgakoudi, E. E. Sheets, M. G. Müller, V. Backman, C. P. Crum, K. Badizadegan, R. R. Dasari, and M. S. Feld, "Trimodal spectroscopy for the detection and characterization of cervical precancers in vivo," American Journal of Obstetrics and Gynecology 186, 374-382 (2002).
4. R. Richards-Kortum and E. Sevick-Muraca, "Quantitative optical spectroscopy for tissue diagnosis," Annual Review of Physical Chemistry 47, 555-606 (1996).
5. V. Backman, M. B. Wallace, L. T. Perelman, J. T. Arendt, R. Gurjar, M. G. Müller, Q. Zhang, G. Zonios, E. Kline, T. McGillican, S. Shapshay, T. Valdez, K. Badizadegan, J. M. Crawford, M. Fitzmaurice, S. Kabani, H. S. Levin, M. Seiler, R. R. R. R. Dasari, I. I. Itzkan, J. J. Van Dam, and M. S. M. S. Feld, "Detection of preinvasive cancer cells," Nature 406, 35-36 (2000).
6. H.-W. Wang, J.-K. Jiang, C.-H. Lin, J.-K. Lin, G.-J. Huang, and J.-S. Yu, "Diffuse reflectance spectroscopy detects increased hemoglobin concentration and decreased oxygenation during colon carcinogenesis from normal to malignant tumors," Opt. Express 17, 2805–2817 (2009).
7. Z. Volynskaya, A. S. Haka, K. L. Bechtel, M. Fitzmaurice, R. Shenk, N. Wang, J. Nazemi, R. R. Dasari, and M. S. Feld, "Diagnosing breast cancer using diffuse reflectance spectroscopy and intrinsic fluorescence spectroscopy," J Biomed Opt 13, 024012 (2008).
8. K. S. Lee and L. M. Gartner, "Spectrophotometric Characteristics of Bilirubin," Pediatr Res 10, 782-788 (1976).
9. G. Zonios, A. Dimou, I. Bassukas, D. Galaris, A. Tsolakidis, and E. Kaxiras, "Melanin absorption spectroscopy: new method for noninvasive skin investigation and melanoma detection," J. Biomed. Opt. 13, 014017 (2008).
10. M. Chandra, K. Vishwanath, G. D. Fichter, E. Liao, S. J. Hollister, and M.-A. Mycek, "Quantitative molecular sensing in biological tissues: an approach to non-invasive optical characterization," Opt Express 14, 6157-6171 (2006).

11. K. Vishwanath, K. Chang, D. Klein, Y. F. Deng, V. Chang, J. E. Phelps, and N. Ramanujam, "Portable, Fiber-Based, Diffuse Reflection Spectroscopy (DRS) Systems for Estimating Tissue Optical Properties," Appl Spectrosc 65, 206-215 (2011).

12. J. Y. Lo, B. Yu, H. L. Fu, J. E. Bender, G. M. Palmer, T. F. Kuech, and N. Ramanujam, "A strategy for quantitative spectral imaging of tissue absorption and scattering using light emitting diodes and photodiodes," Opt Express 17, 1372-1384 (2009).

13. J. R. Lakowicz, Principles of Fluorescence Spectroscopy, 3rd ed. (Springer, New York, 2006), p. 954.

14. G. Zonios, L. T. Perelman, V. Backman, R. Manoharan, M. Fitzmaurice, J. V. Dam, and M. S. Feld, "Diffuse reflectance spectroscopy of human adenomatous colon polyps in vivo," Appl Optics 38, 6628-6637 (1999).

15. R. Reif, O. A'Amar, and I. J. Bigio, "Analytical model of light reflectance for extraction of the optical properties in small volumes of turbid media," Appl Optics 46, 7317-7328 (2007).

16. L. Wang, S. L. Jacques, and L. Zheng, "MCML - Monte Carlo modeling of photon transport in multi-layered tissues," Comput Meth Prog Bio 47, 131-146 (1995).

17. "Optical Thermal Response of Laser-Irradiated Tissue, Second Edition," Optical Thermal Response of Laser-Irradiated Tissue, Second Edition, 1-958 (2011).

18. I. Georgakoudi, B. C. Jacobson, J. Van Dam, V. Backman, M. B. Wallace, M. G. Muller, Q. Zhang, K. Badizadegan, D. Sun, G. A. Thomas, L. T. Perelman, and M. S. Feld, "Fluorescence, reflectance, and light-scattering spectroscopy for evaluating dysplasia in patients with Barrett's esophagus," Gastroenterology 120, 1620-1629 (2001).

19. T. J. Farrell, M. S. Patterson, and B. C. Wilson, "A diffusion theory model of spatially resolved, steady-state diffuse reflectance for the noninvasive determination of tissue optical properties in vivo," Med. Phys. 19, 879-888 (1992).

20. K. M. Yoo, F. Liu, and R. R. Alfano, "When does the diffusion approximation fail to describe photon transport in random media?," Phys. Rev. Lett. 64(1990).

21. C. Zhu, T. M. Breslin, J. Harter, and N. Ramanujam, "Model based and empirical spectral analysis for the diagnosis of breast cancer," Opt. Express 16, 14961-14978 (2008).

22. R. H. Wilson, M. Chandra, J. Scheiman, D. Simeone, B. McKenna, J. Purdy, and M.-A. Mycek, "Optical spectroscopy detects histological hallmarks of pancreatic cancer," Opt Express 17, 17502-17516 (2009).

23. C. G. Zhu and Q. Liu, "Review of Monte Carlo modeling of light transport in tissues," J Biomed Opt 18(2013).

24. I. Pavlova, C. Redden Weber, R. A. Schwarz, M. Williams, A. El-Naggar, A. Gillenwater, and R. Richards-Kortum, "Monte Carlo model to describe depth

selective fluorescence spectra of epithelial tissue: applications for diagnosis of oral precancer " J. Biomed. Opt. 13, 064012 (2008).

25. R. Chen, Z. W. Huang, H. Lui, I. Hamzavi, D. I. McLean, S. S. Xie, and H. S. Zeng, "Monte Carlo simulation of cutaneous reflectance and fluorescence measurements - The effect of melanin contents and localization," J Photoch Photobio B 86, 219-226 (2007).

26. C. Zhu, Q. Liu, and N. Ramanujam, "Effect of fiber optic probe geometry on depth-resolved fluorescence measurements from epithelial tissues: a Monte Carlo simulation," J Biomed Opt 8, 237-247 (2003).

27. F. Jaillon, W. Zheng, and Z. Huang, "Half-ball lens couples a beveled fiber probe for depth-resolved spectroscopy: Monte Carlo simulations," Appl Optics 47, 3152-3157 (2008).

28. I. Fredriksson, M. Larsson, and T. Stromberg, "Inverse Monte Carlo method in a multilayered tissue model for diffuse reflectance spectroscopy," J Biomed Opt 17(2012).

29. G. M. Palmer and N. Ramanujam, "Monte Carlo-based inverse model for calculating tissue optical properties. Part I: Theory and validation on synthetic phantoms," Appl Optics 45, 1062–1071 (2006).

30. N. Y. Boo and S. Ishak, "Prediction of severe hyperbilirubinaemia using the Bilicheck transcutaneous bilirubinometer," J Paediatr Child H 43, 306-311 (2007).

31. G. Monheit, A. B. Cognetta, L. Ferris, H. Rabinovitz, K. Gross, M. Martini, J. M. Grichnik, M. Mihm, V. G. Prieto, P. Googe, R. King, A. Toledano, N. Kabelev, M. Wojton, and D. Gutkowicz-Krusin, "The Performance of MelaFind A Prospective Multicenter Study," Arch Dermatol 147, 188-194 (2011).

32. R. Mehrotra, "A Cross-Sectional Study Evaluating Chemiluminescence and Autofluorescence in the Detection of Clinically Innocuous Precancerous and Cancerous Oral Lesions (vol 141, pg 151, 2010)," J Am Dent Assoc 141, 388-388 (2010).

33. D. G. Ferris, R. A. Lawhead, E. D. Dickman, N. Holtzapple, J. A. Miller, S. Grogan, S. Bambot, A. Agrawal, and M. L. Faupel, "Multimodal Hyperspectral Imaging for the Noninvasive Diagnosis of Cervical Neoplasia," Journal of Lower Genital Tract Disease 5, 65-72 (2001).

34. D. Roblyer, R. Richards-Kortum, K. Sokolov, A. K. El-Naggar, M. D. Williams, C. Kurachi, and A. M. Gillenwater, "Multispectral optical imaging device for in vivo detection of oral neoplasia," J Biomed Opt 13, 024019 (2008).

35. R. A. Zangaro, L. Silveira, Jr., R. Manoharan, G. Zonios, I. Itzkan, R. R. Dasari, J. Van-Dam, and M. S. Feld, "Rapid multiexcitation fluorescence spectroscopy system for in vivo tissue diagnosis," Appl Optics 35, 5211- 5219 (1996).

36. S. C. Kanick, C. van der Leest, R. S. Djamin, A. M. Janssens, H. C. Hoogsteden, H. J. C. M. Sterenborg, A. Amelink, and J. G. J. V. Aerts, "Characterization of Mediastinal Lymph Node Physiology In Vivo by Optical Spectroscopy during

Endoscopic Ultrasound-Guided Fine Needle Aspiration," Journal of Thoracic Oncology 5, 981-987 910.1097/JTO.1090b1013e3181ddbc1090e (2010).

37. L. Rahib, B. D. Smith, R. Aizenberg, A. B. Rosenzweig, J. M. Fleshman, and L. M. Matrisian, "Projecting Cancer Incidence and Deaths to 2030: The Unexpected Burden of Thyroid, Liver, and Pancreas Cancers in the United States," Cancer Research 74, 2913-2921 (2014).

38. B. D. Smith, G. L. Smith, A. Hurria, G. N. Hortobagyi, and T. A. Buchholz, "Future of Cancer Incidence in the United States: Burdens Upon an Aging, Changing Nation," J Clin Oncol 27, 2758-2765 (2009).

39. "Cancer Facts & Figures 2015" (American Cancer Society), retrieved www.cancer.org.

40. M. Callery, K. Chang, E. Fishman, M. Talamonti, L. William Traverso, and D. Linehan, "Pretreatment Assessment of Resectable and Borderline Resectable Pancreatic Cancer: Expert Consensus Statement," Ann Surg Oncol 16, 1727-1733 (2009).

41. M. Eloubeidi, S. Varadarajulu, S. Desai, R. Shirley, M. Heslin, M. Mehra, J. Arnoletti, I. Eltoum, C. Wilcox, and S. Vickers, "A Prospective Evaluation of an Algorithm Incorporating Routine Preoperative Endoscopic Ultrasound-Guided Fine Needle Aspiration in Suspected Pancreatic Cancer," J Gastrointest Surg 11, 813-819 (2007).

42. W. Hartwig, L. Schneider, M. K. Diener, F. Bergmann, M. W. Büchler, and J. Werner, "Preoperative tissue diagnosis for tumours of the pancreas," Br. J. Surg. 96, 5-20 (2009).

43. C.-K. Ho, J. Kleeff, H. Friess, and M. W. Büchler, "Complications of pancreatic surgery," Hpb 7, 99-108 (2005).

44. S. C. Abraham, R. E. Wilentz, C. J. Yeo, T. A. Sohn, J. L. Cameron, J. K. Boitnott, and R. H. Hruban, "Pancreaticoduodenectomy (Whipple Resections) in Patients Without Malignancy: Are They All `Chronic Pancreatitis'?," The American Journal of Surgical Pathology 27, 110-120 (2003).

45. A. Fritscher-Ravens, L. Brand, W. T. Knöfel, C. Bobrowski, T. Topalidis, F. Thonke, A. de Werth, and N. Soehendra, "Comparison of endoscopic ultrasound-guided fine needle aspiration for focal pancreatic lesions in patients with normal parenchyma and chronic pancreatitis," Am J Gastroenterol 97, 2768-2775 (2002).

46. P. Singh, A. Chak, J. E. Willis, A. Rollins, and M. V. Sivak Jr, "In vivo optical coherence tomography imaging of the pancreatic and biliary ductal system," Gastrointest Endosc 62, 970-974 (2005).

47. P. A. Testoni, B. Mangiavillano, L. Albarello, P. G. Arcidiacono, A. Mariani, E. Masci, and C. Doglioni, "Optical coherence tomography to detect epithelial lesions of the main pancreatic duct: an ex vivo study," Am J Gastroenterol 100, 2777-2783 (2005).

48. P. A. Testoni, A. Mariani, B. Mangiavillano, P. G. Arcidiacono, S. Di Pietro, and E. Masci, "Intraductal optical coherence tomography for investigating main pancreatic duct strictures," Am J Gastroenterol 102, 269-274 (2007).

49. S. Eser, M. Messer, P. Eser, A. von Werder, B. Seidler, M. Bajbouj, R. Vogelmann, A. Meining, J. von Burstin, H. Algül, P. Pagel, A. E. Schnieke, I. Esposito, R. M. Schmid, G. Schneider, and D. Saur, "In vivo diagnosis of murine pancreatic intraepithelial neoplasia and early-stage pancreatic cancer by molecular imaging," Proceedings of the National Academy of Sciences 108, 9945-9950 (2011).

50. V. J. Konda, A. Meining, L. H. Jamil, M. Giovannini, K. J. Chang, J. H. Hwang, M. B. Wallace, U. D. Siddiqui, H. R. Aslanian, and S. K. Lo, "An International, Multi-Center Trial on Needle-Based Confocal Laser Endomicroscopy (nCLE): Results From the In Vivo CLE Study in the Pancreas With Endosonography of Cystic Tumors (INSPECT)," Gastroenterology 142, S-620-S-621 (2012).

51. W. Hu, G. Zhao, C. Wang, J. Zhang, and L. Fu, "Nonlinear Optical Microscopy for Histology of Fresh Normal and Cancerous Pancreatic Tissues," PLoS ONE 7, e37962 (2012).

52. D. Piao, K. E. Bartels, R. G. Postier, G. Reed Holyoak, and J. W. Ritchey, "Toward transduodenal diffuse optical tomography of proximal pancreas," Opt Lett 38, 4142-4145 (2013).

53. Y. Liu, R. E. Brand, V. Turzhitsky, Y. L. Kim, H. K. Roy, N. Hasabou, C. Sturgis, D. Shah, C. Hall, and V. Backman, "Optical markers in duodenal mucosa predict the presence of pancreatic cancer," Clin Cancer Res 13, 4392-4399 (2007).

54. M. Patel, A. Gomes, S. Ruderman, D. Hardee, S. Crespo, M. Raimondo, T. Woodward, V. Backman, H. Roy, and M. Wallace, "Polarization gating spectroscopy of normal-appearing duodenal mucosa to detect pancreatic cancer," Gastrointest Endosc 80, 786-+ (2014).

55. M. Chandra, J. Scheiman, D. Heidt, D. Simeone, B. McKenna, and M.-A. Mycek, "Probing pancreatic disease using tissue optical spectroscopy," J Biomed Opt 12, 060501 (2007).

56. M. Chandra, J. Scheiman, D. Simeone, B. McKenna, J. Purdy, and M.-A. Mycek, "Spectral areas and ratios classifier algorithm for pancreatic tissue classification using optical spectroscopy," J Biomed Opt 15, 010514 (2010).

57. R. H. Wilson, M. Chandra, L.-C. Chen, W. Lloyd, J. Scheiman, D. Simeone, J. Purdy, B. McKenna, and M.-A. Mycek, "Photon-tissue interaction model enables quantitative optical analysis of human pancreatic tissues," Opt Express 18, 21612-21621 (2010).

58. "Cancer Facts & Figures 2013" (American Cancer Society, 2013), retrieved www.cancer.org.

59. R. H. Hruban and e. al., "An illustrated consensus on the classification of pancreatic intraepithelial neoplasia and intraductal papillary mucinous neoplasms," Am J Surg Pathol 28, 977-987 (2004).

60. T. Baba, T. Yamaguchi, T. Ishihara, A. Kobayashi, T. Oshima, N. Sakaue, K. Kato, M. Ebara, and H. Saisho, "Distinguishing benign from malignant intraductal papillary mucinous tumors of the pancreas by imaging techniques," Pancreas 29, 212-217 (2004).

61. C. R. Ferrone, C. Correa-Gallego, A. L. Warshaw, W. R. Brugge, D. G. Forcione, S. P. Thayer, and C. Fernandez-del Castillo, "Current Trends in Pancreatic Cystic Neoplasms," Arch Surg-Chicago 144, 448-454 (2009).

62. F. Maire, A. Couvelard, P. Hammel, P. Ponsot, L. Palazzo, A. Aubert, C. Degott, A. Dancour, M. Felce-Dachez, D. O'Toole, P. Levy, and P. Ruszniewski, "Intraductal papillary mucinous tumors of the pancreas: the preoperative value of cytologic and histopathologic diagnosis," Gastrointest Endosc 58, 701-706 (2003).

63. M. A. Eloubeidi and A. Tamhane, "EUS-guided FNA of solid pancreatic masses: a learning curve with 300 consecutive procedures," Gastrointest Endosc 61, 700-708 (2005).

64. V. T.-C. Chang, P. S. Cartwright, S. M. Bean, G. M. Palmer, R. C. Bentley, and N. Ramanujam, "Quantitative physiology of the precancerous cervix in vivo through optical spectroscopy," Neoplasia 11, 325-332 (2009).

65. M.-A. Mycek, K. Schomacker, and N. Nishioka, "Colonic polyp differentiation using time resolved autofluorescence spectroscopy," Gastrointest Endosc 48, 390-394 (1998).

66. R. H. Wilson and M.-A. Mycek, "Models of light propagation in human tissue applied to cancer diagnostics," Technology in Cancer Research and Treatment 10, 121-134 (2011).

67. S. C. Kanick, C. van der Leest, J. G. J. V. Aerts, H. C. Hoogsteden, S. Kascakova, H. J. C. M. Sterenborg, and A. Amelink, "Integration of single-fiber reflectance spectroscopy into ultrasound-guided endoscopic lung cancer staging of mediastinal lymph nodes," J Biomed Opt 15, 017004 (2010).

68. R. H. Wilson, M. Chandra, L. C. Chen, W. R. Lloyd, J. Scheiman, D. Simeone, J. Purdy, B. McKenna, and M.-A. Mycek, "Photon-tissue interaction model enables quantitative optical analysis of human pancreatic tissues," Opt Express 18, 21612-21621 (2010).

69. L. T. Perelman, V. Backman, M. Wallace, G. Zonios, R. Manoharan, A. Nusrat, S. Shields, M. Seiler, C. Lima, T. Hamano, I. Itzkan, J. Van Dam, J. M. Crawford, and M. S. Feld, "Observation of periodic fine structure in reflectance from biological tissue: a new technique for measuring nuclear size distribution," Phys Rev Lett 80, 627-630 (1998).

70. R. K. Bista, S. Uttam, P. Wang, K. Staton, S. Choi, C. J. Bakkenist, D. J. Hartman, R. E. Brand, and Y. Liu, "Quantification of nanoscale nuclear refractive index changes during the cell cycle," J Biomed Opt 16, 070503 (2011).

71. C. Lau, O. Scepanovic, J. Mirkovic, S. Mcgee, C. C. Yu, S. Fulghum, M. Wallace, J. Tunnell, K. Bechtel, and M. Feld, "Re-evaluation of model-based light-scattering spectroscopy for tissue spectroscopy," J Biomed Opt 14, 024031 (2009).

72. A. Amelink, H. J. C. M. Sterenborg, M. P. L. Bard, and S. A. Burgers, "In vivo measurement of the local optical properties of tissue by use of differential path-length spectroscopy," Opt Lett 29, 1087-1089 (2004).

73. R. Drezek, M. Guillaud, T. Collier, I. Boiko, A. Malpica, C. Macaulay, M. Follen, and R. Richards-Kortum, "Light scattering from cervical cells throughout neoplastic progression: influence of nuclear morphology, DNA content, and chromatin texture," J Biomed Opt 8, 7-16 (2003).

74. M. Erkan, S. Hausmann, C. W. Michalski, A. A. Fingerle, M. Dobritz, J. Kleeff, and H. Friess, "The role of stroma in pancreatic cancer: diagnostic and therapeutic implications," Nat Rev Gastro Hepat 9, 454-467 (2012).

75. J. D. Pitts and M.-A. Mycek, "Design and development of a rapid acquisition laser-based fluorometer with simultaneous spectral and temporal resolution," Rev Sci Instrum 72, 3061-3072 (2001).

76. S. L. Jacques, "Optical properties of biological tissues: a review," Phys Med Biol 58, R37-R61 (2013).

77. I. S. Saidi, S. L. Jacques, and F. K. Tittel, "Mie and Rayleigh Modeling of Visible-Light Scattering in Neonatal Skin," Appl Optics 34, 7410-7418 (1995).

78. J. R. Mourant, T. Fuselier, J. Boyer, T. Johnson, and I. Bigio, "Predictions and measurements of scattering and absorption over broad wavelength ranges in tissue phantoms," Appl Optics 36, 949-957 (1997).

79. J. R. Mourant, J. P. Freyer, A. H. Hielscher, A. A. Eick, D. Shen, and T. M. Johnson, "Mechanisms of light scattering from biological cells relevant to noninvasive optical-tissue diagnostics," Appl Optics 37, 3586-3593 (1998).

80. R. Graaff, J. G. Aarnoudse, J. R. Zjip, P. M. A. Sloot, F. F. M. de-Mul, J. Greve, and M. H. Koelink, "Reduced light-scattering properties for mixtures of spherical particles: a simple approximation derived from Mie calculations," Appl Optics 31, 1370-1376 (1992).

81. S. Srinivasan, B. W. Pogue, S. D. Jiang, H. Dehghani, C. Kogel, S. Soho, J. J. Gibson, T. D. Tosteson, S. P. Poplack, and K. D. Paulsen, "Interpreting hemoglobin and water concentration, oxygen saturation, and scattering measured in vivo by near-infrared breast tomography," P Natl Acad Sci USA 100, 12349-12354 (2003).

82. W. Lloyd, R. H. Wilson, C.-W. Chang, G. D. Gillispie, and M.-A. Mycek, "Instrumentation to rapidly acquire fluorescence wavelength-time matrices of biological tissues," Biomedical Optics Express 1, 574-586 (2010).

83. J. A. Hanley, A. Negassa, M. D. deB. Eduardes, and J. E. Forrester, "Statistical Analysis of Correlated Data Using Generalized Estimating Equations: An Orientation " Am J Epidemiol 157, 364-375 (2003).

84. P. Burton, L. Gurrin, and P. Sly, "Extending the simple linear regression model to account for correlated responses: An introduction to generalized estimating equations and multi-level mixed modelling," Stat Med 17, 1261-1291 (1998).

85. D. L. Fortes, M. S. Allen, V. J. Lowe, K.-H. R. Shen, D. A. Wigle, S. D. Cassivi, F. C. Nichols, and C. Deschamps, "The sensitivity of 18F-fluorodeoxyglucose positron emission tomography in the evaluation of metastatic pulmonary nodules," European Journal of Cardio-Thoracic Surgery 34, 1223-1227 (2008).

86. R. F. Brem, A. C. Floerke, J. A. Rapelyea, C. Teal, T. Kelly, and V. Mathur, "Breast-specific Gamma imaging as an adjunct imaging modality for the diagnosis of breast cancer," Radiology 247, 651-657 (2008).

87. R. G. Newcombe, "Two-sided confidence intervals for the single proportion: Comparison of seven methods," Stat Med 17, 857-872 (1998).

88. G. Zonios and A. Dimou, "Light scattering spectroscopy of human skin in vivo," Opt Express 17, 1256-1267 (2009).

89. G. Vizzeri, R. N. Weinreb, A. O. Gonzalez-Garcia, C. Bowd, F. A. Medeiros, P. A. Sample, and L. M. Zangwill, "Agreement between spectral-domain and time-domain OCT for measuring RNFL thickness," Br. J. Ophthalmol. 93, 775-781 (2009).

90. M.-A. Mycek and B. W. Pogue, eds., Handbook of Biomedical Fluorescence (Marcel Dekker, Inc., New York, 2003).

91. J. T. C. Liu, M. J. Mandella, J. M. Crawford, C. H. Contag, T. D. Wang, and G. S. Kino, "Efficient rejection of scattered light enables deep optical sectioning in turbid media with low-numerical-aperture optics in a dual-axis confocal architecture," J Biomed Opt 13(2008).

92. Y. Chen, D. N. Wang, and J. T. C. Liu, "Assessing the tissue-imaging performance of confocal microscope architectures via Monte Carlo simulations," Opt Lett 37, 4495-4497 (2012).

93. J. P. Zinter and M. J. Levene, "Maximizing fluorescence collection efficiency in multiphoton microscopy," Opt. Express 19, 15348-15362 (2011).

94. K. Vishwanath, B. W. Pogue, and M.-A. Mycek, "Quantitative fluorescence lifetime spectroscopy in turbid media: comparison of theoretical, experimental and computational methods," Phys Med Biol 47, 3387-3405 (2002).

95. T. J. Pfefer, K. T. Schomacker, M. N. Ediger, and N. S. Nishioka, "Multiple-fiber probe design for fluorescence spectroscopy in tissue," Appl Optics 41, 4712-4721 (2002).

96. L. Nieman, A. Myakov, J. Aaron, and K. Sokolov, "Optical sectioning using a fiber probe with an angled illumination-collection geometry: evaluation in engineered tissue phantoms," Appl Optics 43, 1308-1319 (2004).

97. R. A. Schwarz, D. Arifler, S. K. Chang, I. Pavlova, I. A. Hussain, V. Mack, B. Knight, R. Richards-Kortum, and A. M. Gillenwater, "Ball lens coupled fiber-optic probe for depth-resolved spectroscopy of epithelial tissue," Opt Lett 30, 1159-1161 (2005).

98. F. Jaillon, W. Zheng, and Z. Huang, "Beveled fiber-optic probe couples a ball lens for improving depth-resolved fluorescence measurements of layered tissue: Monte Carlo simulations," Phys Med Biol 53, 937 (2008).

99. K. Vishwanath and M.-A. Mycek, "Time-resolved photon migration in bi-layered tissue models," Opt Express 13, 7466-7482 (2005).

100. V. Schweller, R. H. Wilson, and M.-A. Mycek, "User-friendly Monte Carlo code for time-resolved fluorescence models of tissues with irregular interfaces," in Biomedical Optics 2010 Technical Digest (Optical Society of America), 3 pages (2010).

101. K. Vishwanath and M.-A. Mycek, "Do fluorescence decays remitted from tissues accurately reflect intrinsic fluorophore lifetimes?," Opt Lett 29, 1512-1514 (2004).

102. F. Ayers, A. Grant, D. Kuo, D. J. Cuccia, and A. J. Durkin, "Fabrication and characterization of silicone-based tissue phantoms with tunable optical properties in the visible and near infrared domain - art. no. 687007," Design and Performance Validation of Phantoms Used in Conjunction with Optical Measurements of Tissue 6870, 87007-87007 (2008).

103. A. Amelink, O. P. Kaspers, H. J. Sterenborg, J. E. van der Wal, J. L. Roodenburg, and M. J. Witjes, "Non-invasive measurement of the morphology and physiology of oral mucosa by use of optical spectroscopy," Oral Oncol 44, 65-71 (2008).

104. J. Q. Brown, L. G. Wilke, J. Geradts, S. A. Kennedy, G. M. Palmer, and N. Ramanujam, "Quantitative Optical Spectroscopy: A Robust Tool for Direct Measurement of Breast Cancer Vascular Oxygenation and Total Hemoglobin Content In vivo," Cancer Research 69, 2919-2926 (2009).

105. C. Fang, D. Brokl, R. E. Brand, and Y. Liu, "Depth-selective fiber-optic probe for characterization of superficial tissue at a constant physical depth," Biomedical Optics Express 2, 838-849 (2011).

106. H. L. Fu, B. Yu, J. Y. Lo, G. M. Palmer, T. F. Kuech, and N. Ramanujam, "A low-cost, portable, and quantitative spectral imaging system for application to biological tissues," Optics Express 18, 12630-12645 (2010).

107. C. F. Zhu, E. S. Burnside, G. A. Sisney, L. R. Salkowski, J. M. Harter, B. Yu, and N. Ramanujam, "Fluorescence Spectroscopy: An Adjunct Diagnostic Tool to Image-Guided Core Needle Biopsy of the Breast," Ieee T Bio-Med Eng 56, 2518-2528 (2009).

108. J. S. Soares, I. Barman, N. C. Dingari, Z. Volynskaya, W. Liu, N. Klein, D. Plecha, R. R. Dasari, and M. Fitzmaurice, "Diagnostic power of diffuse reflectance spectroscopy for targeted detection of breast lesions with microcalcifications," Proceedings of the National Academy of Sciences 110, 471-476 (2013).

109. S. C. Kanick, C. van der Leest, J. G. J. V. Aerts, H. C. Hoogsteden, S. Kaščáková, H. J. C. M. Sterenborg, and A. Amelink, "Integration of single-fiber reflectance spectroscopy into ultrasound-guided endoscopic lung cancer staging of mediastinal lymph nodes " J. Biomed. Opt. 15, 017004 (2010).

110. S. C. Kanick, C. van der Leest, J. Aerts, H. J. C. M. Sterenborg, and A. Amelink, "Incorporation of Single Fiber Reflectance Spectroscopy into Ultrasound-Guided Endoscopy (EUS-FNA) of Mediastinal Lymph Nodes," in OSA Technical Digest (CD) (Optical Society of America, 2010), BTuD89.

111. V. Sharma, P. Kapur, E. Olweny, J. Cadeddu, C. G. Roehrborn, and H. Liu, "Auto-fluorescence lifetime spectroscopy for prostate cancer detection: an optical biopsy approach," in OSA Technical Digest (Optical Society of America, 2012), JM3A.19.

112. Y. Pu, W. Wang, G. Tang, Y. Budansky, M. Sharonov, M. Xu, S. Achilefu, J. A. Eastham, and R. R. Alfano, "Screening prostate cancer using a portable near infrared scanning imaging unit with an optical fiber-based rectal probe," 822002-822002 (2012).

113. A. Desjardins, M. van der Voort, S. Roggeveen, G. Lucassen, W. Bierhoff, B. Hendriks, M. Brynolf, and B. Holmström, "Needle stylet with integrated optical fibers for spectroscopic contrast during peripheral nerve blocks," J Biomed Opt 16, 077004 (2011).

114. A. Balthasar, A. E. Desjardins, M. van der Voort, G. W. Lucassen, S. Roggeveen, K. Wang, W. Bierhoff, A. G. H. Kessels, M. Sommer, and M. van Kleef, "Optical Detection of Vascular Penetration During Nerve Blocks: An In Vivo Human Study," Regional Anesthesia and Pain Medicine 37, 3-7 (2012).

115. A. Balthasar, A. E. Desjardins, M. van der Voort, G. W. Lucassen, S. Roggeveen, K. Wang, W. Bierhoff, A. G. H. Kessels, M. van Kleef, and M. Sommer, "Optical Detection of Peripheral Nerves: An In Vivo Human Study," Regional Anesthesia and Pain Medicine 37, 277-282 (2012).

116. V. Becker, M. B. Wallace, P. Fockens, S. von Delius, T. A. Woodward, M. Raimondo, R. P. Voermans, and A. Meining, "Needle-based confocal endomicroscopy for in vivo histology of intra-abdominal organs: first results in a porcine model (with videos)," Gastrointest Endosc 71, 1260-1266 (2010).

117. H. Pohl, T. Rösch, M. Vieth, M. Koch, V. Becker, M. Anders, A. C. Khalifa, and A. Meining, "Miniprobe confocal laser microscopy for the detection of invisible neoplasia in patients with Barrett's oesophagus," Gut 57, 1648-1653 (2008).

118. V. Turzhitsky, Y. Liu, N. Hasabou, M. Goldberg, H. K. Roy, V. Backman, and R. Brand, "Investigating population risk factors of pancreatic cancer by evaluation of optical markers in the duodenal mucosa," Dis Markers 25, 313-321 (2008).

119. N. Iftimia, S. Cizginer, V. Deshpande, M. Pitman, S. Tatli, N.-A. Iftimia, D. X. Hammer, M. Mujat, T. Ustun, and R. D. Ferguson, "Differentiation of pancreatic cysts with optical coherence tomography (OCT) imaging: an ex vivo pilot study," Biomedical Optics Express 2, 2372-2382 (2011).

120. P. A. Testoni, A. Mariani, B. Mangiavillano, P. G. Arcidiacono, S. Di Pietro, and E. Masci, "Intraductal optical coherence tomography for investigating main pancreatic duct strictures," The American journal of gastroenterology 102, 269-274 (2007).

121. M. Giovannini, F. Caillol, F. Poizat, E. Bories, C. Pesenti, G. Monges, and J. L. Raoul, "Feasibility of Intratumoral Confocal Microscopy under Endoscopic Ultrasound Guidance," Endoscopic Ultrasound 1, 80-83 (2012).

122. V. J. A. Konda, H. R. Aslanian, M. B. Wallace, U. D. Siddiqui, J. Hart, and I. Waxman, "First assessment of needle-based confocal laser endomicroscopy during EUS-FNA procedures of the pancreas (with videos)," Gastrointest Endosc 74, 1049-1060 (2011).

123. H. Isayama, Y. Nakai, and P. V. Draganov, "The role of Endoscopic Ultrasound (EUS) in the management of patients with pancreatic cancer: now bigger than ever," Journal of gastrointestinal oncology 4, 121 (2013).

124. T. J. Song, J. H. Kim, S. S. Lee, J. B. Eum, S. H. Moon, D. H. Park, D. W. Seo, S. K. Lee, S. J. Jang, S. C. Yun, and M.-H. Kim, "The prospective randomized, controlled trial of endoscopic ultrasound-guided fine-needle aspiration using 22G and 19G aspiration needles for solid pancreatic or peripancreatic masses," The American journal of gastroenterology 105, 1739-1745 (2010).

125. W. R. Lloyd, R. H. Wilson, S. Y. Lee, M. Chandra, B. McKenna, D. Simeone, J. Scheiman, and M.-A. Mycek, "In vivo optical spectroscopy for improved detection of pancreatic adenocarcinoma: a feasibility study," Biomedical Optics Express 5, 9-15 (2014).

126. R. H. Wilson, M. Chandra, J. Scheiman, D. Simeone, B. McKenna, J. Purdy, and M. A. Mycek, "Optical spectroscopy detects histological hallmarks of pancreatic cancer," Optics Express 17, 17502-17516 (2009).

127. J. P. Zinter and M. J. Levene, "Maximizing fluorescence collection efficiency in multiphoton microscopy," Optics Express 19, 15348-15362 (2011).

128. L. Van Hoe and B. Claikens, "The Pancreas: Normal Radiological Anatomy and Variants," in Radiology of the Pancreas, A. Baert, G. Delorme, and L. Van Hoe, eds. (Springer Berlin Heidelberg, 1999), pp. 19-68.

129. J. Valvano, "Tissue Thermal Properties and Perfusion," in Optical-Thermal Response of Laser-Irradiated Tissue, A. J. Welch and M. J. C. van Gemert, eds. (Springer Netherlands, 2011), pp. 455-485.

130. "Database of Tissue Properties" (The Foundation for Research on Informing Technologies in Society),retrieved http://www.itis.ethz.ch/virtual-population/tissue-properties/database/.

131. "New Semiconductor Materials : Characteristics and Properties" (Ioffer Physico-Technical Institute), retrieved http://www.ioffe.ru/SVA/NSM/Semicond/Si/thermal.html.

132. C. C. Lee, C. Y. Wang, G. Matijasevic, and S. S. Chan, "A New Gold-Indium Eutectic Bonding Method," Mater Res Soc Symp P 264, 305-310 (1992).

133. C. C. Lee, C. Y. Wang, and G. Matijasevic, "Au-in Bonding Below the Eutectic Temperature," Ieee T Compon Hybr 16, 311-316 (1993).

134. "EZBright LED Handling and Packaging Recommendations" (Cree Inc.), retrieved http://www.cree.com/LED-Chips-and-Materials/Document-Library.

135. C. N. CN-0139, "Single Supply Low Noise LED Current Source Driver Using a Current Output DAC in the Reverse Mode," (2009).

136. L. Orozco, "Programmable-Gain Transimpedance Amplifiers Maximize Dynamic Range in Spectroscopy Systems" (Analog Dialogue, 2013), retrieved http://www.analog.com/library/analogdialogue/archives/47-05/pgtia.html.

137. A. M. Laughney, V. Krishnaswamy, E. J. Rizzo, M. C. Schwab, R. J. Barth, B. W. Pogue, K. D. Paulsen, and W. A. Wells, "Scatter Spectroscopic Imaging Distinguishes between Breast Pathologies in Tissues Relevant to Surgical Margin Assessment," Clin Cancer Res 18, 6315-6325 (2012).

138. M. A. Collins, F. Bednar, Y. Q. Zhang, J. C. Brisset, S. Galban, C. J. Galban, S. Rakshit, K. S. Flannagan, N. V. Adsay, and M. P. di Magliano, "Oncogenic Kras is required for both the initiation and maintenance of pancreatic cancer in mice," J Clin Invest 122, 639-653 (2012).

139. D. S. Ferreira, J. Mirkovic, R. F. Wolffenbuttel, J. H. Correia, M. S. Feld, and G. Minas, "Narrow-band pass filter array for integrated opto-electronic spectroscopy detectors to assess esophageal tissue," Biomedical Optics Express 2, 1703-1716 (2011).

140. R. Zimmermann, F. Braun, T. Achtnich, O. Lambercy, R. Gassert, and M. Wolf, "Silicon photomultipliers for improved detection of low light levels in miniature near-infrared spectroscopy instruments," Biomedical Optics Express 4, 659-666 (2013).

141. J. Maiss, L. Millermann, K. Heinemann, A. Naegel, A. Peters, K. Matthes, E. G. Hahn, and J. Hochberger, "The compactEASIE® is a feasible training model for endoscopic novices: A prospective randomised trial," Digest Liver Dis 39, 70-78 (2007).

142. R. Straessle, M. Pellaton, Y. Petremand, D. Briand, C. Affolderbach, G. Mileti, and N. F. de Rooij, "Low-temperature indium hermetic sealing of alkali vapor-cells for chip-scale atomic clocks," in Micro Electro Mechanical Systems (MEMS), 2012 IEEE 25th International Conference on, 2012), 361-364.